Summer 2016

Multi-scale modeling and simulation of rolling contact fatigue

Mir Ali Ghaffari Gharehbagh
University of Iowa

MULTI-SCALE MODELING AND SIMULATION OF ROLLING CONTACT FATIGUE

by

Mir Ali Ghaffari Gharehbagh

A thesis submitted in partial fulfillment of the
requirements for the Doctor of Philosophy
degree in Mechanical Engineering
in the Graduate College of
The University of Iowa

August 2016

Thesis Supervisor: Professor Shaoping Xiao

Graduate College
The University of Iowa
Iowa City, Iowa

CERTIFICATE OF APPROVAL

PH.D. THESIS

This is to certify that the Ph.D. thesis of

Mir Ali Ghaffari Gharehbagh

has been approved by the Examining Committee for the thesis requirement for the Doctor of Philosophy degree in Mechanical Engineering at the August 2016 graduation.

Thesis committee: _____
Shaoping Xiao, Thesis Supervisor

_____
Asghar Bhatti

_____
Hongtao Ding

_____
Jia Lu

_____
Hiroyuki Sugiyama

ACKNOWLEDGEMENTS

I would like to express my sincere appreciation to Professor Shaoping Xiao for his support and guidance throughout this research process and throughout my education in the Ph.D. program.

I also thank Professors Jia Lu, Hongtao Ding, Hiroyuki Sugiyama and Asghar Bhatti for serving on my thesis committee.

I would like to express gratitude to my beloved wife, Niloofar, for her kind support during my education at The University of Iowa.

I am very thankful of my parents, Yahya and Roghayyeh whose love and devotion taught me how to be a better person.

To my son, Milan.

ABSTRACT

In this thesis, a hierarchical multiscale method was developed to predict rolling contact fatigue lives of mechanical systems. In the proposed multiscale method, the molecular modeling and simulation of lubricant was conducted to investigate the friction between rolling contact surfaces. The calculated friction coefficient was passed to the continuum model of rolling contact components to predict fatigue lives.

Molecular dynamics modeling and simulation of thin film lubrication and lubricated contact surfaces were carried out to investigate mechanisms of hydrodynamic lubrication at nano-scale first. Although various lubricant alkane chains were considered in the molecular model, the chain length of eight united molecules were mainly employed in this thesis. In addition, the effects of temperature and nano-particles (debris) on the friction forces were discussed. It was found that the existing of nano-particles (debris) could increase the friction force between contact surfaces with hydrodynamic lubrication.

In the continuum model of the developed multiscale method, finite element analysis was employed to predict rolling contact fatigue life of rolling contact components, including bearing and gear-tooth. Specifically, the fatigue crack initiation of bearing was studied, and then the fatigue crack initiation and propagation in gear-tooth. In addition, the enhancement of gear-tooth fatigue life by using composite patches was discussed as well. It should be noted that the friction coefficient used in the continuum model was calculated in the molecular model. It is one-way message passing in

the developed multiscale method.

Another continuum method was studied and developed in this thesis to provide alternate methods for the continuum model in the proposed multiscale framework. Peridynamics method has advantages in modeling and simulation of discontinuities, including cracks, over the conventional finite element methods. The applications of Peridynamics in predicting fatigue crack initiation and propagation lives were discussed in this thesis.

PUBLIC ABSTRACT

This research aims to develop a hierarchical multiscale method to predict rolling contact fatigue lives of mechanical systems. In the proposed multiscale method, the molecular modeling and simulation of lubricant was conducted to investigate the friction between rolling contact surfaces. The calculated friction coefficient was passed to the continuum model of rolling contact components to predict fatigue lives.

Molecular dynamics modeling and simulation of thin film lubrication and lubricated contact surfaces were carried out to investigate mechanisms of hydrodynamic lubrication at nano-scale first. In addition, the effects of temperature and nano-particles (debris) on the friction forces were discussed. It was found that the existing of nano-particles (debris) could increase the friction force between contact surfaces with hydrodynamic lubrication.

In the continuum model of the developed multiscale method, finite element analysis was employed to predict fatigue life of rolling contact components, including bearing and gear-tooth. In addition, the enhancement of gear-tooth fatigue life by using composite patches was discussed as well. It should be noted that the friction coefficient used in the continuum model was calculated in the molecular model. It is one-way message passing in the developed multiscale method.

In addition, Peridynamics approach was studied and developed in this thesis to provide alternate methods for the continuum model in the proposed multiscale framework.

TABLE OF CONTENTS

LIST OF TABLES

Table

LIST OF FIGURES

Figure

CHAPTER 1
INTRODUCTION

1.1 Background information

Gearbox failure is one of the largest sources of unplanned maintenance costs in wind industries because repairing or replacing a failed gearbox in wind turbine in particular is an extremely expensive undertaking. Therefore, when a failure occurs, it is important to correctly identify the failure mode so that the appropriate actions can be taken to reduce the likelihood of a re-occurrence of the same type of failure.

Gearbox failures can be caused by fundamental design issues, manufacturing defects, deficiencies in the lubricant or lubrication system, excessive time at standstill, large loading, and many other reasons. A correct failure mode diagnosis is the first step in identifying the actions that can be taken to prevent additional failures. In gearboxes, some of the most common gear and bearing failure modes are listed as:

- Micropitting can affect both gears and bearings, and failures due to micropitting are very common in wind turbine gearboxes. Micropitting occurs when the lubricant film between contacting surfaces is not thick enough and the surfaces have high amounts of sliding action. Micropitting results in a frosted or matte finish surface in affected areas, as seen in the figure below. Micropitting-related failures can be prevented by changing lubricant type or by reducing contact surface roughness (Fig. 1.1).

Fig. 1.1: Fatigue occurrence on a Roller bearing.

- Macropitting can also affect both gears and bearings. Macropitting occurs when the contact stress in the gear or bearing exceeds the fatigue strength of the material. Wind turbine gears and bearings are typically designed for a 20-year service life. Macropitting that occurs before the end of the design life is an indication that one or more design considerations, such as contact stress, material properties, lubricant condition or applied load, were not met. Macropitting results in craters on the gear tooth or bearing ring (or roller) surface. Beach marks due to the presence of corrosion and lubricant in the crack indicate a fatigue progression process. Macropitting failures can be prevented by reducing loads, improving gear and bearing profiles to reduce stresses, using cleaner steel, or increasing material strength through alloy selection or a heat treatment process.
- Bending fatigue is a failure mode that affects gear teeth. Bending fatigue failure occurs when the stress at the root of the gear tooth exceeds the capability of

the gear material. This can be due to excessive loads, incorrect heat treatment, inclusions in the steel or a notch at the root of the tooth. The appearance of the fracture surface will vary depending on whether the failure is high or low cycle fatigue. Features such as ratchet marks are occasionally present, and those marks indicate multiple crack initiations. Bending fatigue failure can be prevented by decreasing load, increasing gear material strength or optimizing the gear root fillet geometry.

- Axial cracking is a phenomenon that occurs in bearings, almost always on the bearing inner ring. Failures of this type have become very common in wind turbine gearboxes and have been discussed in an article in the June 2013 issue of North American Windpower. The cracks usually propagate in the axial direction which is perpendicular to the direction of rolling. Axial crack failures are most likely to occur in through-hardened bearings (Fig. 1.2).

Fig. 1.2: Axial cracking on bearing ring.

- Some other types of fatigue in bearings such as spalling are also one of the main reasons to cause failure (Fig. 1.3).

(a)

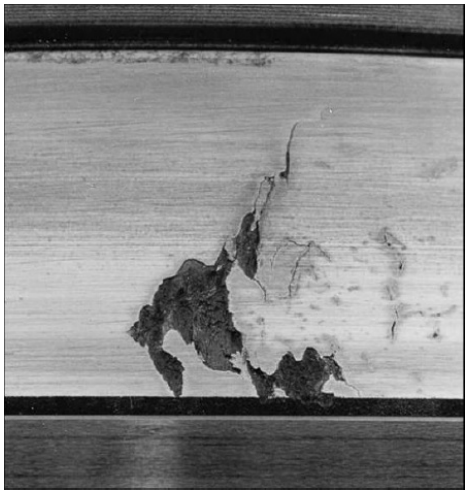

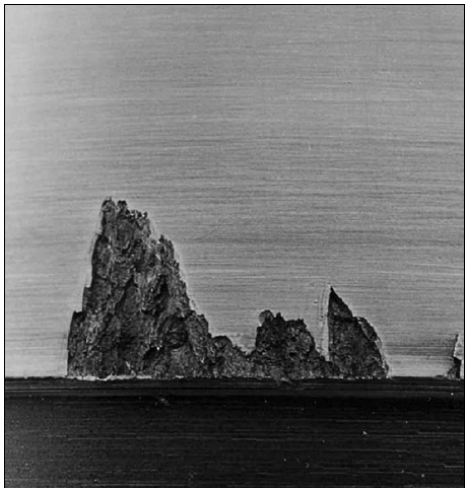

(b) (c)

Fig. 1.3: (a) Material fatigue: Spalling, (b) Material fatigue: Point surface origin (PSO) spalling, (c) Material fatigue: Geometric stress concentration (GSC) spalling.

The wind turbine gearbox failure modes described in the above are some of the

most common ones. The others include case-core separation, plastic deformation, scuffing, polishing, adhesion, abrasion, subcase fatigue, erosion, electric discharge, cavitation, corrosion, and several additional forms of cracking. Regardless of the failure mode type, however, proper and prompt identification is the key to preventing a re-occurrence of any gearbox failure. In this thesis we are mainly focusing on rolling contact fatigue of bearings considering micropitting initiation. In addition, for the gear tooth, both fatigue crack initiation and fatigue crack propagation are studied.

1.2 Rolling contact fatigue

The rotational motion and dynamics of rollers in a bearing give rise to alternate contact between the bearing inner race and the rolling elements. High pressures caused by the contact are developed between the load carrying elements. Due to alternate contact, the contacting elements are subjected to cyclic loading and then stressing. This cyclic nature of stress makes the rolling elements and the inner race susceptible to failure due to fatigue. It is one of the leading causes of failure in rolling element bearings, and this phenomenon is known as Rolling Contact Fatigue (RCF). In addition to rolling element bearings, RCF is also commonly observed in gears, cam-follower mechanisms and rail-wheel contacts. RCF manifests itself in a variety of different mechanisms that ultimately lead to final failure [9]. Subsurface originated spalling and surface originated pitting are the two most dominant mechanisms. These are often competing modes of failure, and the ultimate mechanism that prevails de-

pends on a number of factors, e.g. surface quality, lubricant cleanliness, material quality, etc.

If micro-cracks initiate below the surface, subsurface originated spalling occurs. In other words, the cracks propagate towards the surface to form a surface spall. As Fig. 1.4 shows, these cracks are often found to originate in the region of maximum shear stress below the surface [2]. Factors favoring subsurface originated spalling are smooth surfaces, presence of non-metallic inclusions in the material and absence of surface shear. This mechanism is the dominant mode of failure in rolling element bearings that have smooth surfaces and operate under elastohydrodynamic lubrication (EHL) conditions.

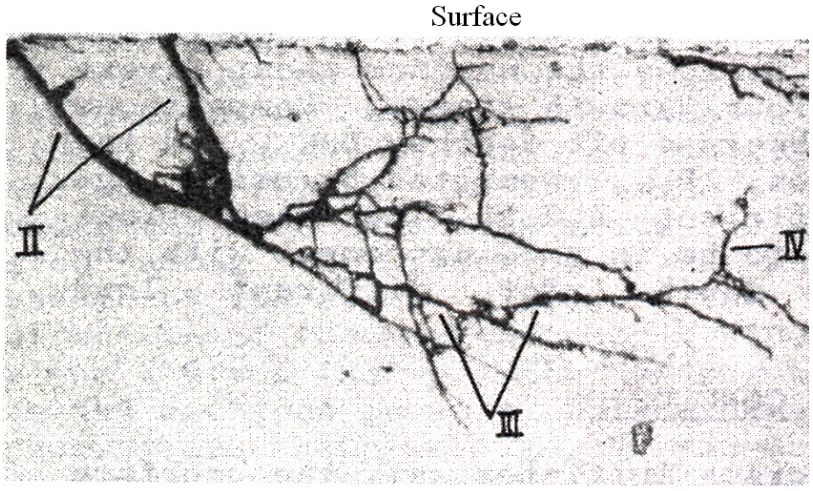

Fig. 1.4: Subsurface cracks in rolling contact fatigue [2].

Surface originated pitting, on the other hand, occurs in cases where surface irregularities in the form of dents or scratches are present. In this phenomenon, cracks initiate at the surface stress concentrators and thereafter propagate at a shallow angle (less than 30 degree) to the surface [10]. When the cracks reach a critical length or depth, they branch up towards the free surface. Then, a piece of surface material is removed, and a pit is formed[3], As shown in Fig. 1.5. This type of failure is common in gears and bearings where substantial sliding occurs between the contacting surfaces.

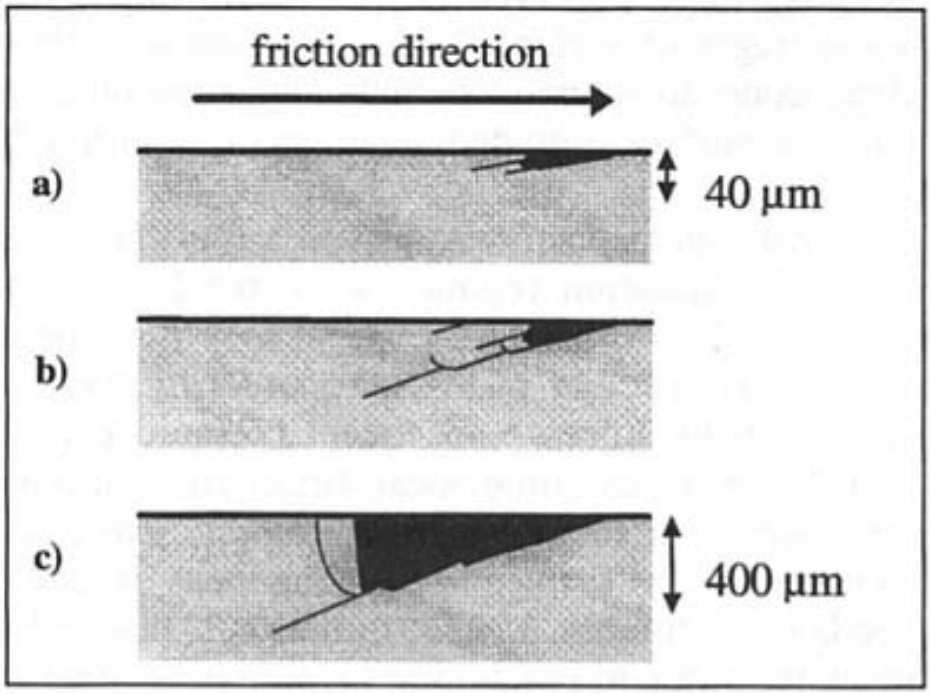

Fig. 1.5: Mechanism of surface initiated pitting [3].

1.3 Tribology

Tribology is the science of interacting surfaces in relative motion, and the related subjects and practices. The nature and consequence of this interaction at the moving interface control the friction, the wear, and the behavior of the lubrication. Understanding the nature of this interaction and solving the technological problems related to the interfacial phenomena constitute the essence of Tribology.

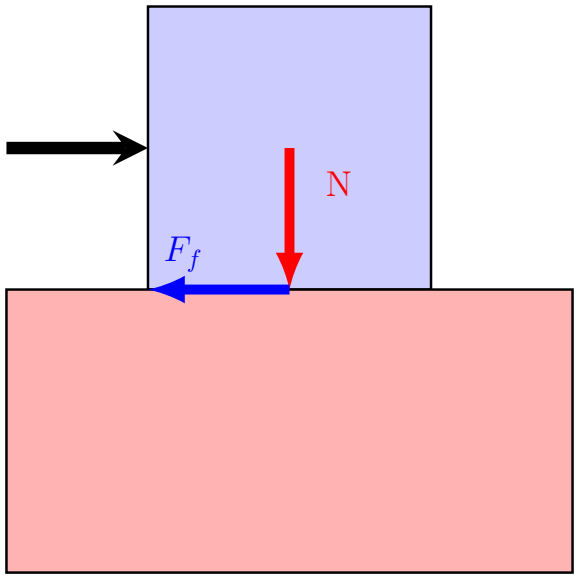

Fig. 1.6: Schematic view of Amontons friction law. N denotes the normal load and F_f represents the friction force.

The basic law of friction was first derived by Leonardo da Vinci in 1519, and was rediscovered by Amontons in 1699 [11]. Based on Fig. 1.6, the law indicates that:

1. The frictional force F_f is proportional to the normal force N, and the coefficient of friction $= F_f/N$ is a constant in a given friction system.
2. Friction is independent of the contact area between two given surfaces.

This observation was later verified by Coulomb in 1785 by distinguishing between the static friction and the kinetic friction. The static friction force is the force resisting sliding, and it needs to be conquered in order to trigger the motion of sliding. The kinetic friction is independent of the sliding speed, which is called the third law of friction. However, Coulomb incorrectly presented that the friction was only due to interlocking surface asperities and claimed that the asperities lifting over their counterparts on the other surface consumed energy. He proposed that a lubricant could reduce friction by filling in the gaps between the asperities. In the nineteenth century, many researchers were also able to accept his roughness theory of friction based on repeating Coulombs experimental results. Nevertheless, there were two drawbacks with this theory. At first, it is difficult to explain how the friction energy can be produced and dissipated. Secondly, not all of the dissipated energy can be converted to heat during sliding.

Vince modified Coulombs theory by stating that the adhesion or cohesion between the surfaces mainly contributed to friction. The effects of adhesion and roughness were observed on some specific surfaces, but only adhesion was shown to be the main factor that determined the friction force. Their explanation indicated that the static friction coefficient is higher than the kinetic friction coefficient. At the nanoscale, the molecular adhesion between surfaces is caused by short range inter-molecular

forces. When surfaces are sliding relatively, the surface molecules are removed from their equilibrium positions, and when that displacement exceeds a certain distance the molecules return to their equilibrium position with the vibrational motion. However, Vinces theory was not able to explain the material transitions, such as wear, which are generally observed when two surfaces experience dry sliding under a normal load. Bowden and Tabor [12] presented that the predominant friction effect caused a strong adhesion between two surfaces at real contact points. When a surface slides on another one, the junctions of real contact points must shear or be sheared. However, Their assumption that the friction force was the primary force required to shear junctions could not explain why the substantial friction existed even in cases without wear.

A surface force apparatus (SFA) was developed to measure the friction at the atomic scale, with which Israelachvili [13] observed the first direct evidence for wear-free friction. Surfactant mono-layers were also observed to exhibit different states including solid-like, amorphous, or liquid-like. The existing of one or more states depends on the atmosphere, temperature, velocity or related parameters [13, 14]. Numerous researches have been conducted using novel experimental tools which allowed the tribologists to be exposed to the atomic scale. Nanotribology [15] is concerned with experimental and theoretical research ranging from the atomic and molecular scale to the micro-scale. In macrotribology, surfaces with a large mass are usually studied subject to heavy loads. It inevitably causes wear, and the bulk properties of components dominate the friction phenomena. In nanotribology, however, the friction

systems tend to have a light load so wear is negligible and the properties of the interface dominate the friction phenomena.

1.4 Lubrication effects on contact

Lubricant is used to reduce wear, to lower friction, and to remove heat. The behavior of sliding surfaces is affected and modified by the lubrication between the surfaces. The scientific studies of lubrication started when Reynolds discussed the feasibility of a theoretical treatment of film lubrication. When the load is fully supported by a fluid film, the surfaces are completely separated. This is generally referred to as hydrodynamic lubrication [16].

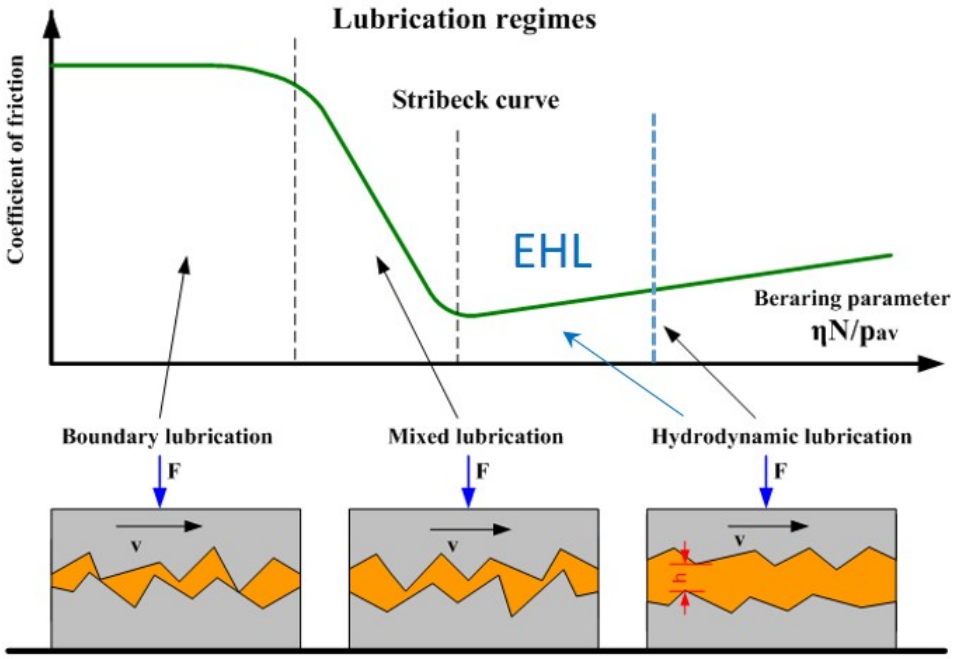

Fig. 1.7: Lubrication regimes: boundary, mixed, elastohydrodynamic and hydrodynamic.

A recapitulative friction diagram, shown in Fig. 1.7, which distinguishes different lubrication regimes, was first proposed by Stribeck in 1902, based on extensive experiments on lubricated journal bearings. The Stribeck diagram shows how the friction force or the coefficient of friction is expected to vary with the sliding speed, depending on which type of friction regime is operating (Fig. 1.7).

When the load is heavy and/or the speed is low, the hydrodynamic or hydrostatic pressure may be unable to fully support the load. Therefore, the surfaces come into contact at their asperities. The amount and extent of asperity contact depends on the following factors including surface roughness, fluid film pressure, normal load,

hardness, and elasticity of the asperities, etc. Many of the asperities undergo elastic deformations so that the normal load is supported by the asperities and a thin fluid film, e.g. the lubricant. This condition is generally referred to as elastohydrodynamic lubrication (EHL) [17]. This theory assumes continuum mechanics and does not consider the effects of wear or a third body such as wear debris. In addition, no chemical effect between the asperity and the lubricant is considered.

As the contact pressure increases beyond the EHL condition, it causes the contacting asperities to deform plastically, the number of contacting asperities (contact area) to increase, and the thickness of the fluid film to decrease. At this region the lubricant is no longer completely supporting the load, and the surfaces start interacting at the asperity level. It causes an increase in friction as the number of contacting asperity increases. Therefore, the friction means the force to shear the lubricant and the junctions between asperities. This condition is referred to as mixed lubrication.

When the thickness of the average fluid film falls below the average surface roughness, surface asperity contact effectively supports the load. It leads to the occurrence of wear, surface deformation, abrasion, adhesion, and fatigue. In most cases, chemical reactions between the lubricant molecules and the asperity surfaces due to frictional heating produce a boundary chemical film which can be either beneficial or detrimental in terms of wear. The combination of a load shared by the asperities and the occurrence of chemical reactions creates a lubrication region commonly referred to as the boundary lubrication (BL) region.

In practice, determining whether the system is a pure EHL region or a BL region is

difficult, since the surfaces have a range of asperity height distributions. Two surfaces in contact produce a range of stresses that are distributed within the contact zone. In reality it tends to be a mixed region because some asperities are in a hydrodynamic lubrication mode, some in an elastohydrodynamic lubrication mode, and the others in a boundary lubrication mode. It is worthy to mention that, as wear occurs, the surface topography changes, and it eventually affects the contact area and the distribution of asperity stress.

1.5 Friction and lubrication at nano-scale

Although the lubrication approximation originates from thin films, there is a limit to its validity. When two separating surfaces are sliding with a lubricant whose thickness is comparable to the molecular scale, the continuum assumption, one of the basic assumptions of approximation, breaks down. In this case the Reynolds equation must be modified or replaced by other mathematical models. From a practical perspective, most surfaces in engineering applications are rougher than the nanometer, so it is highly unlikely that an ideal molecular lubrication exists as a unique lubrication mode. However, it is often presenting in sub-regions of mixed or boundary contacts, where particular effects such as lubricant solidification and viscosity enhancement can emerge for molecularly confined films between interacting asperities.

Recent developments in system designs have resulted in decreasing physical sizes, which demands a fundamental understanding of friction and lubrication at nano-

scale. Experimental results have shown that in the interfacial region of only a few molecular diameters, the confined fluid has very different physical properties than in the bulk region. For example, one of the common assumptions in the fluid mechanics is the no-slip boundary condition which has been proved to be invalid in thin film lubrication at nano-scale. In addition, surface roughness can be found at all length scales, from macro-scale to nano-scale. In boundary lubrication, some surface regions are fully separated by lubricant while other asperities are under direct contact. The surface roughness, lubricant and adhesion force together determine the contact condition between two surfaces. Therefore, a fully understanding of the fundamental mechanism of friction and lubrication between rough surfaces at nano-scale becomes very important.

1.6 Multiscale modeling and simulation of rolling contact fatigue

In this thesis, a multiscale modeling and simulation framework is presented to study rolling contact fatigue and predict the fatigue life. The multiscale model include a molecular model of lubricant and a continuum model of rolling contact component. The aims of this work include:

1. Develop a molecular model of lubricant, and conduct molecular dynamics simulation to calculate the friction coefficient between rolling contact surfaces.
2. Pass the calculated friction coefficient to the finite element model of rolling contact component to predict rolling contact fatigue life of bearing.

3. Study contact fatigue crack initiation and propagation of gear teeth.
4. Study other continuum methods, including the peridynamics and the smoothed particle hydrodynamics as the alternate tools for the continnum model of the proposed mutliscale framework.

This work started with a review in chapter 2 on friction and lubrication at nano-scale from experiments and numerical simulations. Particular phenomena at nano-scale were presented, including stick-slip motion, solvation force, and lubricant solidification, etc. Moreover, the simulation results were divided into three main categories: dry contact, confined thin film, and lubricated surface contact. There were a limited number of MD simulation works that have been done on lubricated surface contact, particularly lubricated multi-asperity contact; therefore, it is necessary to extend current models to lubricated multi-asperity contact, which can represent real surface contact at nano-scale. MD simulations of confined thin film with atomic flat surfaces and different amount of lubricant are conducted. The effects of liquid-solid interaction, molecular chain length, and branch on friction are discussed. The effects of nano particles (debris) and temperature on coefficient of friction are also studied in this chapter. The coefficient of friction, which is obtained from molecular dynamics simulation, will be passed to the continuum model of rolling contact component to study fatigue phenomena in next chapter.

In Chapter 3, the continuum modeling and simulation of bearing fatigue are presented. Finite element approach and E-N material data are employed to predict the fatigue crack initiation life and its location. The friction coefficient which is calcu-

lated in the molecular model, described in Chapter 2, is used in the continnum model to apply more accurate boundary conditions. In Chapter 4, fatigue crack initiation and propagation of a gear-tooth under moving Hertzian contact load are studied. In addition composite patches are considered to repair the cracked gear-tooth so that the fatigue life of the gear-tooth can be enhanced.

In Chapter 5, we studied the Peridynamics method, and applied it in the continuum model to predict rolling contact fatigue lives. It should be noted that the peridynamics approach is a continuum based version of MD simulation. Fatigue crack initiation and propagation are simulated in a roller contact fatigue model in this chapter.

CHAPTER 2
MOLECULAR MODELING AND SIMULATION OF LUBRICANT IN ROLLING CONTACT SYSTEMS

2.1 Introduction

As one of the key elementary mechanical components, ball and roller bearings are used to allow rotary motion and support significant loads. The rotational motion and dynamics of rollers, i.e. rolling elements, in a bearing give rise to alternate contact between the bearing inner race and the rolling elements. High pressures caused by these contacts are developed between the load carrying elements. Due to alternate contact, the contacting elements are subjected to cyclic stressing. This cyclic nature of stress makes the contacting elements susceptible to failure due to fatigue. It is one of the leading causes of failure in bearings, and this phenomenon is known as Rolling Contact Fatigue (RCF). RCF is also commonly observed in gears, cam-flower mechanisms and rail-wheel contacts. Therefore, it is crucial to understand mechanisms of RCF and predict fatigue life during machinery design.

There have been several numerical approaches to study RCF of bearings or other mechanical components [18]. These models can be classified into either probabilistic engineering models or deterministic research models. The probabilistic engineering models include the formulas to predict RCF life, and the formula parameters were obtained from extensive experimental testing. Lundberg and Palmgren [19, 20] proposed the first engineering model, the L-P model, to predict the bearing life based on the assumption of crack initiating at a subsurface weak point in the material. The

Weibull statistical strength theory was applied in their model. In order to overcome the limitations of the L-P model, Ioannides and Harris [21] modified the principles of crack initiation and proposed another new model, the I-H model, to predict the bearing lives. Based on the given defect's severity distribution, Tallian [22] proposed a statistical model to compute fatigue crack propagation life. Then, Kudish and Burris [23] modified Tallian's theory by considering more material and loading parameters. However, this model didn't include the fatigue crack initiation life.

The deterministic research models were developed to estimate the fatigue crack initiation life or the crack fatigue propagation life based on mechanics of the failure process. Keer and Bryant [24] developed the first deterministic research model to calculate the fatigue lives for rolling Hertzian contacts. They used two-dimensional fracture mechanics and only considered the fatigue crack propagation life. Considering both the crack initiation life and the crack propagation life, Zhou and co-workers [25, 26] proposed a new life prediction model taking into account the accumulated damage. Another fatigue life prediction model was presented by Bhargave et al. [27] based on plastic strain accumulation under the cyclic contact stress. Other similar prediction models can be found in [28–30]. However, the assumption of homogeneous materials in the contact region was employed in most deterministic research models. To overcome this limitation, a few models, including finite element models, were developed to take into account the micromechanical material behavior in the contact region. A so-called Voronoi finite element method (VFEM) was proposed by Jalalahmadi and Sadeghi [31]. With the implementation of a fatigue life criterion

[32], VFEM can be used to study the effect of material micromechanical behavior on rolling contact fatigue.

When using the above models to study RCF, the mechanical components, i.e. rolling elements in bearings, were assumed to be well lubricated. On the other hand, the friction force was prescribed on the contact surface to calculate the RCF lives. Consequently, the lubrication effect was neglected. It has been known that partially lubricated mechanical components and the debris in the lubrication would dramatically reduce the mechanical component's RCF lives because of the large friction force on the contact surface. Therefore, it is necessary to consider the lubrication effects when predicting the RCF lives of bearings or other lubricated mechanical elements.

Lubricant is used to reduce wear, to lower friction, and to release heat. The behavior of sliding surfaces is affected and modified by the lubrication between them. The scientific study of lubrication, in tribology community, started when Reynolds in 1886 discussed the feasibility of a theoretical treatment of film lubrication. A recapitulative friction diagram was first proposed by Stribeck in 1902 after extensive experiments have been conducted on lubricated bearings to distinguish different lubrication regimes. The diagram indicates how the friction force or the coefficient of friction is changed due to various pressures.

Although the lubrication approximation originated from thin film studies, there is a limitation due to its continuum mechanics assumptions. When two separating surfaces are sliding under the contacting load, the lubricant between surfaces has the thickness comparable to the molecular scale. Therefore, the continuum assumption

becomes invalid. For example, one of the common assumptions in the fluid mechanics is the no-slip boundary condition which has been proved to be invalid in thin film lubrication at nanoscale. In addition, surface roughness may be considered when the length scale is down to the nanoscale. In the case of boundary lubrication, some surface regions are separated by lubricant while the others are under direct contact due to the existing asperities. Generally, the surface roughness, lubricant and adhesion force together determine the contact mechanism between two surfaces. Therefore, a fully understanding of the fundamental mechanism of friction and lubrication between contact surfaces at nanoscale becomes very important to predict RCF lives.

Among many powerful numerical methods to elucidate nanoscale phenomena, molecular dynamics (MD) has outstanding advantages to provide the steady state of a system as well as simulate the non-equilibrium process under various conditions. It can help to investigate the unobservable tribological aspects, including the lubricant behavior between contact surfaces at nanoscale. A review of the molecular mechanisms of tribology in thin films and at surfaces was brought forward in [33]. Zhang [34] employed MD to conduct friction analyses and wearability evaluation. In addition, MD was adopted to simulate heat transfer at the interface of contacting solids [35], and to examine the effects of surface roughness on friction [36–40].

With the development in nano engineering and nano materials science, nanoparticles have been introduce into lubricants. The nanoscale additives were reported to be capable of improving the friction performance of lubricants in anti-wear and friction-reduction properties [41–43]. Some nanoparticles were shown to play a favorable role

as solid lubricants under severe conditions [44, 45]. Ghaednia and co-workers [46] conducted MD simulations to explore the interactions between the nanoparticles and the lubricant or the contact surfaces. They found that the presence of nanoparticles reduced friction. The friction reduction mechanism indicated that nanoparticles in the thin film elastohydrodynamic lubricant regime restrict only a few layers of lubricant molecules to slide (shearing) on each other. It should be noted that nanotubes also showed promising properties for the lubrication [47, 48].

A new multiscale model for studying rolling contact systems is proposed in this thesis. The molecular model of lubricants is carried to study the friction phenomenon between rolling contact surfaces. The calculated friction coefficient is then passed to a continuum FEM model to predict rolling contact fatigue life. In this chapter, the molecular modeling and simulation of lubricant is introduced. The calculated friction coefficient will be passed to the continuum model of rolling contact components for fatigue life prediction. The continuum approaches for rolling contact fatigue life prediction are described in the following chapters.

2.2 Molecular modeling of lubricant

2.2.1 Molecular dynamics

MD simulation, which is a numerical technique used to calculate the equilibrium and transport properties of a classical many-body system, is adopted to study hydrodynamic lubrication in this chapter. In the MD simulation, the atoms or

molecules in the simulated system follow the laws of classical mechanics. The motion of an atom, e.g. atom i, with mass m_i, is due to its interaction with other atoms in the system according to Newton's second law:

$$m_i\vec{a}_i = \vec{f}_i = -\Delta u(\vec{r}_i) \tag{2.1}$$

where $\vec{a}_i$ is the acceleration of atom i, and the interatomic force, $\vec{f}_i$, applied on atom i , is derived from the total potential energy due to its interaction with other atoms,

$$u(\vec{r}_i) = \sum_j u_{ij}(\vec{r}_i, \vec{r}_j) \tag{2.2}$$

where $\vec{r}_i$ and $\vec{r}_j$ are the atomic positions of atoms i and j respectively. u_{ij} is the potential function to describe the interaction between atoms i and j.

MD simulation requires solving the equations of motion, i.e. Eq.2.1, to obtain the atomic trajectories. In this chapter, the Velocity Verlet algorithm is employed as the time integration algorithm since it achieves a considerable accuracy [49].

The atomic position, $\vec{r}_i(t)$, velocity, $\vec{v}_i(t)$, and acceleration, $\vec{a}_i(t)$, at the time $t + \delta t$ (here δt is the time step) can be obtained from the equivalents at the time t as below:

$$\vec{r}_i(t+\delta t) = \vec{r}_i(t) + \vec{v}_i(t).\delta t + \frac{1}{2}\vec{a}_i(t).(\delta t)^2 \tag{2.3}$$

$$\vec{v}_i(t+\frac{1}{2}\delta t) = \vec{v}_i(t) + \frac{1}{2}\vec{a}_i(t).\delta t \tag{2.4}$$

$$\vec{a}_i(t+\delta t) = -\frac{\partial u(\vec{r}_i)}{\partial \vec{r}_i}.\frac{1}{m_i} \tag{2.5}$$

$$\vec{v}_i(t+\delta t) = \vec{v}_i(t+\frac{1}{2}\delta t) + \frac{1}{2}\vec{a}_i(t+\delta t).\delta t \tag{2.6}$$

At each iteration, the atomic position for next time step is updated first, and then the velocity at the half time step is obtained through the acceleration at the previous

time step. Afterwards, the acceleration at the next time step is calculated from Newton's second law. At last, the velocity at the next time step is updated by adding the velocity increment with the consideration of the updated acceleration. The choice of time step t is essential. Its value should be at least an order of magnitude less than the typical time of the system that is defined by the phonon frequencies or the ratio of velocity to acceleration.

One of key issues in MD simulation of tribological phenomena is the temperature regulation because the work done during two walls sliding from each other is ultimately converted into a random thermal motion at the nanoscale. The temperature of the simulated system would increase infinitely if only modeling the simulated system as an isolated one. To model the heat dissipation from the simulated system to the surrounding media, a numerical heat bath is implemented in MD simulations. A classic approach to adding or subtracting kinetic energy to the system is multiplying the velocities of all particles with the same global factor. In this simplest version of velocity rescaling, the factor is chosen to keep the kinetic energy constant at each time step, so that the temperature can be maintained. However, there might be fluctuations in the kinetic energy in a true constant temperature ensemble. Alternatively, the equations of motion can be modified to gradually scale the velocities so that the average kinetic energy can be maintained over a longer time scale. The Nose-Hoover method [50, 51] is one of these methods, and it is used in this chapter to conduct MD simulations of hydrodynamic lubricants at a constant temperature.

The Nose-Hoover method couples the simulated system with a heat bath, and the

heat will be transferred back and forth between the system and heat bath in order to keep the system temperature relatively constant. In this method, Newton's second law of motion is modified with an additional term related to the heat bath:

$$\vec{a}_i(t) = \frac{\vec{f}_i(t)}{m_i} - \zeta(t)\vec{v}_i(t) \tag{2.7}$$

The coefficient of friction ζ is defined as

$$\frac{d}{dt}\zeta(t) = \frac{N_F}{Q}(k_B T(t) - k_B T_0) \tag{2.8}$$

in which N_F is the degrees of freedom and equals to $3N + 1$, with N as the number of particles in the simulated system, $T(t)$ is the instantaneous temperature, T_0 is the heat bath temperature or the desired temperature, and k_B is the Boltzmann constant. The heat transfer rate is determined by the fictitious mass parameter Q.

2.2.2 Molecular model of lubricant system

The MD simulations in this study were carried out with the Larger-scale Atomic Molecular Massively Parallel Simulator (LAMMPS) code plimpton95. The schematic view of the simulated system is depicted in Fig.2.1. The MD model of lubricant system includes the lubricant chains that are confined between upper and lower Fe walls. The solid walls are divided into six layers, including upper and lower rigid layers, thermostat layers, and free layers. Linear alkanes with the chain length of C_8 are considered as the fluid film of lubrication, as shown in Fig.2.2, in this chapter. There are a total of 1950 chains in the simulated model. Most industrial applications

indicate a thin lubricant thickness of only several nano meters [52, 53] under a high normal pressure. In this study, the initial film thickness of about 5 nm is used to model the rheological and frictional behavior of the lubricant.

The whole MD simulation process includes three main stages named relaxing, compressing, and shearing. In the relaxing stage, the upper and lower walls are fixed to keep the system height constant, and the randomly distributed lubricant alkane chains can move freely. It is essential to have lubricant chains becoming fully relax. In other words, the system will be at thermodynamic equilibrium state. In the compressing stage, a uniformly distributed external load is applied onto the upper rigid layer while the lower rigid layer remains fixed. To investigate tribological phenomena of the system subject to external loadings, it is generally desirable to keep the interface as undisturbed by the external force as possible. Therefore, it is crucial to apply any external forces and constraints to the outmost layers, i.e. rigid layers shown in Fig.2.1. The temperature regulation is usually applied on the middle region of the upper or lower solid layer, named the thermostat layers. Therefore, the contacting solids are undisturbed by regulating the thermostat regions. The lubricant is compressed in the second stage until the system reaches to the thermodynamic equilibrium state again.

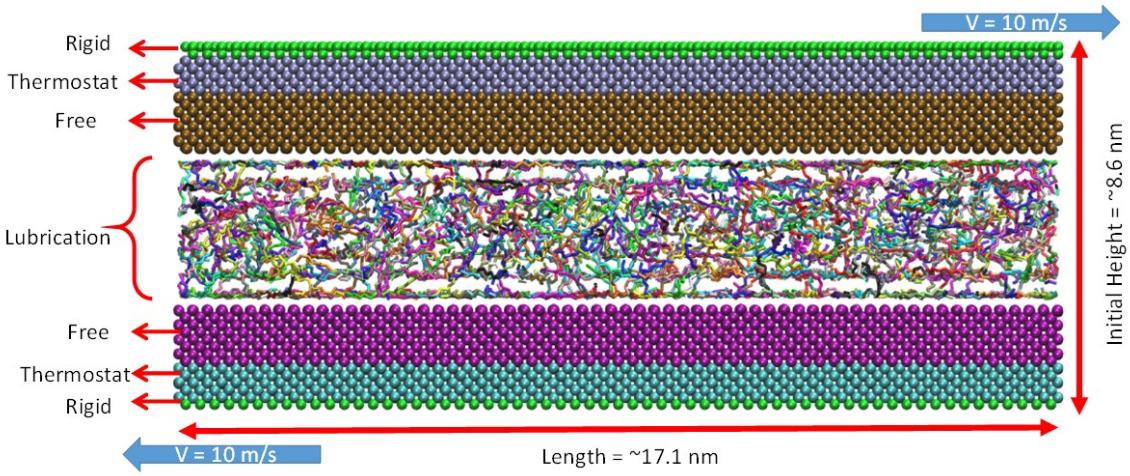

(a)

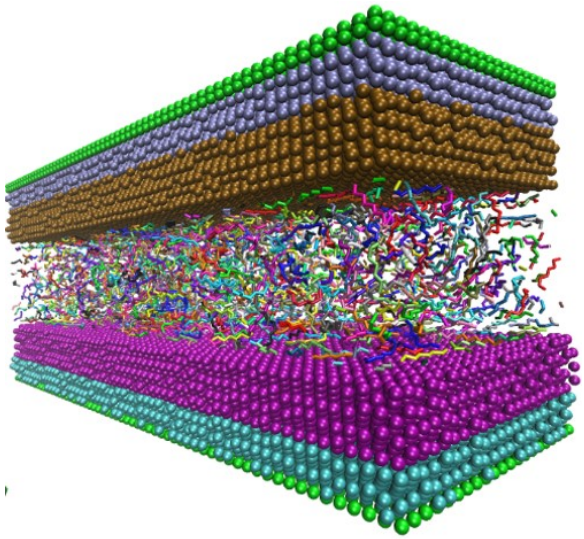

(b)

Fig. 2.1: The molecular model of thin film lubrication between two contact surfaces : a) Schematic view; and b) three-dimensional view.

At the last stage, shearing, a constant velocity of 10 m/s is applied onto the upper and lower rigid layers along the longitudinal direction, as indicated in Fig.2.1

(a), so that the lubricant is sheared. This sliding velocity conduction has been widely used in MD simulations of thin film lubrication as it enables the simulation to obtain a required sliding distance within a reasonable calculation time [37, 38, 52, 54]. In addition, the constant velocity mode makes it easy to record the friction forces.

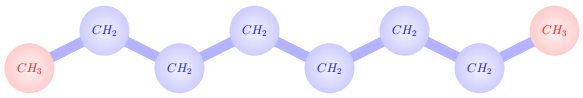

Fig. 2.2: Schematic view of an alkane with 8 chain in used as the lubricant. The red atom is the united atom of CH_3 and the blue atom stands for that of CH_2.

2.2.3 Potential functions

In the MD simulation, the selection of proper potential functions is important to describe interaction between molecules. In the molecular model of lubricant system, the alkane molecules are represented via an optimized United Atom (UA) potential TraPPE-UA, and the Fe atoms in solid walls are modeled by the embedded atom method (EAM) potential. The non-bonded interactions among alkane molecules as well as the liquid-solid interaction are modeled through the Lennard-Jones (L-J) potential with the Lorentz-Berthelot combination rules.

2.2.3.1 Bonded interaction in a single alkane chain

A liquid lubricant, such as n-alkanes, has two unique properties compared to solids such as Fe, Al, Au, etc. At first, unlike a solid with a well-ordered crystalline structure, the liquid by nature has no ordered internal structure. The lubricant can flow and the lubricant molecules can pass one another during the motion. Secondly, the lubricant molecules are typically made of flexible chains and branches which include bonded, angular, and torsional interactions.

Linear alkane chains are used in this chapter to model the lubricant, and the molecular architecture includes bond stretching, angle bending, and torsion. The TraPPE-UA potential has been well developed to simulate both linear and branched alkanes [55, 56]. It was extended to simulate molecules in short chains [57, 58] which has been widely used to model surfactants and lubricants. Generally, the UA potential is a sum of the covalent bond stretching, angle bending, and torsion presented as,

$$E_{bond} = \frac{K_b}{2}\left(r - r_0\right)^2 \tag{2.9}$$

$$E_{bend} = \frac{K_\theta}{2}\left(\theta - \theta_0\right)^2 \tag{2.10}$$

$$E_{torsion} = c_0 + c_1\left[1 + cos(\alpha)\right] + c_2\left[1 - cos(2\alpha)\right] + c_3\left[1 + cos(3\alpha)\right] \tag{2.11}$$

The potential parameters for the alkane chains are listed in Table 2.1.

Table 2.1: Potential parameters for alkanes

Bond	$K_b(eV/\mathring{A}^2)$	$r_0(\mathring{A})$		
$C-C$	39.0279464	1.54		
Angle	$K_\theta(eV/rad^2)$	$\theta_0(deg)$		
$C-C-C$	5.3858393	114		
Dihedral	$c_0(eV)$	$c_1(eV)$	$c_2(eV)$	$c_3(eV)$
$C-C-C-C$	0	0.030594	-0.005876	0.068190

2.2.3.2 Liquid-solid interactions and other non-bonded interactions

The interfacial interaction between surfaces and lubricant determines how surfaces influence the structure of confined lubricants and interfacial sliding [59, 60]. A wide range of potentials have been adopted in MD simulations in tribology community. For example, the simple ideal springs [52, 61] and sine-wave potentials are often used. Another potential function, the L-J potential [54, 62], gives a realistic representation of typical inter-atomic interactions. The L-J potential is a two-body potential commonly used for non-bonded interactions between atoms or molecules. In a molecular model of lubricant, an L-J particle may present a single atom on the chain (explicit atom model), a CH_3 segment (united atom model), or even a segment consisting of several CH_2 units in a coarse-grained model. Here, the L-J potential is used to describe the interactions between a pair of CH_3 and/or CH_2 segments, which are on two different alkane chains or separated by more than four segments along a single alkane chain. In addition, the liquid-solid interaction, i.e. the interaction between a CH_3 or CH_2 segment and an Fe atom, is also modeled via the L-J potential.

The commonly used 12-6 L-J potential has the following form:

$$U(r_{ij}) = 4\varepsilon \left[\left(\frac{\sigma}{r_{ij}} \right)^{12} - \left(\frac{\sigma}{r_{ij}} \right)^{6} \right] \tag{2.12}$$

where r_{ij} is the distance between particles i and j, ε is the L-J interaction energy, and σ is the L-J interaction diameter. The parameters of dissimilar interactions can be computed by the Lorentz-Berthelot combining rules:

$$\begin{cases} \sigma_{ij} = \frac{1}{2} \left(\sigma_{ii} + \sigma_{jj} \right) \\ \\ \varepsilon_{ij} = \sqrt{\varepsilon_{ii} \varepsilon_{jj}} \end{cases} \tag{2.13}$$

The potential parameters for the alkanes are listed in Table 2.2 As Eq. 2.12 shows, the well-depth determines the strength of the interaction between the surface and the lubricant. The L-J parameters for liquid-solid interaction are guided by the mixing rule in Eq. 2.12, so the liquid-solid interaction can be controlled by using a range of well-depth parameters of the L-J potential of the surface (Fe).

Table 2.2: Potential parameters for inter-atomic interactions

LJ 12-6 potentials	$\sigma(\mathring{A})$	$\varepsilon(eV)$	Mass (g/mol)
CH_3	3.75	0.008444	15.0351
CH_2	3.95	0.003963	14.0272
CH	4.68	0.000861	13.0191
Fe	2.321	0.04097	55.8450

It shall be noted that the selection of potential functions depends on the studied physical phenomenon. A simple spring model can be used for thin film lubrication,

and the wall atoms are attached to their lattice position with a spring in the molecular model. However, it is more common to use the L-J potential in modeling thin film lubrication or surface sliding. In studying thin film lubrication, the main interest is to investigate the behavior of the lubricant between two sliding walls. The L-J potential for the interaction between the wall atoms and the lubricant molecules is acceptable as long as the parameters are chosen properly. Moreover, reasonable results can be gained by using the L-J potential for the atoms of surfaces when two surfaces are sliding against each other [54]. Another significant advantage of using this potential is the computational efficiency.

2.2.3.3 Solid (Fe)

In the embedded atom method (EAM) [63] for Fe, the total potential energy has a pairwise part and a local density part:

$$E = \sum_{i=1}^{N-1} \sum_{j=i+1}^{N} \varphi(r_{ij}) + \sum_{i=1}^{N} (\Phi(\rho_i)) \tag{2.14}$$

where the subscripts i and j label distinct atoms, N is the number of atoms in the system, r_{ij} is the distance between atoms i and j

$$\rho_i = \sum_{j} \Psi(r_{ij}) \tag{2.15}$$

All functions above are represented as sums of basis functions:

$$\varphi(r) = \sum_{k=1}^{n^{\varphi}} a_k^{\varphi} \varphi_k(r) \tag{2.16}$$

$$\Psi(r) = \sum_{k=1}^{n^{\Psi}} a_k^{\Psi} \Psi_k(\rho) \tag{2.17}$$

$$\Phi(r) = \sum_{k=1}^{n^{\Phi}} a_k^{\Phi} \Phi_k(\rho) \tag{2.18}$$

where φ_k, Ψ_k, and Φ_k are the basis functions, and a_k are coefficients to be fitted to material properties. Those coefficients in the EAM for Fe can be found in [63].

2.2.4 Periodic boundary condition

Periodic boundary conditions are the approach available to simulate a large molecular system by modeling a small unit cell adjacent to periodic mirror images at each side. For example, Fig. 2.3 shows a sketch of periodic boundary conditions in a 2D system.

The gray lattice in the middle is the unit cell under simulation. The other eight white lattices are the mirror images of the unit cell, and each mirror image has atoms with the same states as the simulated one. When an atom moves out of the lattice, an equivalent atom in a mirror image simultaneously moves into the lattice, such as atom #2 which is indicated by the arrows. Under periodic boundary conditions the number of atoms in the simulated cell was kept as a constant. Another principle of periodic boundary conditions is that there should be a cut-off distance to include the related atoms in the mirror images for non-bond interaction. Atom #3, for example, actually interacts with the #1 atom in the F cell rather than the #1 atoms in the simulation cell or other images. The cut-off distance should meet the requirement $r_c \leq L/2$.

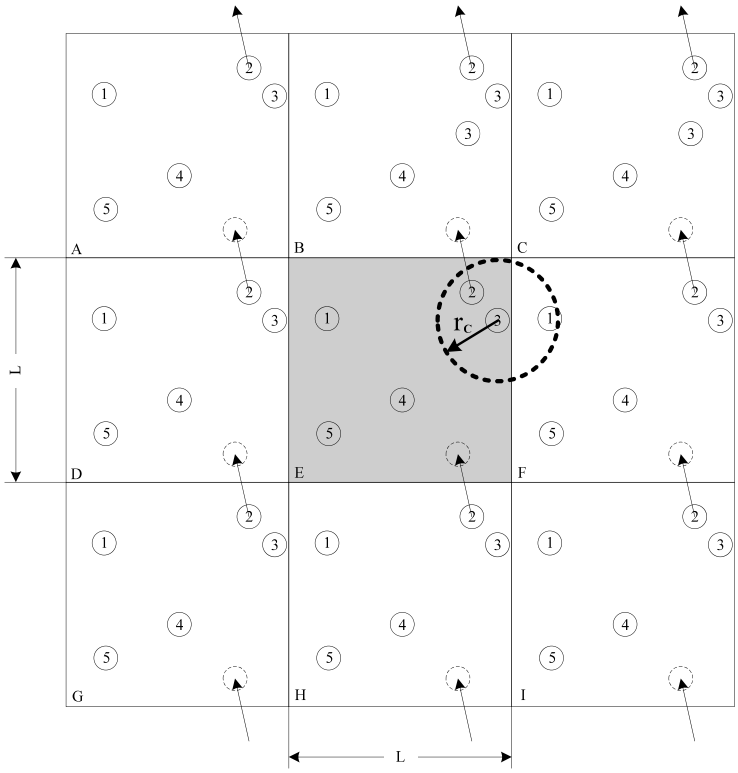

Fig. 2.3: 2D schematic view of periodic boundary conditions.

Two types of molecular dynamic simulations (thin film lubrication, contaminated lubrication with nano-particle (debris)) are conducted in this thesis. Due to its intrinsic property of small size, the compliance described through the spring attached to the outermost layer could be ignored because the bulk material of surface is small and the effect of elasticity of surface is minor. Compared with the constant force mode, the constant velocity mode is more widely used in the atomistic computer simulations. Specifically, under a large normal load, the friction force could be huge and varying. If the contacting surfaces have large surface roughness, a huge driving force

is needed to make the surfaces slide against each other under a large normal load. Moreover, the constant velocity mode is easy to record the friction forces. Therefore, the constant velocity mode is used in this thesis.

Hydrodynamics and elastohydrodynamics have been successfully used to describe micro-thick films [17], however; as the thickness of the confined liquid approaches to only a few molecular diameters, these theories begin to break down. Both experiments and simulations have proved that there are significant changes in the static and dynamic properties of fluid films when the thickness decreases from microns down to the atomic scale.

Experimental results indicate that tribological performance such as the bulk viscosity depends on the shape and length of the lubricant molecules. Generally, long-chain and branched molecules have higher viscosities than short-chain and linear ones [64]. In addition, in small-scale flows, the assumption of a non-slip boundary condition becomes invalid [65, 66] while in fact, an interfacial slip occurs. The properties of lubricant, such as chain length and branch, by nature, have an essential effect on its performance, and when that is combined with the effect of small confinement, a complete understanding of lubricants behaviour at the atomic scale is required. In this chapter the molecular dynamic simulation of thin film lubricant is carried out. The lubricants having various chain lengths and different temperatures are considered in the simulation. The effect of Nano particles (debris) on the coefficient of friction is also studied in this chapter.

2.3 Results

2.3.1 Effect of chain length

It has been found that the chain length of linear alkanes plays an essential role in determining lubricant's static and dynamic properties [67, 68]. In this section, three different chain lengths of C_8, C_{16}, and C_{20} for the n-alkane lubricant are considered to study the effect of the chain length on mechanical behavior of lubricant in the molecular model. The normal pressure which is applied on the upper wall is 1500 MPa. Fig. 2.4 shows a schematic view of each case and a zoomed view of the their lubricant chains.

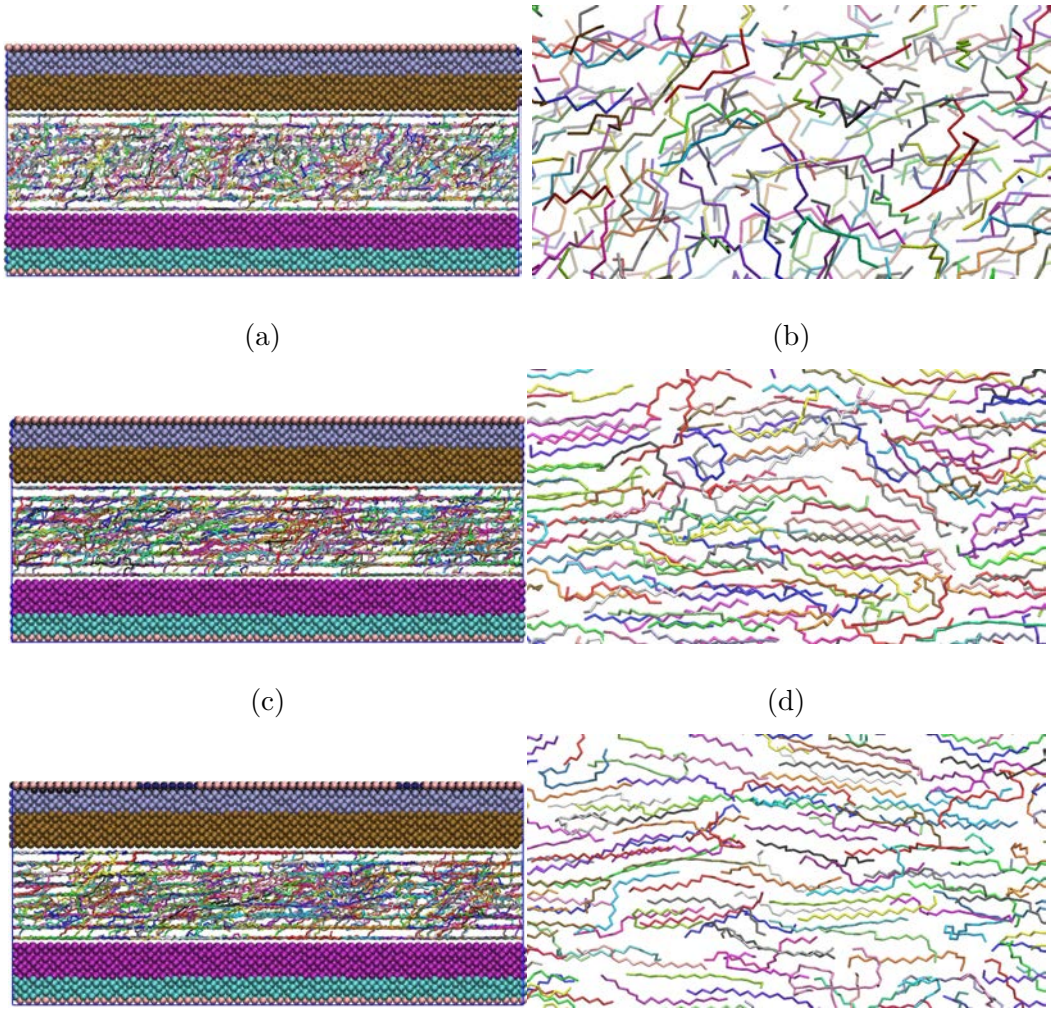

Fig. 2.4: Schematic view of thin film lubrication model in MD simulation. (a) Model with C_8 lubricant; (b) A view of C_8 chains; (c) Model with C_{16} lubricant; (d) A view of C_{16} chains; (e) Model with C_{20} lubricant; (f) A view of C_{20} chains.

As it is mentioned before, in the simulation after the relaxation, the normal pressure is applied onto the upper wall atoms till the simulated system reaches to the

equilibrium state again. Fig. 2.5 indicates the variation in the system height under 1500 MPa for different chain lengths. The system has an initial transient response at the beginning of compression, and the film thickness oscillates at first, it gets more stable as the system reaches a state of equilibrium. Fig. 2.5 also shows that, as the chain length increases, the system height at equilibrium is decreased. It should be noted that the total number of lubricant atoms is the same (15,600 atom) for all three cases. However, the number of lubricant chains varies due to the chain length. It leads to a different separation between the upper and lower walls.

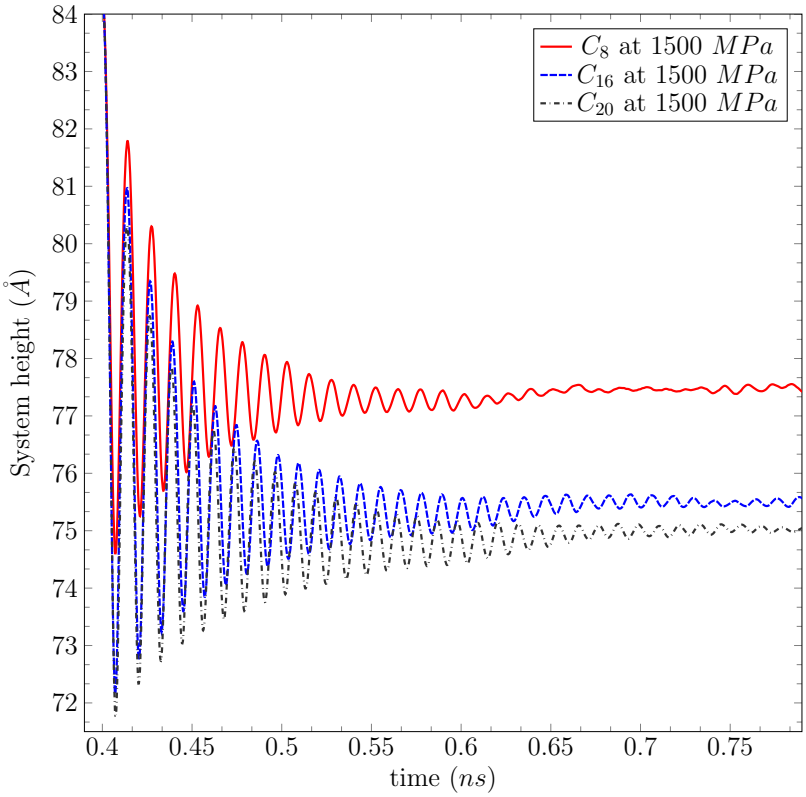

Fig. 2.5: Density profile of three different linear alkanes confined by surfaces.

The density profiles of C_8, C_{16}, and C_{20} full films are given in Fig. 2.6 which shows a clear layering structure. In all cases, the lubricant in the middle seems to remain in its bulk state. It suggests that the confining effect decays towards the inner layers.

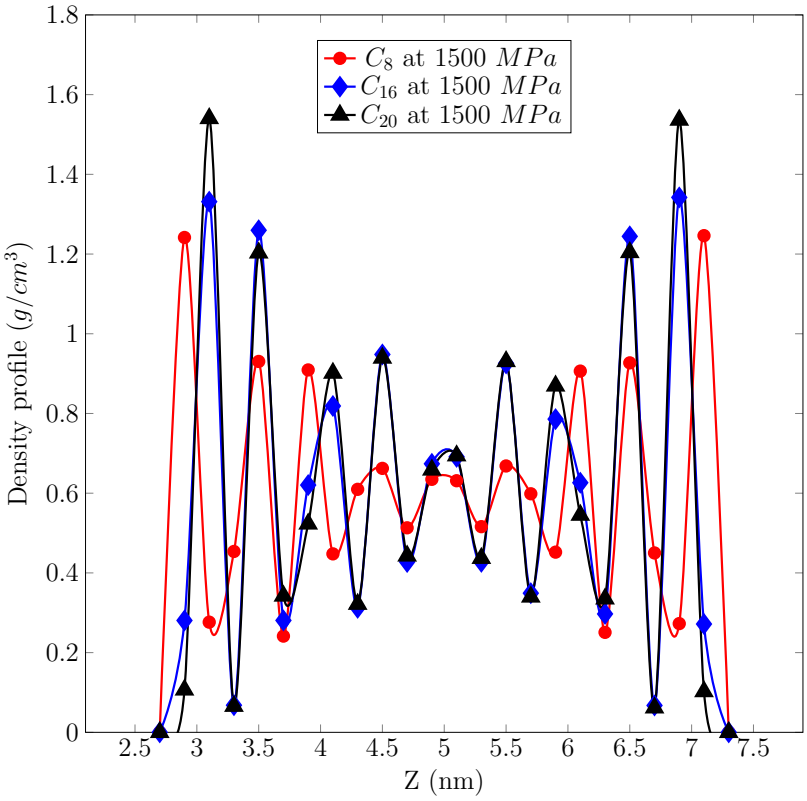

Fig. 2.6: Density profile of three different linear alkanes confined by surfaces.

In addition, from Fig. 2.6, an asymmetry in the density profiles is notices due to the normal motion only of the upper boundary layer while the lower boundary layer is fixed in the z direction. As it is mentioned before, the united atoms include CH_3

and CH_2 which have corresponding atom mass and the volume confined between the walls to calculate the average density. Fig. 2.6 also indicates that chain length has an effect on the layering structure, i.e., the lubricant with longer chains has sharper density peaks. This conclusion is in agreement with results of Koike and Yoneya [67]. Based on Fig. 2.6, the lubricant with shorter chains (i.e. C_8) has a larger film thickness. It is compatible with bulk density. However, the thickness changes are getting smaller as chain length increases. For example, the difference of film thickness between C_{16} lubricant and C_{20} lubricant is not significant and these two chain lengths maintain a clear layering structure even in the middle.

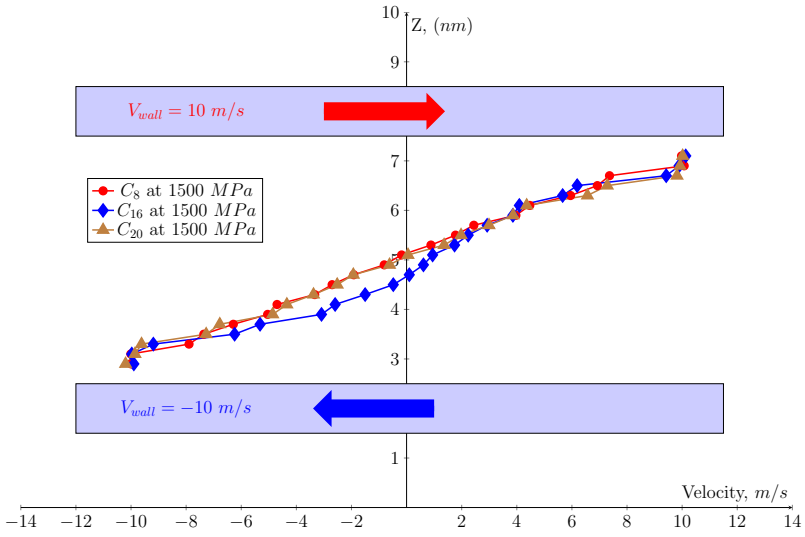

Fig. 2.7: Density profile of three different linear alkanes confined by surfaces.

In this section no-slip condition is considered for the simulation. It means that all the linear alkanes are confined by the wall with a strong liquid-solid interaction.

As Fig. 2.7 shows, all the lubricants have no slip at the boundary and there is no significant difference in their behaviors.

The shear stress is calculated by dividing the friction force over the surface area. The thickness of the lubricant is much larger than the cutoff distance for LJ interaction between the upper and lower atoms. Therefore, the shear stress is only obtained from the interaction between the upper wall and the lubricant. Theoretically, the shear stress of lubrication is determined by the property of the lubricant [67, 69, 70] and interfacial slip. Flow resistance increases by increasing the chain length because there is a strong cohesion between long chains (Table 2.3).

Table 2.3: Shear stress for different chain lengths

Chain length	Shear stress (MPa)
8	8.21
16	13.64
20	14.00

2.3.2 Coefficient of friction

In the MD simulations, the normal pressure is applied onto the upper wall atoms. The tribological phenomena of the system subject to different normal loads are investigated first. Fig. 2.8 indicates the variation in the system height, i.e. the film thickness, due to different normal loads. The system has a transient response at the beginning of compression, and the film thickness oscillates and tends to be stable

as the system reaches a state of equilibrium. As the normal load increases, the film thickness gets thinner. It can be seen that the film thickness gets stable after 0.6 ns.

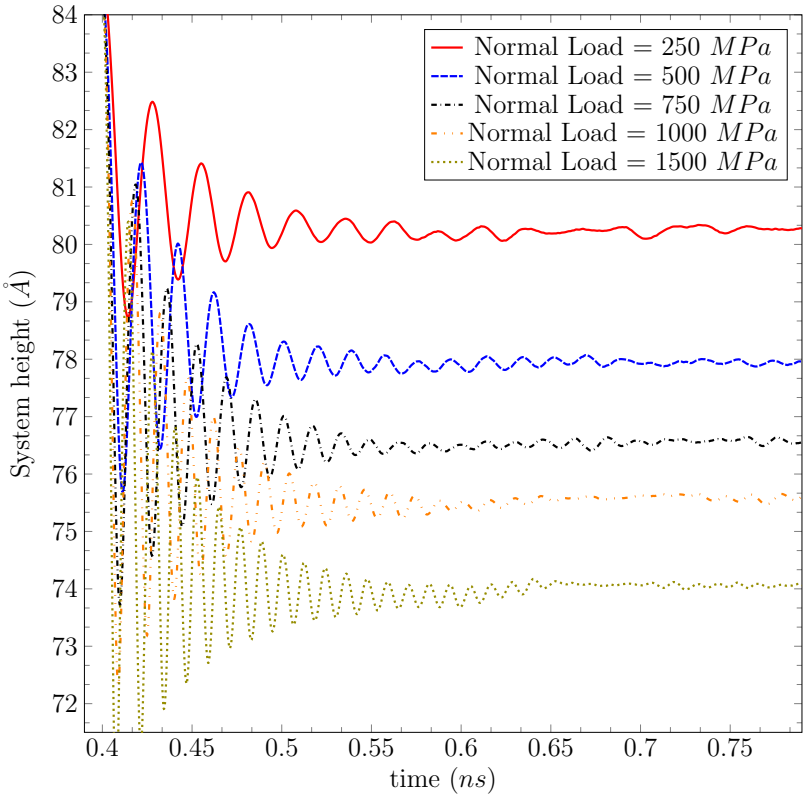

Fig. 2.8: System height, i.e. the film thickness, under various normal loads.

The film density profiles are shown in Fig. 2.9, which give a clear layering structure. The lubricant in the middle seems to remain in its bulk state. It suggests that the confining effect decays towards the inner layers. In addition, the density profile exhibits an asymmetry. This is due to the normal motion of the upper boundary layer while the lower boundary layer is fixed in the vertical direction. As it is

mentioned before, the united atoms include CH_3 and CH_2 which have corresponding atom mass and the volume confined between the walls to calculate the average density. Fig. 2.9 also shows that the density profile structure becomes larger near the walls and its thickness shrinks. It is predictable that the film thickness is smaller under a larger normal load, and the density profile has to be denser in some areas.

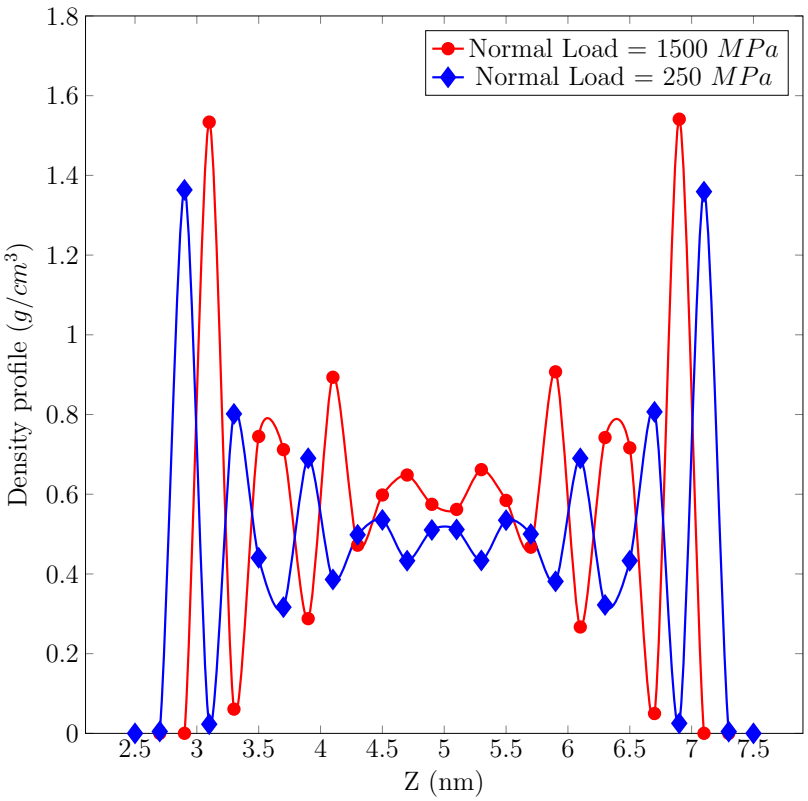

Fig. 2.9: Density profile of the linear alkane confined by surfaces.

The friction force under each normal load can be obtained in the MD simulation by summing the forces exerted on the atoms of the rigid and thermostat layers in

the longitudinal and vertical direction respectively. The friction forces under different normal loads are shown in the Fig. 2.10.

Generally, the friction coefficient can be calculated by

$$\mu = \frac{F}{P} \tag{2.19}$$

where F is the friction force and P is the externally applied load.

A linear function is used to fit the data in Fig. 2.10 to determine the coefficient of friction. The slope of the linear function indicates that the coefficient of friction equals to 0.0483. The calculated coefficient of friction is similar to the typical friction coefficients for many hydrodynamic lubricant applications. The friction coefficient calculated from the molecular model will then be passed to the fatigue life prediction model at the continuum level in next section.

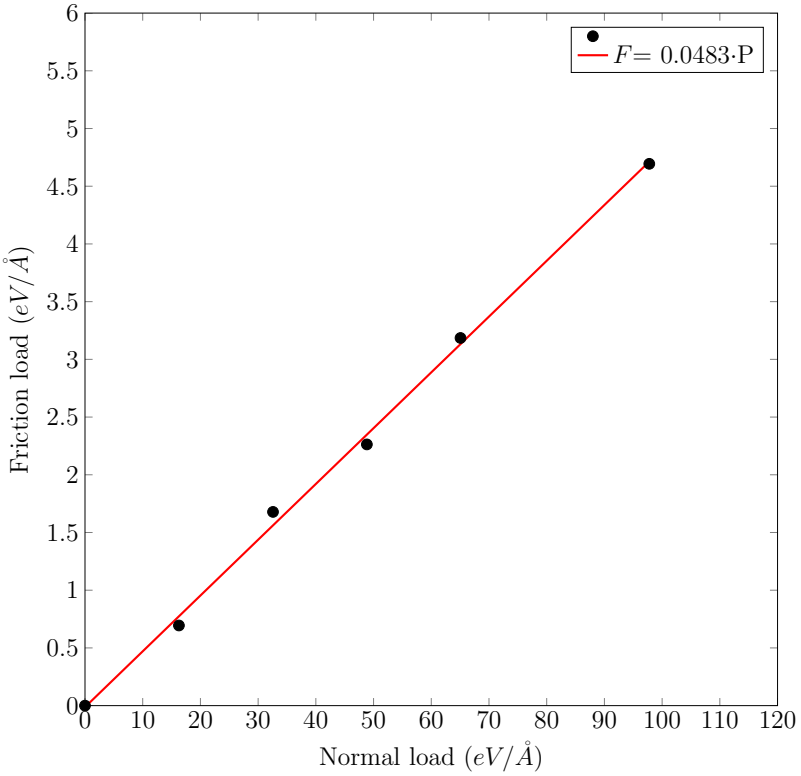

Fig. 2.10: Friction forces vs. normal loads.

2.3.3 Temperature effect

The effect of temperature on the friction force is studied here. The intention is to investigate the temperature dependency of the friction force in EHL bearings which will eventually become fatigue failure. In this section only the chain length of C_8 is considered for the lubricant film and 14,040 atoms are used for the lubrication molecules. As shown in Fig. 2.11, under a normal pressure of 250 MPa, when the temperature increases, the friction force decreases. It is because in very low temperatures (i.e. 100 K to 200 K), the lubricant acts as solid so that the friction between

the surface and the lubricant increases dramatically. However, as the temperature goes higher the friction force reduces smoothly. In reality, the normal operation of the bearings are typically at the temperature between 250 K to 500 K.

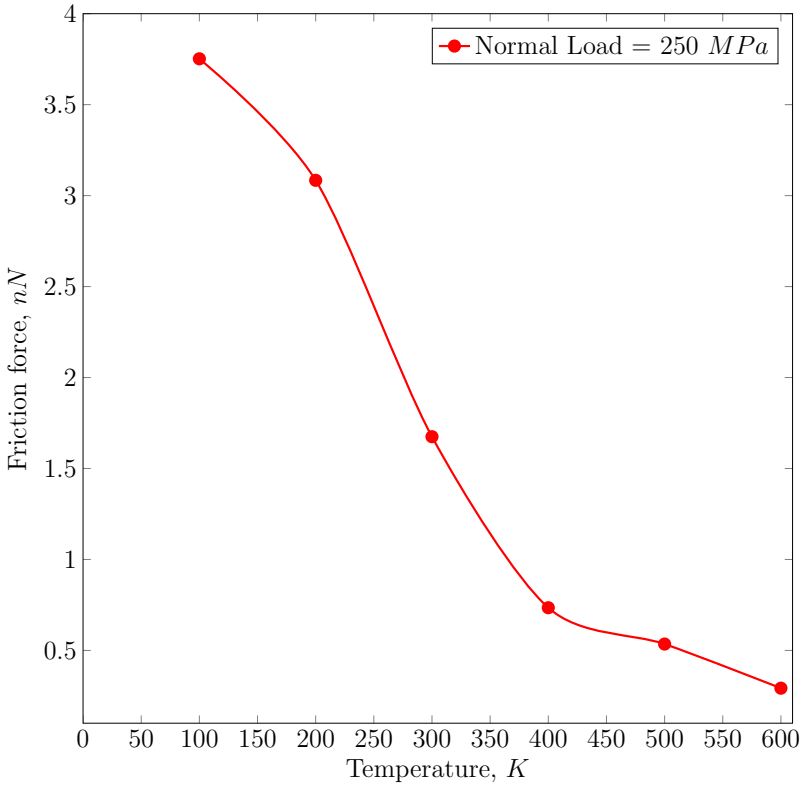

Fig. 2.11: Friction force versus temperature.

Velocity profiles of the lubricant film at different temperatures are shown in Fig. 2.12. It can be seen that at a lower temperature, the fluid velocity profile is more linear than the one at a higher temperature.

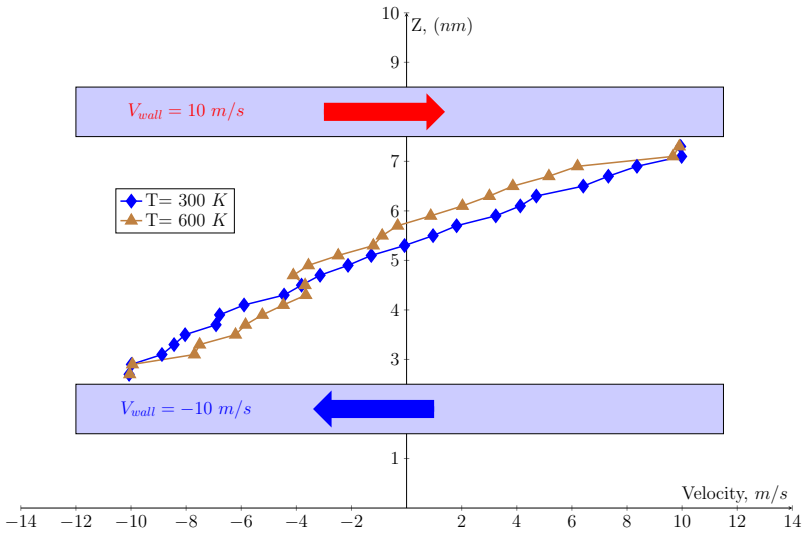

Fig. 2.12: Velocity profile of the lubrication confined between solid walls.

In addition, the temperature also has effect on the density profile of the lubricants depicted in Fig. 2.13. At a high temperature, the density profile of the lubrication film remains almost constant in the middle and it oscillates suddenly near the walls.

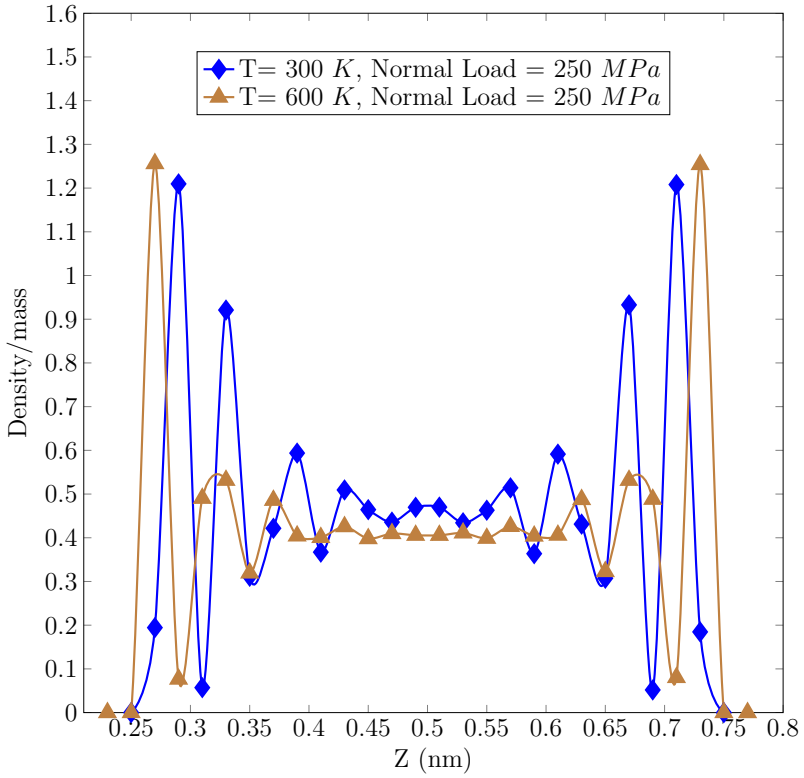

Fig. 2.13: Density profile versus lubrication height.

2.3.4 Effect of nano-particle (debris)

According to the studies done by Ghaednia et. al [46, 71] , nano particles in lubrication would reduce the friction force. First, in an elastohydrodynamic thin film lubrication, if the nano particle is smaller than lubrication thickness, the particle is not getting stuck between the walls. Consequently, the lubricants molecules move along with the nanoparticle between the contact surfaces. This would result in sliding (shearing) of only a few layers of lubricant molecules over one another [46]. On the other hand, when nano particles have contact with rough surfaces in a boundary

lubrication, the real contact area becomes smaller, and it will eventually reduces the friction force [71].

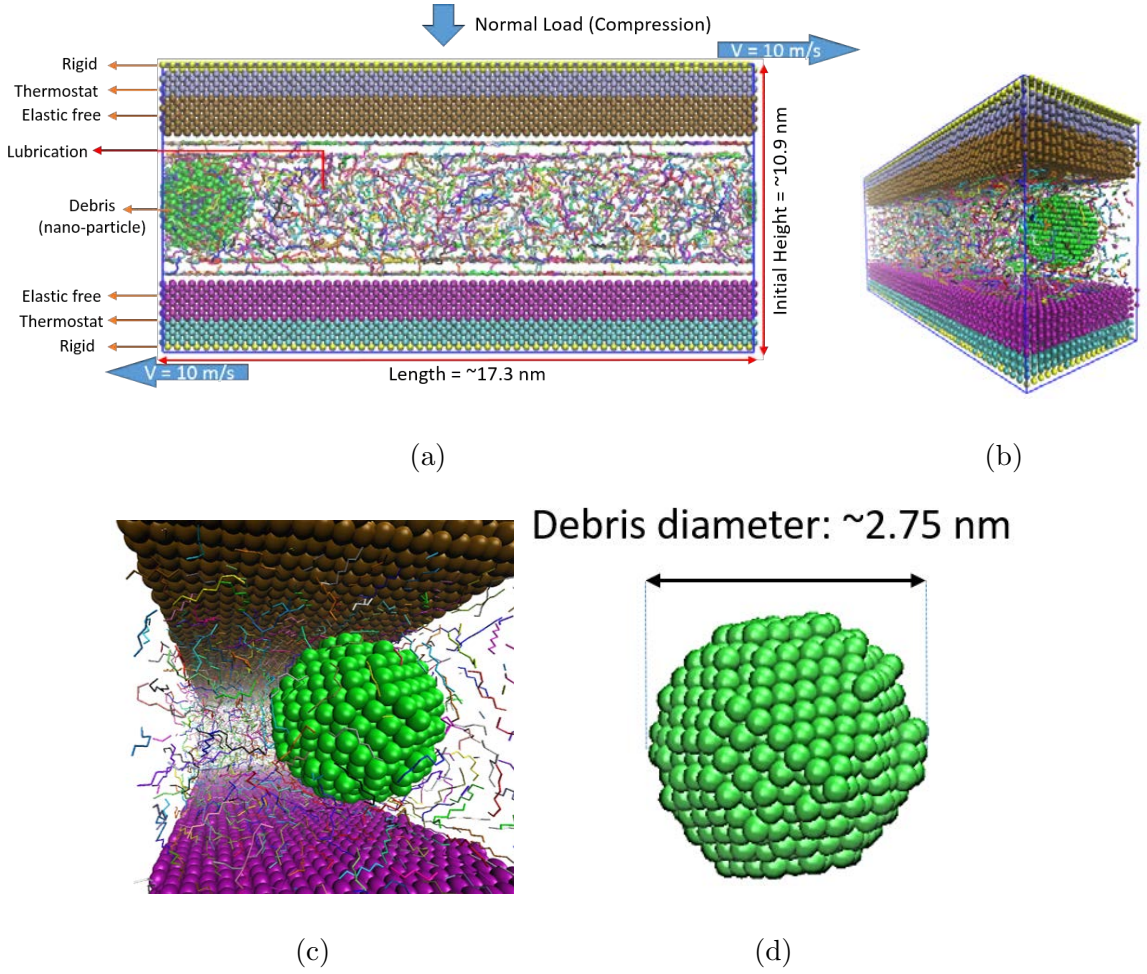

Fig. 2.14: Schematic view of thin film lubrication model in MD simulation in presence of nano-particle.

It should be noted that the regime of the lubrication will stay in hydrodynamic lubrication mode, and the effect of a nano-particle (debris) on the friction coefficient

will be studied. The nano particle is chosen large enough to get in contact with the two walls, and its material is the same as the wall material which is Fe (refer to Table 2.3). LJ potential function is used for the interaction forces between the nano particle and solid walls. The mixing rule is applied for the interaction of nano particle with the lubricant chains. . The schematic view of the model in the presence of the nano-particle is depicted in Fig. 2.14.

Different normal pressures are applied on the upper wall to calculate the friction force and then the coefficient of friction. Both cases with and without presence of the nano-particle are considered. The chain length of C_8 with 14,040 atoms is employed to model the lubricant film. The temperature is set at the room temperature of 300 K. Fig. 2.15 shows that friction force is increased with the presence of the nano-particle and consequently the coefficient of the friction is also increased by %40. Since the smooth surfaces in the simulation are considered, the effect on nano-particle on the coefficient of friction is not very high. It should be noted that the friction coefficient for the case without the nano particle is calculated different than the previous one in Section 2.3.2. This is due to the different thickness of lubricant films in two models.

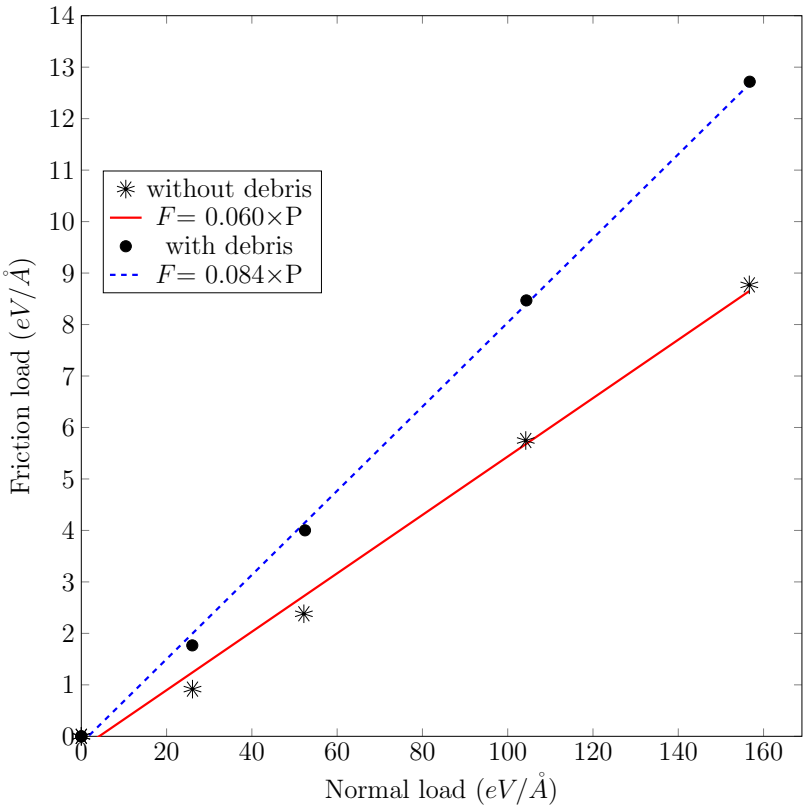

Fig. 2.15: Effect of nano-particle (debris) on the coefficient of friction.

2.4 Conclusions

In this chapter the basic principle of molecular dynamics simulation is presented. Specifically, the integration method determines how the position of each atom is updated while the thermostat method allows the heat, particularly for the frictional system, to be dissipated with the boundary condition. All this basic knowledge helps in understanding the specific models discussed in the following chapters. Because the force field is undoubtedly crucial to MD simulation, the choice of a proper force field depends on the physical properties of the problem. Due to severe deformation

and metal transfer, a specially-designed EAM potential is used on the wall molecules because it could handle the plastic deformation better than simple potentials such as LJ and Morse potentials. TraPPE-UA force field that covers the parameters for short chain PEO and linear and branched alkanes is used to model the lubricant. More importantly, the liquid-solid interaction not only affects the structure of confined lubricant, but also determines the interfacial slip.

In this chapter, molecular dynamic simulation of thin film lubrication was conducted. Solid walls were modeled by the Finnis-Sinclair (FS) EAM potentials and the united atoms includes CH_3 and CH_2 were considered for the fluid chain. The effect on a nano-particle (debris) and temperature on mechanical parameters of thin film lubrication in elastohydrodynamics regime was also studied. The material of the nano-particle was considered as the same as the wall material (Fe) and it was big enough to have contact with two solid surfaces. Based on the results in this chapter, in the presence of nano-particle the coefficient of friction in elastohydrodynamic regime will be increased by %40, and as the temperature increase the friction force is decreased with lead to less coefficient of friction.

It was also depicted that how increasing normal pressure will change the film thickness, when chain length of 8 is considered for the fluid. Furthermore, based on the relation of friction force and normal load, coefficient of friction for the thin film fluid were obtained to use in macro-scale in order to calculate roller contact fatigue.

CHAPTER 3
BEARING FAILURE (MACRO SCALE)

3.1 Continuum modeling of rolling contact fatigue

In this chapter, the fatigue life at crack initiation is predicted via the continuum mechanics approach. The contact pair, e.g. bearing, in the rolling contact model includes the rolling element and the bearing inner race. The rolling element is modeled as a rigid body while the material of bearing inner race is assumed to be homogeneous and isotropic. In addition, the bearing is assumed to be free of imperfections. Since the curvature of the bearing inner race is much smaller than the one of the rolling element, the bearing inner race is considered having flat surface in our model. The stress analysis of the rolling contact model is conducted in the FEM framework through ANSYS parametric language for moving Hertzian contact load [72], as shown in Fig. 3.1. Two-dimensional model is used here, and the simulation includes two steps. Firstly, the normal load is applied to achieve the contact between the roller and the surface. Then, the roller moves in X-direction while the contact load is applied. It shall be noted that the prescribed friction coefficient of 0.0483 was obtained via MD modeling and simulation discussed in previous section. During the simulation, the stress state at each node is calculated per step of the moving Hertzian contact loading. Then, the stress history, i.e. the stress loading cycle, for each node in one Hertzian contact loading cycle is obtained. The stress loading cycle is calculated using the critical plane damage method [72] based upon the analysis of stresses or

strains as they experienced at a particular plane of the material.

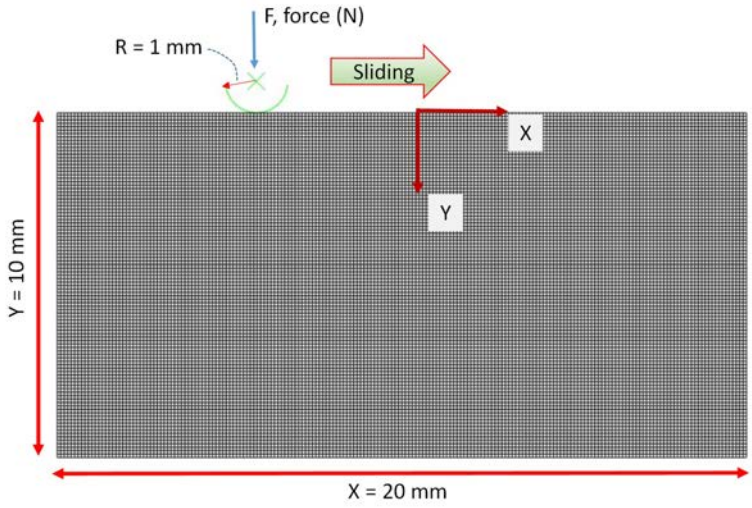

Fig. 3.1: Schematic Finite element model and cyclic Hertzian contact load through analytical rigid body on the surface.

Calculating the stress loading cycle at the critical plane is essential for analyzing the rolling contact fatigue life because the critical plane is experienced the most extreme damage and is most likely for the fatigue crack to initiate [73]. The emergence of different fracture modes generally depends on the material type, strain amplitude and state of stresses. If the tensile stress is the dominant stress in the material, the following tensile-based damage model will be used to predict the fatigue life [73]:

$$d_t = \sigma_{max}\epsilon_a = \frac{(\sigma'_f)^2}{E}(2N_i)^{2b_i} + \sigma'_f\epsilon'_f(2N_i)^{b_i+c_i} \tag{3.1}$$

where d_t is the tensile damage parameter, σ'_f and ϵ'_f are the maximum principal stress calculated from three-dimensional simulation and the largest normal strain amplitude for any plane, respectively. σ_{max} is the fatigue strength coefficient, ϵ_a is the axial fatigue ductility coefficients, b_i and c_i are the axial fatigue strength exponent and the ductility exponent respectively, and N_i is the fatigue crack initiation life, i.e. the number of loading cycles for crack initiation.

The tensile damage parameter for the plane strain and plane stress conditions can be obtained by stress and strain analysis:

$$d_t = \sigma_{max}\epsilon_a = \begin{cases} \frac{1-\upsilon^2}{2E}\sigma_n^2 & Plain\,Strain \\ \\ \frac{\sigma_n^2}{2E} & Plain\,Stress \end{cases} \tag{3.2}$$

where υ is Poisson ratio, and σ_n is the normal stress. The normal stress was corrected by Hoffman-Seeger [74] after updating by the finite element method. Substituting Eq. 3.2 into 3.1, the fatigue crack initiation life N_i can be determined.

If the shear stress is the dominant stress in the material, the following shear-based damage model will be used to predict the fatigue crack initiation life of the material [73]:

$$d_s = \gamma_a\left(1 + k\frac{\sigma_{max}}{\sigma_{ys}}\right) = \frac{\tau'_f}{S}(2N_i)^{b_{0i}} + \gamma'_f(2N_i)^{c_{0i}} \tag{3.3}$$

where d_s is shear damage parameter, γ_a is the largest shear strain amplitude for any plane, S was the shear modulus, and τ'_f is shear fatigue strength coefficient. Yield

stress and maximum normal stress on the same plane as largest normal strain amplitude are demonstrated by σ_{ys} and σ_{max} respectively. Material parameters such as b_{0i}, c_{0i} and k are also considered in the equation. The shear damage parameter is calculated for both the plane strain and plane stress conditions as follow:

$$d_s = \gamma_a \left(1 + k\frac{\sigma_{max}}{\sigma_{ys}}\right) = \frac{1+\upsilon}{2E}\sigma_n \left(1 + k\frac{\sigma_n}{\sigma_{ys}}\right) \tag{3.4}$$

3.2 Results and discussions

A quasi-static simulation is conducted to model moving Hertzian contact [72]. C-Mn Steel SAE1561 is used as the material of the bearing inner race. The material properties are shown in Table 3.1. The fatigue related parameters are obtained from the E-N fatigue data of this material shown in Fig. 3.2.

Table 3.1: Material properties [1]

Description	Symbol	
Yield strength (MPa)	Y	447
Ultimate tensile strength (MPa)	U	836
Elastic Modulus (MPa)	E	2.07×10^5
Fatigue strength coeff. (MPa)	σ_{max}	1278
Fatigue Strength exponent	b_i	-0.11
Fatigue ductility exponent	c_i	-0.54
Fatigue ductility coeff.	ε_a	0.53
Cyclic strain hardening exponent	n'	0.19
Cyclic strength coeff.	K'	1448

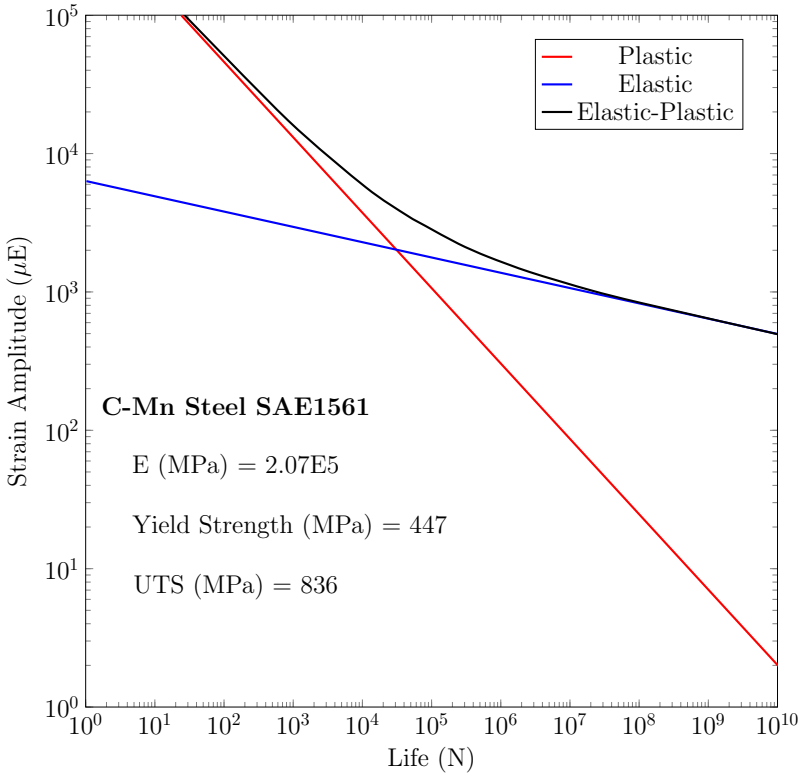

Fig. 3.2: Strain-life data for C-Mn Steel SAE1561.

Based on the above material fatigue data and the E-N fatigue calculation approach, fatigue life cycles for the different load cases are analyzed via Eq. 3.1, and the results are shown in Fig. 3.3. For the Hertzian load lower than 3000 MPa, there is no fatigue observed. In other words, fatigue only occurs under the loads equal to and larger than 3000 MPa. It is also shown in Fig. 3.3 that the fatigue life decreases as the normal load increases and the behavior is almost logarithmic.

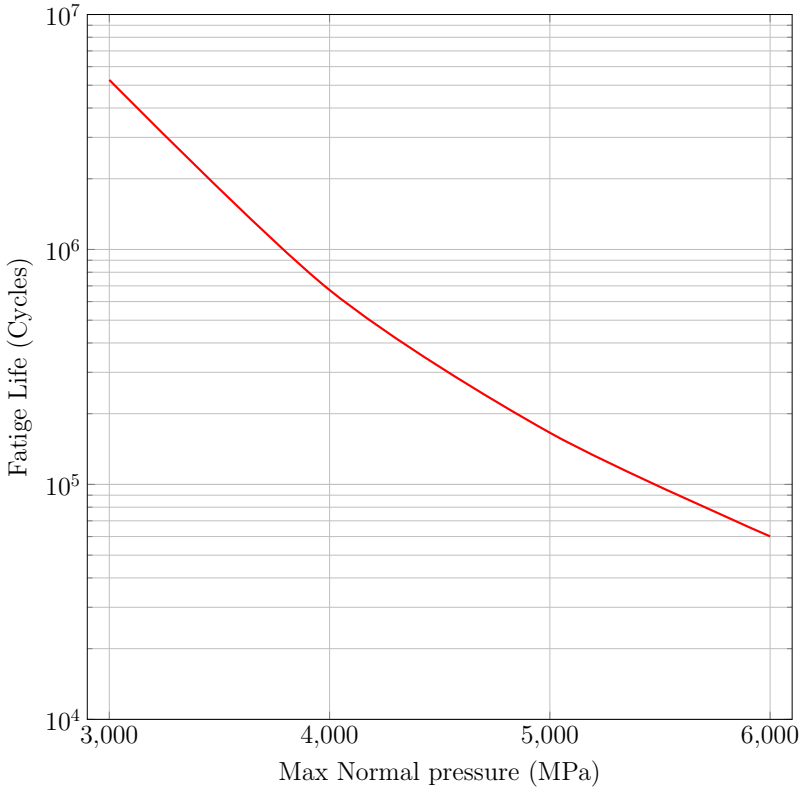

Fig. 3.3: Fatigue life versus different Hertzian normal pressures.

In the continuum model, the stress histories at various points during one contact loading cycle are calculated first. Then, the fatigue lives are evaluated at those points to find the critical location where fatigue occurs. Since the stress is only various along the vertical direction in the two-dimensional model, the locations at x=0 are considered to calculate the stress histories. One point on the contact surface and other six points under the surface are chosen. The distances between those points and the contact surface are 0.000 mm, 0.027 mm, 0.055 mm, 0.083 mm, 0.111 mm, 0139 mm, and 0.167 mm. The shear and Von-Mises stress profiles at those seven

points during one contact loading cycle are shown in Fig. 3.4. It shall be noted that the stress profiles under various contact loads are pretty similar and only the stress magnitudes are different. Therefore, a single load case of Hertzian contact load with $P_{max} = 6000$ MPa is consider first. Fig. 3.4 shows that as it goes deeper from the contact surface the shear stress increases until to the point at $y = -0.139$ mm and then decreases. However, the Von-Mises stress keeps decreasing.

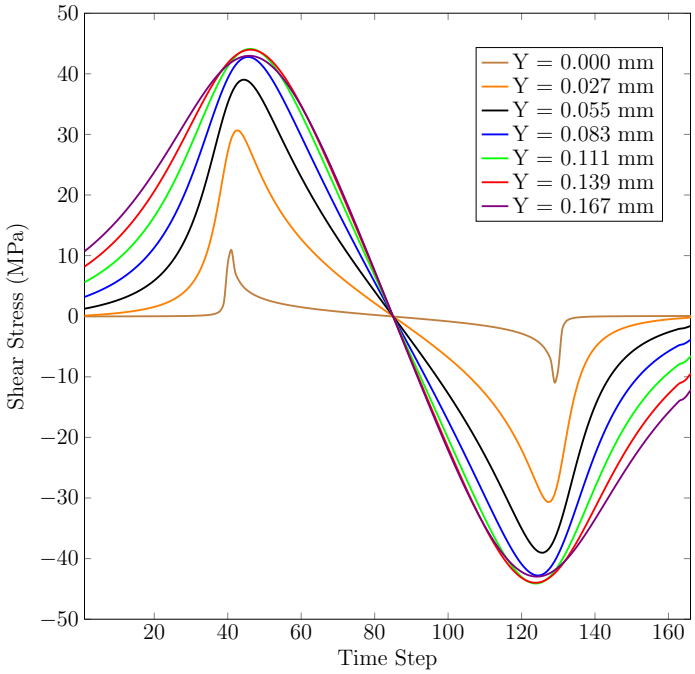

(a)

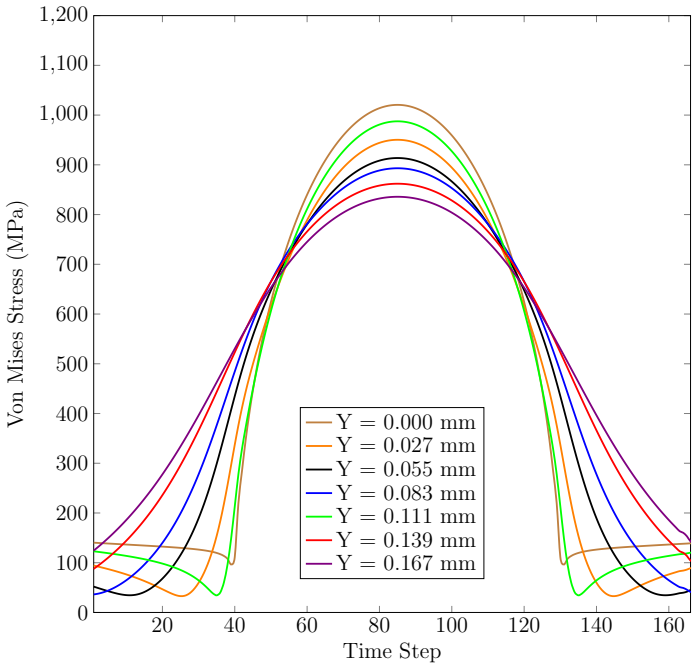

(b)

Fig. 3.4: Stress histories under the contact surface when Hertzian contact load of $P_{max} = 6000$ MPa; (a) Shear stress; (b) Von-Mises stress.

Using the relationship between the deformation and the number of loading cycles for the fatigue crack initiation, i.e. Eq. 3.1, the position of initial fatigue fracture and the corresponding number of stress cycles can be determined, as shown in Fig. 3.5. The number of loading cycles required for initial fatigue crack occurring is 6.01E4 cycles. In addition, the initial fatigue crack occurs at $y = 0.08$ mm under the contact surface.

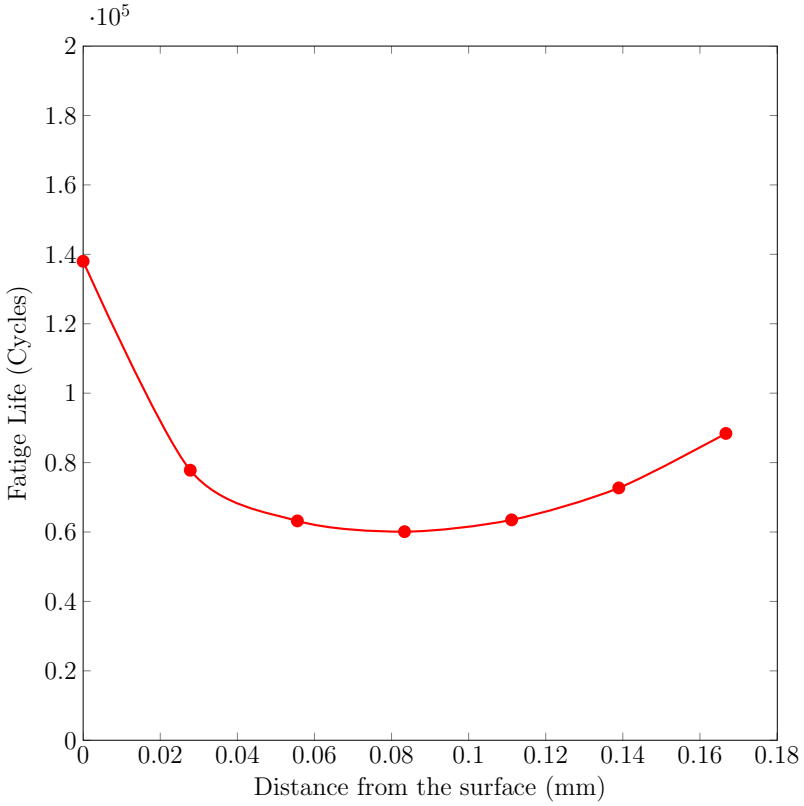

Fig. 3.5: The number of loading cycles till the initial crack occurs at the observed material points when $P_{max} = 6000$ MPa.

Various normal loads are also considered here as 3000 MPa, 4000 MPa and 5000 MPa. The fatigue lives at the points below the contact surface are shown in Fig. 3.6. It indicates that the fatigue life scatters are almost the same at all the loads, and the difference is only in its value. The locations of the initial crack are the same under all the normal loads. Fig. 3.6 also demonstrates that as the normal load increases the fatigue life decreases and the crack initiation occurs after 5.2×10^6, 6.7×10^5, and 1.6×10^5 cycles when the normal loads are 3000 MPa, 4000 MPa and 5000 MPa, respectively. It shall be noted that the crack initiates below the surface and it will start to propagate in different angles and then to reach the surface eventually. This phenomenon is so-called spallation.

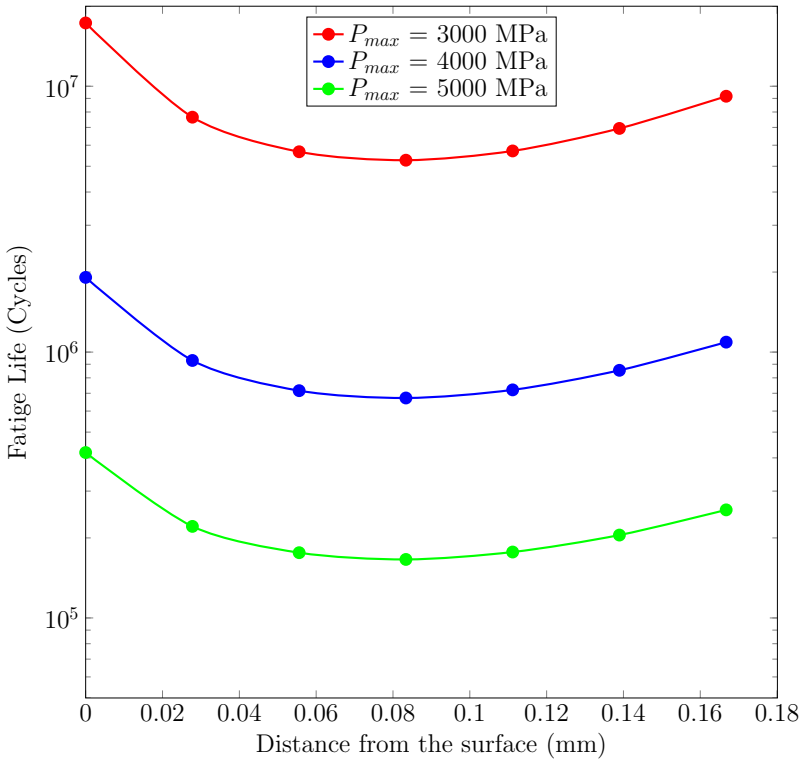

Fig. 3.6: Number of loading cycles till the initial crack occurs at the observed material points when $P_{max} = 3000$ MPa, $P_{max} = 4000$ MPa, and $P_{max} = 5000$ MPa.

In the application of wind turbine, the wind turbine blades rotate due to wind's forces, including two primary aerodynamic forces: lift and drag. Mostly, the wind flow is not steady so that the wind turbine blades exhibit vibrations during rotation. Consequently, the torque and the bending moment transferred to the wind turbine gearbox through the speed shaft has some fluctuations, i.e. noises, as well as the resulted normal load on the bearings in the gearbox. Therefore, it is crucial to consider the load fluctuation when predicting bearing fatigue life in wind turbine gear box. To study rolling contact fatigue life under fluctuating loads, the continuum model, de-

scribed in the above, is implemented in the software of nCode Designlife. The nCode Designlife utilizes the frequency domain fatigue analysis in which the random loading and response are categorized using Power spectral density (PSD) functions [75].

Three fluctuating normal loads, shown in Fig. 3.7, due to random vibrations are considered here to calculate rolling contact fatigue lives. Although those three fluctuating loads have the same mean value of 3000 MPa, they have different amplitudes. The minimum and maximum loads of those three fluctuating loads are [0.7, 1.3], [0.8, 1.2] and [0.9, 1.1] of the mean load which is represented as the dot line in Fig. 3.7. The prescribed friction with the friction coefficient of 0.0483 is applied here. It shall be noted that the friction coefficient under fluctuating loads can be calculated via the same molecular model as described in chapter 2.

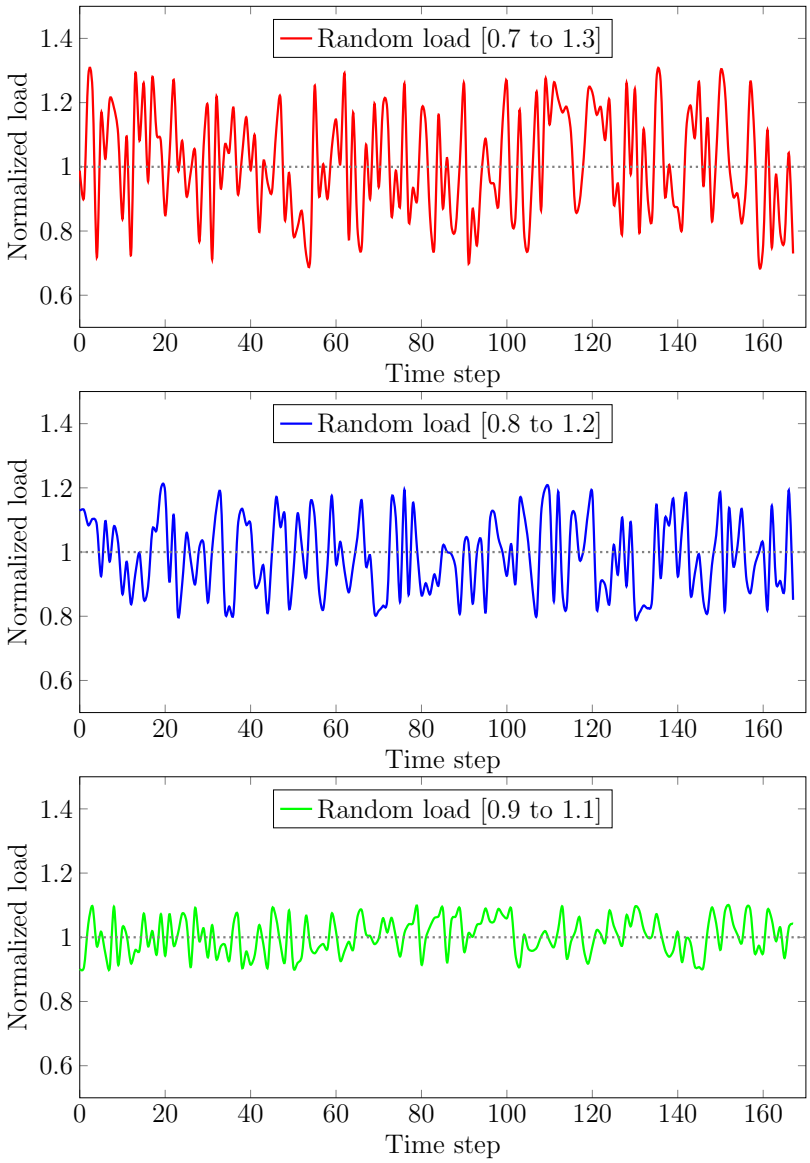

Fig. 3.7: Three different normalized fluctuating normal loads during one Hertizan contact cycle.

The time histories of Von-Mises stress at a node on the contact surface is shown in Fig. 3.8. It shows that for the fluctuating load with larger amplitude, the resulted Von-Mises stress has larger fluctuation. It shall be noted that the difference

of noise levels between various random loads is significant, especially the noise peaks.

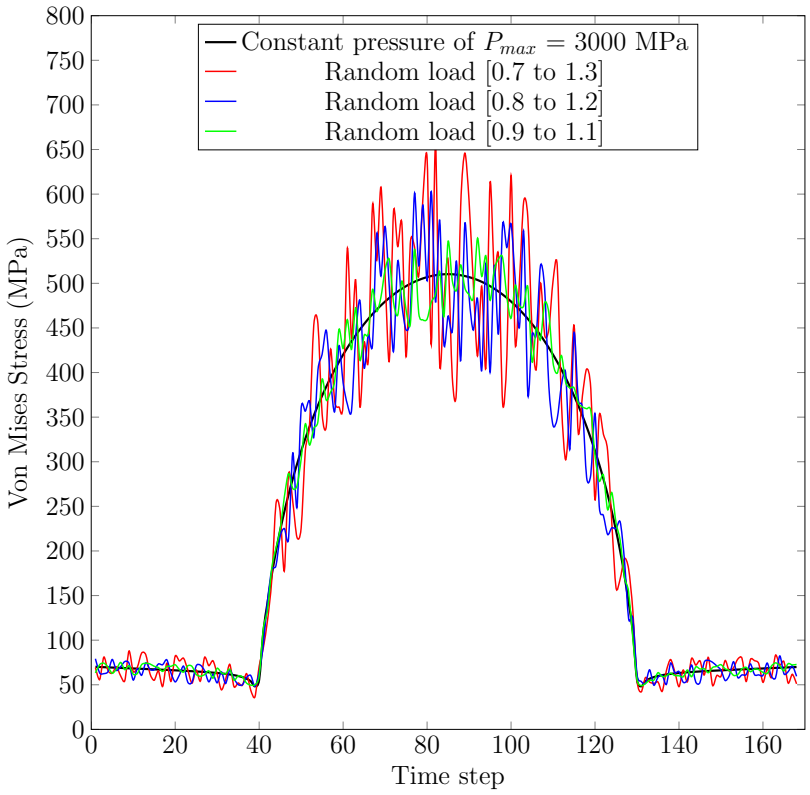

Fig. 3.8: Von-Mises time history for different random loads at a node on the contact surface.

The predicted rolling contact fatigue lives under various fluctuating normal loads are shown in Table 3.2, compared with the result due to a constant normal load of 3000MPa. As shown in this table, the fatigue life for the case under a constant normal load is much higher than the others. This demonstrates that if the system was subject to a fluctuating cyclic load, the fatigue life would be dramatically reduced.

In addition, as the amplitude of the fluctuating load becomes smaller, the fatigue life increases.

Table 3.2: Rolling contact fatigue lives under a constant load of $P_{max} = 3000$ MPa and various fluctuating loads with the mean value of 3000 MPa

Case study	Fatigue life
Constant pressure of P_{max}	5.2×10^6
Random load [0.9, 1.1]	2.4×10^6
Random load [0.8, 1.2]	1.3×10^6
Random load [0.7, 1.3]	0.8×10^6

3.3 Conclusion

In this chapter, the continuum model is developed and employed to study rolling contact fatigue and predict fatigue life. Since the thickness of the lubricant is very small, molecular model is a proper method to simulate the lubricant so that the friction phenomena can be studied between two contact surfaces. The calculated friction coefficient, in the previous chapter, is passed to the continuum model of the rolling contact component in the proposed multiscale modeling framework. The fluctuating load is also considered, and the fatigue life is significantly reduced. The proposed multiscale method belongs to the family of hierarchical or sequential multiscale methods due to its one-way message passing from the molecular model to the continuum model.

CHAPTER 4
GEAR-TOOTH FATIGUE FAILURE (MACRO SCALE)

4.1 Introduction

There are many types of gear teeth subject to cyclic loading in different industries including: wind turbines, gas and oil transmissions, and power plants. The modern industrial gears usually fail due to material fatigue under repeated loading that is manifested in the surface pitting of the gear tooth flank. These components need to be capable to withstand fatigue damages in their lives. Fully understanding the gear tooth failure mechanism can help to design more reliable gears. Numerical methods are powerful tools used to study this complicated physical phenomena. Most researches in studying crack initiation and propagation of an industrial gear tooth were done using two-dimensional finite element numerical modeling methods and simulation.

One of the common failures in gears made of alloy steel, with smooth contact surfaces and appropriate lubrication, is the subsurface pitting initiation. Shear subsurface stresses due to contact loading cause a substantial dislocation motion, which can initiate fatigue cracking [73, 76]. Sraml et. al [76] developed a general computational model for the simulation of contact fatigue crack initiation in the gear tooth. They used damage mechanics to model fatigue crack initiation in a two-dimensional model. However, in these previous studies, moving contact loads along the tooth surface had not been considered. Once the crack is initiated the gear tooth crack propagation

life must be considered [77–85]. Podrug et. al [73] presented a computational model for finding fatigue lives of gears under moving bending loads. They modeled two-dimensional crack propagation and also studied the effects of a moving load on the fatigue life of a gear. Glodez et al. [77] presented a new model to determine the pitting resistance of the gear tooth flank. The number of cycles required for crack propagation from the initial crack length to the critical crack length was obtained in their research. They applied this model on a real spur gear pair that was also experimentally tested. After this work, Glodez et al. [78, 79] continued to develop a general computational model for simulating fatigue crack growth of mechanical elements under cyclic contact loading. For different combinations of contact surface curvatures and contact loadings, the effects of various crack length on the pit shapes and the first stress intensity factor were studied. In industrial gears that have rough surfaces, the surface pitting is mainly influenced by the surface roughness. It results in residual stresses and fatigue which lead to surface cracking. Other defects including; debris, machining defects, large notches and inclusions are also responsible for some of the surface pitting initiation.

Most of the studies about gear tooth fatigue failure have used computational fracture mechanics and employed two-dimensional models [80–84]. Lewicki et al. [80, 81] conducted analytical and experimental studies to investigate the effect of rim thickness on gear tooth crack propagation. They used FRANC (FRacture ANalysis Code) program to simulate gear tooth crack propagation. Another study presented by Albrecht [82] devised a system which included gear tooth stresses, gear resonance and trans-

mission noise using NASTRAN. Fatigue crack propagation in specimens similar to the gear teeth were studied by Blarasin et al. [83]. They predicted crack propagation in different models of the cracked specimens using two numerical approaches: the finite element method and the weight function technique. Flasker et al. [84] calculated crack propagating speed in the tooth root of a case-hardening and hardened gear using linear elastic fracture mechanics.

In addition, Spievak et. al [86] studied fatigue failure in spiral bevel gears under bending loads using the boundary element method. They developed a method to predict two-dimensional fatigue crack growth in a three-dimensional specimen geometry. Besides the numerical studies, some experimental investigations on fatigue mechanisms of gears have been conducted by Pehan et al. [6] and Blarasin et al. [83]. In addition, many researchers have discussed the effect of contact pressures on the fatigue crack growth in a gear tooth [6, 83, 87, 88].

There were only a few examples of three-dimensional crack growth investigations on gears presented so far [84, 85]. Pehan et. al [85] modeled the gear three-dimensionally and the propagation of each point along the crack tip profile was considered to be in the direction of the maximum strain energy release rate. However, the crack depth was calculated in such a way that the stress intensity factor on the crack tip profile was constant. The result of the numerical calculations of their study gave a diagram of the stress intensity factor as a function of crack depth. Lewicki et. al [89] performed a three-dimensional crack growth simulation on a split-tooth gear design using boundary element modeling and linear elastic fracture mechanics.

Preventing a catastrophic failure and extending fatigue life of a cracked gear tooth becomes possible when using a proper technique to repair it. Reinforcing and repairing components with composite patches is a well-known technique in civil and aerospace engineering applications [4, 7]. However, there were not any previous studies considering composite patches to repair a gear tooth for extending the fatigue life.

A three-dimensional (3D) mixed-mode fatigue crack model must be considered in order to develop a more comprehensive crack growth model. In this chapter, crack initiation was studied first to investigate the location where the failure started. Various friction coefficients on the gear tooth surface were considered. Then, the crack propagation in the gear tooth was studied via the three-dimensional finite element model developed in this chapter. The effects of various load conditions on the crack trajectories and the fatigue crack propagation life were investigated. Fatigue crack composite repair was also implemented to determine its effectiveness impeding crack propagation. All implementations in this study are carried out by computational methods.

The outline of this chapter is as follows. In section 4.2, a comprehensive three-dimensional model for studying crack initiation and propagation in a gear tooth is developed. Methodologies for calculating fatigue crack initiation and propagation lives are also introduced. Section 4.3 describes the calculation of crack initiation life. In section 4.4 the following results from crack propagation simulations are discussed: fatigue crack propagation life, variation of stress intensity factors through the face width, crack trajectory, crack front shape and 3D crack surface after crack propaga-

tion. Section 4.5 explains the extension of fatigue crack propagation life of a gear tooth by using composite patches and the conclusions are given in Section 4.6.

4.2 Modeling and methodologies

4.2.1 Geometry of the gear tooth and the load condition

In this chapter, the numerical model of a cylindrical gear tooth with straight teeth in a gear has the following geometrical data from previous study of Podrug et.al. [73]. The number of teeth is $z = 39$, normal module is $m = 4.5$ mm, center distance is $a_{cent} = 91.5\,mm$, addendum modification coefficients is $x = 0.06$, tooth face width is $b = 28\,mm$, and an engagement angle on the pitch diameter is $\alpha_n = 24^o$. It is noted that in this work, the gear tooth geometry for all the case studies is constant and it is illustrated in Fig. 4.1(a). The gear is made of high strength alloy steel 14NiCrMo 13-4 with Youngs modulus $E = 2.1E5\ MPa$ and Poisson's ratio $\upsilon = 0.3$. The full contact width along the face width (Z direction) was $28\,mm$, the Hertzian contact load width was $2.39\,mm$ and the sample pressure P_0 was $1550\ MPa$ [73, 76].

Fig. 4.1 and Fig. 4.2 illustrate the developed three-dimensional models of a gear tooth for studying fatigue crack initiation and fatigue crack propagation respectively. A type of isotropic 8-node-solid elements (SOLID45) was used. To analyze fatigue crack initiation, fine meshes were generated at the surface of the tooth root as shown in Fig. 4.1(b). When studying the fatigue crack propagation, fine meshes were generated only around the crack at every step as shown in Fig. 4.2(a) for the gear tooth with

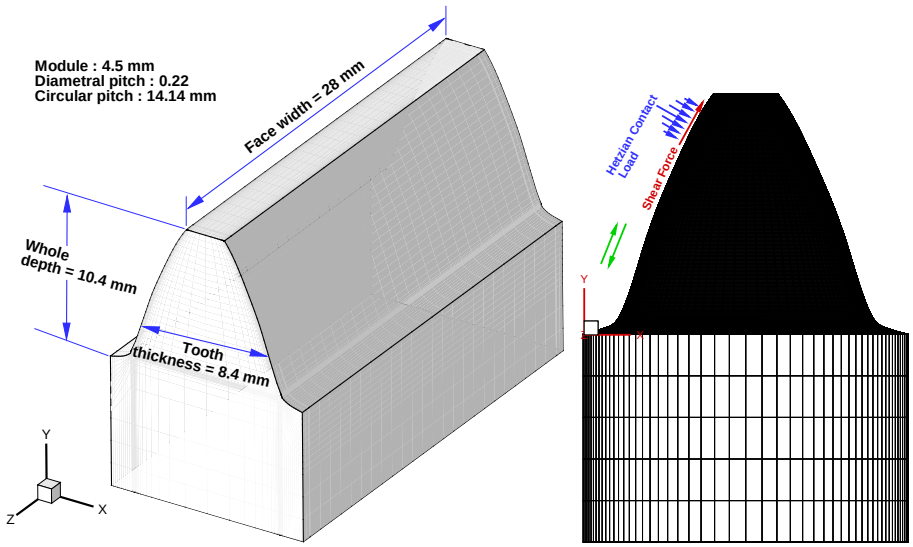

(a) (b)

Fig. 4.1: (a) Geometry of the gear tooth used in this study, (b) Typical finite element mesh for an undamaged gear tooth.

an initial crack.

A small de-bonded area equal to the element size at the crack edges has been considered in the finite element model. This is necessary for numerical modeling and it is almost compatible with experimental evidence [7]. The stress and strain fields of the cracked gear tooth were obtained using the elastic solution from the ANSYS finite element program.

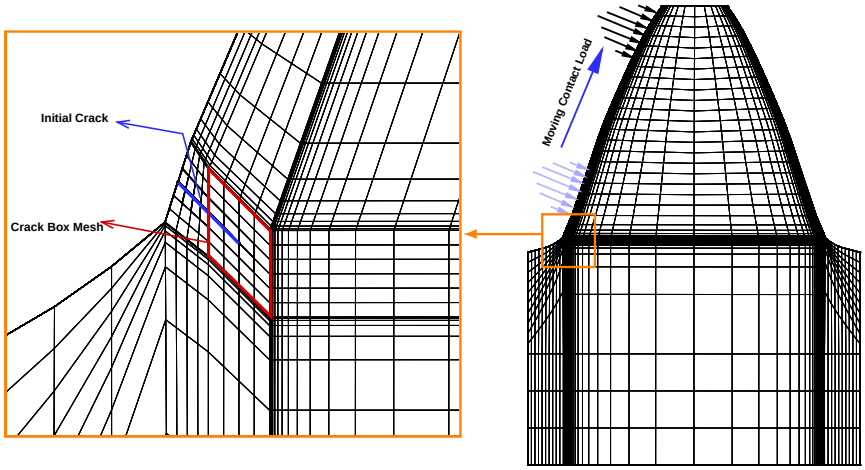

(a)

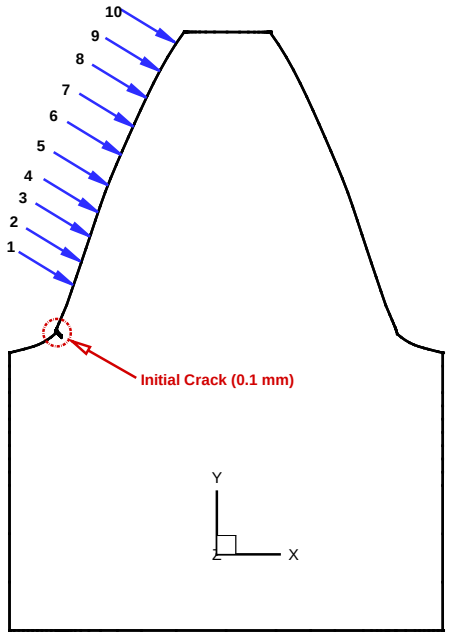

(b)

Fig. 4.2: (a) Typical FEM mesh of a cracked gear tooth, (b) Moving contact load model.

4.2.2 Modeling of fatigue crack initiation

Two concerns arise when calculating the service life of a mechanical system. At first, individual elements and the entire product during designing are optimized particularly with respect to the service life. In this case, modeling the occurrence of defects (crack initiation) and the crack propagation are important [76] to accurately predict the service life. Secondly, a defect such as a crack is detected during periodic inspection. If an extra component for the one concerned is not available or a considerable amount of time would be necessary to manufacture it, the following questions will arise: how long will the damaged component operate with full rated loading and/or what will the loading for the desired service life be, i.e. the time necessary for the manufacture of a new component-gear.

Using continuum mechanics approach and assuming a homogeneous and isotropic material, fatigue crack initiation can be simulated. The gear tooth is assumed having no imperfections and damages. In this study, the stress analysis of the contact model was executed in the framework of the finite element method using ANSYS parametric language for moving Hertzian contact load as shown in Fig. 4.2(b). The stress state at each node was calculated per step of the moving Hertzian contact loading. Then, a real stress loading cycle for each node in one cycle of the moving contact load was obtained. Calculating the stress loading cycle was essential for the contact fatigue life analysis. The stress loading cycle was calculated using the critical plane damage method based upon the analysis of stresses or strains as they were experienced by a particular plane in a material. This plane, called the critical plane, experienced the

most extreme damage, and fatigue crack initiation would likely occur in this plane [73].

Shear and tensile cracks generally occur in a material depending on material type, strain amplitude and state of stresses. If the tensile stress was the dominant stress in the material, the following tensile-based damage model might be used for predicting the fatigue life of the material [73]:

$$d_t = \sigma_{max}\epsilon_a = \frac{(\sigma'_f)^2}{E}(2N_i)^{2b_i} + \sigma'_f\epsilon'_f(2N_i)^{b_i+c_i} \tag{4.1}$$

where d_t is the tensile damage parameter, σ'_f is the fatigue strength coefficient, ϵ'_f is the axial fatigue ductility coefficient, b_i and c_i are used for the axial fatigue strength exponent and the ductility exponent respectively. σ_{max} and ϵ_a are the maximum principal stress calculated from three dimensional simulation and the largest normal strain amplitude for any plane respectively. In this chapter, the following parameters determined in experiments [73] are used: $\sigma'_f = 1464MPa$, $\epsilon'_f = 0.3$, $b_i = -0.08$ and $c_i = -0.51$. N_i was the fatigue crack initiation life, i.e. the number of loading cycles for crack initiation. Using stress and strain analysis in the gear tooth, the tensile damage parameter for the plane strain and plane stress conditions can be performed:

$$d_t = \sigma_{max}\epsilon_a = \begin{cases} \frac{1-\upsilon^2}{2E}\sigma_n^2 & Plain\,Strain \\ \\ \frac{\sigma_n^2}{2E} & Plain\,Stress \end{cases} \tag{4.2}$$

where Poisson ratio, υ, is equal to 0.3 and σ_n is the normal stress at the plane normal to the surface at the gear root. The normal stress was corrected by Hoffman-Seeger [74] after calculating by finite element method. Substituting Eq. 4.2 into 4.1, the fatigue crack initiation life, N_i can be determined.

If the shear stress was the dominant stress in the material, the following shear-based damage model would be used for predicting the fatigue crack initiation life of the material [73]:

$$d_s = \gamma_a \left(1 + k\frac{\sigma_{max}}{\sigma_{ys}}\right) = \frac{\tau_f'}{S}(2N_i)^{b_{0i}} + \gamma_f'(2N_i)^{c_{0i}} \tag{4.3}$$

where d_s is shear damage parameter, γ_a is the largest shear strain amplitude for any plane, S was the shear modulus, and τ_f' is shear fatigue strength coefficient. Yield stress and maximum normal stress on the same plane as largest normal strain amplitude are demonstrated by σ_{ys} and σ_{max} respectively. Material parameters such as b_{0i}, c_{0i} and k are also considered in the equation. The shear damage parameter is calculated for both the plane strain and plane stress conditions as follow:

$$d_s = \gamma_a \left(1 + k\frac{\sigma_{max}}{\sigma_{ys}}\right) = \frac{1+\upsilon}{2E}\sigma_n \left(1 + k\frac{\sigma_n}{\sigma_{ys}}\right) \tag{4.4}$$

In this chapter, Eqs. 4.1 and 4.2 are used because the tensile stress is a dominant stress in the gear tooth.

4.2.3 Mixed-mode fatigue crack model

Fig. 4.2(a) shows the side view of a typical geometry and loading of the gear tooth containing an initial crack. The crack length of 0.1 mm was chosen for this procedure for sake of accuracy when modeling fatigue crack propagation. Since this length is very small compared to the size of the gear tooth, the angle of initial crack was chosen to be 45^o without causing significant error if this angle would be different in real cases. Having the displacement and stress fields obtained around the crack-tip via FEM analysis, fracture parameters such as K_I, K_{II} and K_{III} could be calculated. Then, they were used to predict the crack front shape, crack propagation path and fatigue crack growth life of the cracked gear tooth. These analyses were conducted using the linear elastic fracture mechanics (LEFM) assumptions. In addition, the computational fracture analyses were based on the calculation of strain energy release rates (SERRs) with the aid of the modified virtual crack closure technique (MVCCT) to obtain the local SERR.

For the moving load model, a quasi-static numerical simulation method was conducted and the gear tooth engagement was broken down into multiple load steps and

analyzed separately. The contact load moved along the tooth flank and changed its direction and intensity. In order to study the effect of moving load on the gear root stress amplitude, the analysis was divided into 10 separate load cases every half load cycle as shown in Fig. 4.2(b). Force intensity for different load cases was calculated using the following equation [73]:

$$F_j = F_{HPSTC} X_\Gamma \tag{4.5}$$

where F_{HPSTC} is the highest point of the single tooth contact and X_Γ is the load sharing factor, which accounts for the load sharing between the various pairs of teeth in mesh along the path of contact for gears. No tip relief has a distribution shown in Ref. [73] and the parameter on the path of contact can be calculated as follows:

$$\Gamma_y = \frac{tan(\alpha_{y1})}{tan(\alpha_w)} - 1 \tag{4.6}$$

where α_{y1} and α_w were pressure angles at y cylinder and pitch cylinder respectively and Γ_y was the parameter on the path of contact. When analyzing the stress cycle in the gear tooth root it was determined that stress had its maximum value when the load was at the highest point of the single tooth contact. The load was the same as the one which was applied for fatigue crack initiation life simulation and the load amplitude was the same for the all cases. The maximum value of the tensile damage parameter was detected at the plane perpendicular to the surface at the root notch

when the load was at the highest point of the single tooth contact. The calculation procedure in the modified virtual crack closure technique, were conducted in two stages. In the first stage the internal nodal force, F^i, was computed at the crack-tip. Next, the crack was extended with a value of ΔA, and the analysis was performed to yield the displacements at nodes j and $j*$ which had coincided before crack growth as shown in Fig. 4.3. For a crack front modeling using the 3-D eight-node elements, the energy release rates were calculated as follows [7]:

$$\begin{cases} G_I = \frac{1}{2\Delta A} F_y^i \left(u_y^j - u_y^{j*}\right) \\ G_{II} = \frac{1}{2\Delta A} F_x^i \left(u_x^j - u_x^{j*}\right) \\ G_{III} = \frac{1}{2\Delta A} F_z^i \left(u_z^j - u_z^{j*}\right) \end{cases} \tag{4.7}$$

Then the stress intensity factors were computed from the following relations [7]:

$$\begin{cases} K_I = \sqrt{E' G_I} \\ K_{II} = \sqrt{E' G_{II}} \\ K_{III} = \sqrt{2SG_{III}} \end{cases} \tag{4.8}$$

where E' was the modulus of elasticity: $E' = E$ for plane stress problems and $E' = E/(1-\upsilon^2)$ for plane strain problems. S and υ were the shear modulus of elasticity and Poisson's ratio respectively.

For three-dimensional general mixed-mode problems the criteria of Richard et al. [90] were used for crack growth analyses. Richard criterion suggested an equivalent stress intensity factor, which was comparable to the equivalent stress in the classical stress

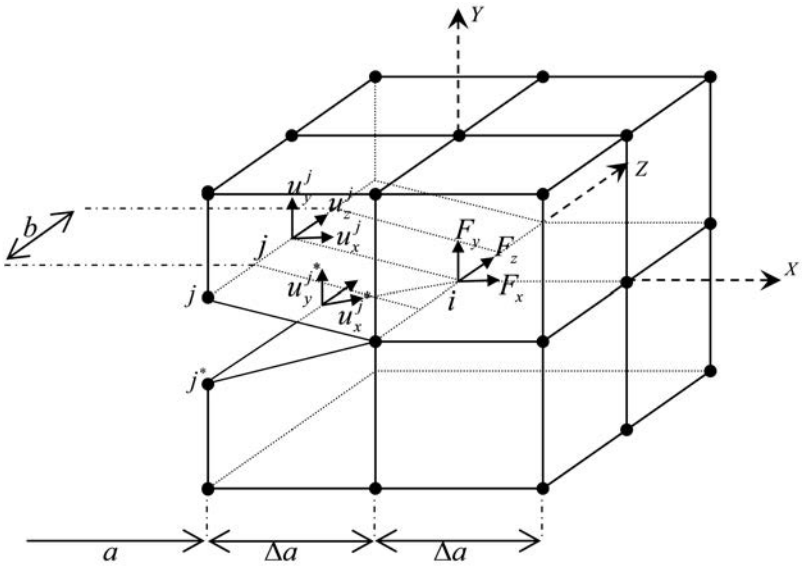

(a)

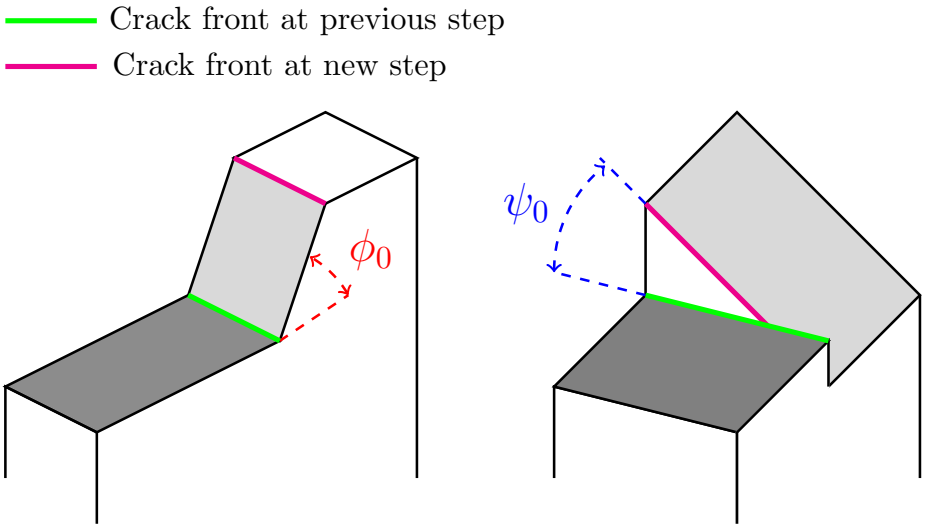

(b)

Fig. 4.3: (a) Modified virtual crack closer technique for an eight nodes solid element, (b) Crack deflection angles ϕ_0 and ψ_o for a general mixed-mode condition [4].

theories, shown in the equation below:

$$K_{eq} = \frac{K_I}{2} + \frac{1}{2}\sqrt{K_I^2 + 4(\alpha_1 K_{II})^2 + 4(\alpha_2 K_{III})^2} \tag{4.9}$$

where $\alpha_1 = \frac{K_{Ic}}{K_{IIc}}$, $\alpha_2 = \frac{K_{Ic}}{K_{IIIc}}$ and K_{Ic}, K_{IIc} and K_{IIIc} were critical stress intensity factors in various fracture modes. Deflection angles of ϕ_0 and ψ_0 are typically defined in Fig. 4.3(b) and they were calculated by the following relations [90].

$$\phi_0 = \pm\left[A\frac{|K_{II}|}{K_I + |K_{II}| + |K_{III}|} + B\left(\frac{|K_{II}|}{K_I + |K_{II}| + |K_{III}|}\right)^2\right] \tag{4.10}$$

$$\psi_0 = \pm\left[C\frac{|K_{III}|}{K_I + |K_{II}| + |K_{III}|} + D\left(\frac{|K_{III}|}{K_I + |K_{II}| + |K_{III}|}\right)^2\right] \tag{4.11}$$

where A, B, C, and D are experimental parameters with values of 140 deg, -70 deg, 78 deg, and -33 deg respectively and they are constant for isotropic materials [90].

4.2.4 Modeling crack propagation

One of the keys to estimate the fatigue crack propagation life is defining a relationship between the crack length and the loading cycles. For this purpose the Paris Law was used as follows:

$$\frac{da}{dN} = c(\Delta K)^n \tag{4.12}$$

where da and dN are crack growth increment and fatigue crack propagation life increment respectively. The material constants in Paris equation were obtained based on the ASTM E-647 method: $n = 2.954$ and $c = 3.128 \times 10^{-13}$ [73]. In the mixed-mode problems, ΔK was replaced by the effective stress intensity factor range, ΔK_{eq}, which was calculated as follows:

$$\Delta K_{eq} = \frac{\Delta K_I}{2} + \frac{1}{2}\sqrt{\Delta K_I^2 + 4(\alpha_1 \Delta K_{II})^2 + 4(\alpha_2 \Delta K_{III})^2} \tag{4.13}$$

where the values of $\alpha_1 = 1.155$ and $\alpha_2 = 1$ are used. With the calculated crack growth rate, Δa, and orientations, ϕ_0 and ψ_0, the position of the new crack-tip in the local polar coordinate could be determined. Then, the projection of the new crack-tip in the local rectangular coordinates was determined to find the components of Δa the X, Y, and Z directions.

A macro program using ANSYS Parametric Design Language (APDL) was also developed to conduct the automatic crack growth modeling process. In the finite element modeling of a gear tooth with an initial crack size, a crack propagation procedure using the recursive method was developed. At each crack growth increment a three stage model for the crack front was required [7]. In this procedure, an elastic solution was obtained first for the cracked gear tooth with the existing crack configuration. Next, the incremental crack length at each point of the crack front was calculated based on the three stress intensity factors, ΔK_{eq} values, crack growth direction angles,

and the assumed crack increment size at the surface of the gear tooth. After calculating and comparing ΔK_{eq} for all crack tip nodes through the face width, the biggest ΔK_{eq} was selected for using Paris law. The maximum crack increment of $0.1\,mm$ was assumed, and the number of fatigue cycles for crack growth was obtained. At last, the increments of the other crack tip nodes based on their own ΔK_{eq} were calculated. By considering an assumed small crack increment at the crack front node with maximum ΔK_{eq} the corresponding required load cycles (ΔN) can be calculated from Paris Law. The ratio of crack growth at each node with respect to the considered increment at the crack front node with maximum ΔK_{eq} and its direction was calculated using ΔN and the stress intensity factor values at the crack front nodes. It was noted that each increment may contain the X, Y, and Z-coordinate values for each node. Displacements of crack tip nodes should be calculated on their own $X-Y$ plane without moving in Z direction. After finding the increments of crack tip nodes in X, Y and Z-coordinates the new positions of the points were calculated by linear interpolation of the two nearest points to obtain a three dimensional new crack front shape in the second step. The detailed procedure can be found in ref [7].

To create a new crack front, the obtained points were rearranged along the face width of cracked gear tooth at the location of the (original) crack front. Then, the new positions of the considered points at the crack front were calculated by the linear interpolation of each two neighboring points to obtain a three dimensional new crack front shape. At last, new mesh of the cracked gear tooth was constructed using the updated crack front geometry. This procedure was repeated for each crack growth in-

crement. The main steps of the developed APDL program to conduct the automatic 3D crack propagation procedure were as follows:

i. Geometry and finite element mesh generation of the cracked gear tooth

ii. Definition of loading, constraints, and material properties

iii. Implementation of a linear elastic solution

iv. Calculation of nodal forces and nodal displacements at the crack front in three directions

v. Calculation of G_I, G_{II} and G_{III} and then K_I, K_{II} and K_{III} at the crack front using modified crack closure technique (Eqs. 4.7 and 4.8)

vi. Calculation of crack deflection angles ϕ_0 and ψ_0 at various points of the crack front

vii. Calculation of K_{eq} at various points of the crack front using Eqs. 4.13

viii. Consideration of a $0.1\,mm$ crack increment at the crack front node with maximum ΔK_{eq} surface at each increment and calculation of the corresponding load cycles (ΔN) using Paris Law

ix. Calculation of ΔN and values of K_I, K_{II} and K_{III} at the crack front nodes the ratio of crack growth at each node with respect to the $0.1\,mm$ growth at the crack front node with maximum ΔK_{eq} surface and generation of the new crack front shape as explained above

x. Construction of new geometry of the cracked gear tooth with new crack front shape

xi. Reconstruction of the finite element model based on the new crack length and the crack front configuration

xii. If $K_{eq} \leq K_{Ic}$ or crack length at the crack front node with maximum ΔK_{eq} surface was less than a defined value, return to step (iii)

xiii. Formation of the results and cessation of the solution.

This process was repeated at each crack propagation increment. The flowchart of the developed APDL program for the fully automatic fatigue crack growth processing in general mixed-mode condition is shown in Fig. 4.4.

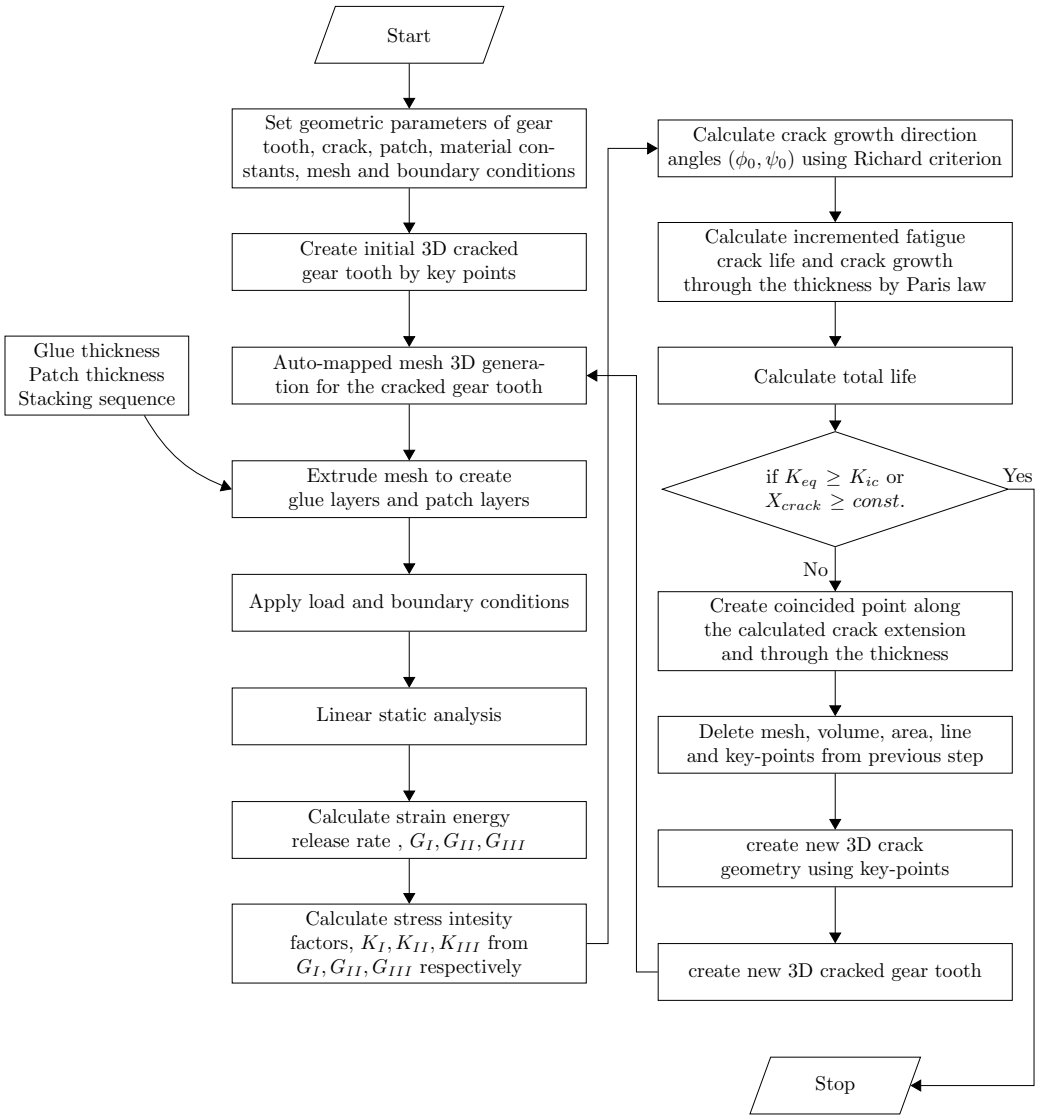

Fig. 4.4: Flowchart of the APDL program for automatic fatigue crack growth in general mixed-mode conditions.

A sensitivity study on crack increment size was also performed. For the virtual crack closure technique, the energy release rates were defined as the virtual crack closure integral over a finite crack closure length. This crack closure length corresponds

to the lengths of the elements adjacent to the crack front. The element length, a, must be chosen small enough to assure a converged FE solution but large enough to avoid oscillating results. The energy release rates used for fracture predictions and the ones employed for material characterization must be consistent. This does not imply that the material tests must be evaluated by FE-models, but it should be established that the data reduction scheme is in agreement with the definition of a finite crack closure length. Consequently, it was suggested to use element lengths at the crack tip in such a manner that the computed results were insensitive to the variation of the element length a at the crack tip. Krueger [91] recommended considering $\Delta a/h$ value between 0.01 and 0.1 for this purpose where Δa is element length and h is the face width of the cracked panel. It was noted that for the increment sizes larger than $0.5\,mm$, the obtained crack fronts and crack trajectories were not smooth as predicted. However, there were no significant differences from the results (crack front, trajectory, and life) obtained with the increment sizes smaller than $0.1\,mm$.

In this chapter, we take the number of loading cycles which results in the crack propagation of $5\,mm$ in X-direction as the fatigue crack propagation life.

4.3 Fatigue crack initiation life

As it was mentioned, an elastic and isotropic material model, without any imperfections or initial damage, was assumed. The Hertzian contact pressure was moving along one surface of the gear tooth and friction force was also considered to

detect fatigue crack initiation. The fatigue crack initiation life was then calculated using Eqs. 4.1 or 4.3.

During the simulation, the moving contact loading started at the root of gear tooth, and moved along the contact surface until the top of the gear tooth has the same aspect shown in the Fig. 4.1. It was found that the principle normal stress was dominant. Fig. 4.5 illustrates the contour of the principle stress after the first cycle of loading. It can be seen that the maximum principle stress exists at the root of the gear tooth, where the initial crack occurs. Therefore, eq. 4.1 was selected to predict the fatigue crack initiation life.

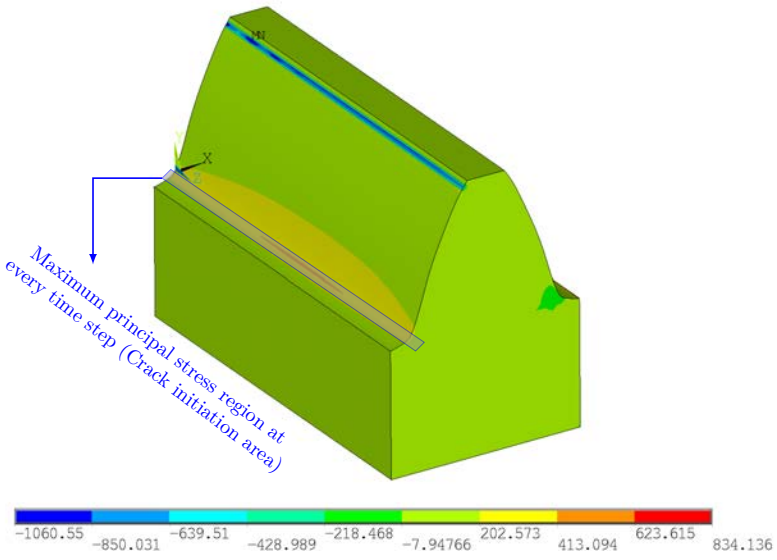

Fig. 4.5: Principle stress contour for one step of loading.

Fig. 4.6 shows the evolution of Tresca stress during one loading cycle. The Tresca stress was normalized by the amplitude of contacting loading pressure, $P_0 = 1550\,MPa$. This stress history helped to determine the fatigue crack initiation life via Eq. 4.1. It can be seen that the Tresca stress was higher with a larger friction coefficient,μ.

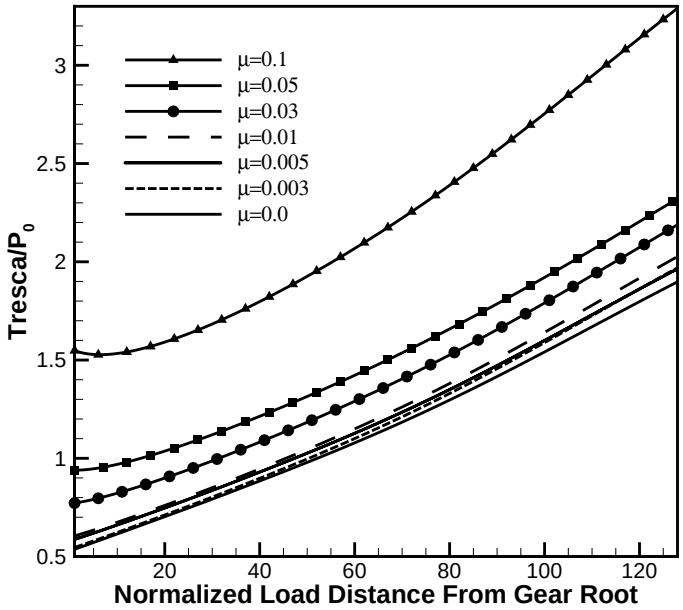

Fig. 4.6: Maximum Tresca stress at the critical plane on the contact surface.

[H] Fig. 4.7 shows that the fatigue crack initiation life is predicted in the range of $E10$ cycles. This could be unpractical at first but with a simple calculation it can be shown that these cycles could be happened in one year or more depending on

the gear tooth rotation speed. Burton et al. [92] shows that low speed shafts have typically around $30 - 100$ rpm speed and high speed shafts have a speed around $300 - 1500$ rpm.

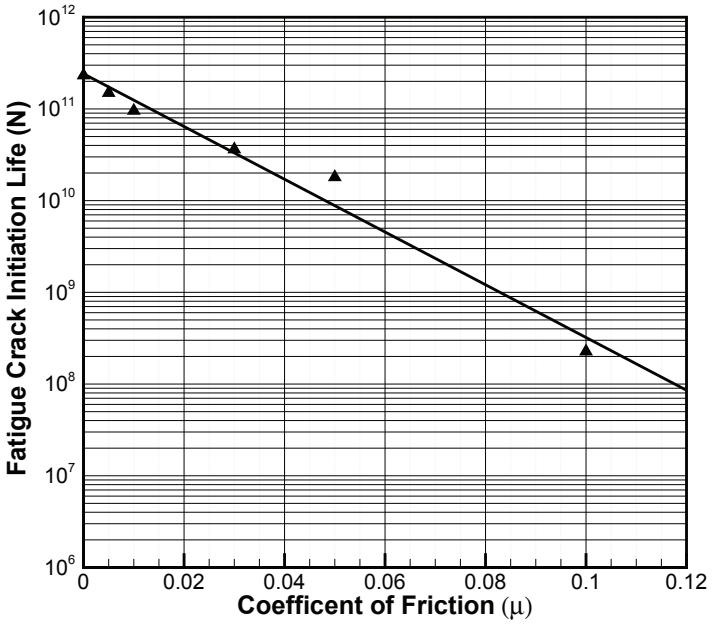

Fig. 4.7: Number of loading cycles, when initial crack appears at the observed material point.

Fig. 4.7 also indicates that a variation of fatigue life was almost logarithmic by changing the coefficient of friction. The initial crack was found to be located along the maximum principle stress line at the root of the gear as shown in Fig. 4.5.

4.4 Fatigue crack propagation model

To validate the developed FEM procedure, the predicted crack growth behavior of a plain panel containing a 45^o central inclined crack was compared with the available experimental results [5] in Fig. 4.8(a). The agreement between the experimental and the numerical results was demonstrated. In addition, fatigue crack trajectory calculated by three-dimensional crack growth modeling was compared with the results from Pehan et al. [6] and shown in Fig. 4.8(b). It was noted that a two-dimensional crack trajectory was modeled in [6], the crack growth line was the same through the face width of the gear tooth. However, since the three-dimensional crack growth modeling was employed in this Chapter, the crack trajectory was shown to change at different points through the face width. Therefore, in Fig. 4.8(b) crack trajectories for the edge of the crack and for the middle line of the crack have been depicted as this studys result. Fig. 4.8(b) also shows a good agreement between Pehans results and the simulated crack trajectory obtained at middle line of the crack.

4.4.1 Moving contact loading through the whole face width

After finding the location of initial crack from the previous section and applying it to the mixed-mode fatigue crack model, fatigue crack propagation can be simulated. As depicted in Fig. 4.9, we first studied the cases in which the contact load was applied through the whole face width of the gear tooth with an initial crack at the root. The following results will be discussed in this section: variations of

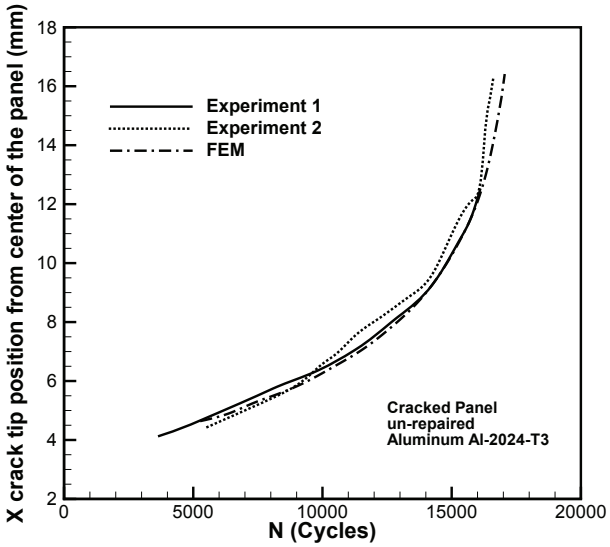

(a)

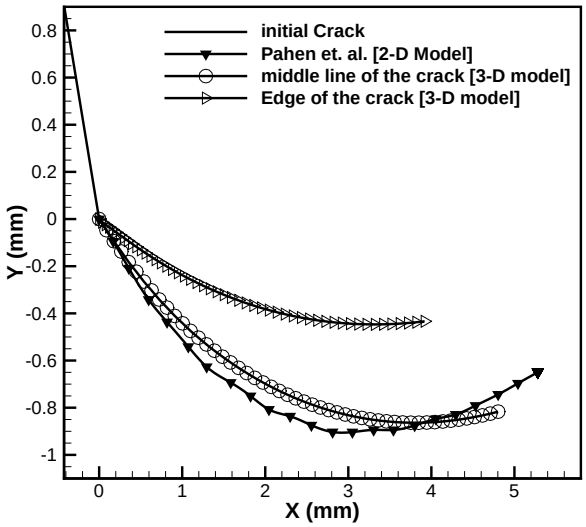

(b)

Fig. 4.8: (a) Comparison between the predicted Fatigue crack growth life behaviors with experimental results of ref. [5], (b) Comparison between the predicted crack growth paths with previous results of ref. [6].

stress intensity factors through the face width, crack trajectory, and fatigue crack propagation life of the gear tooth.

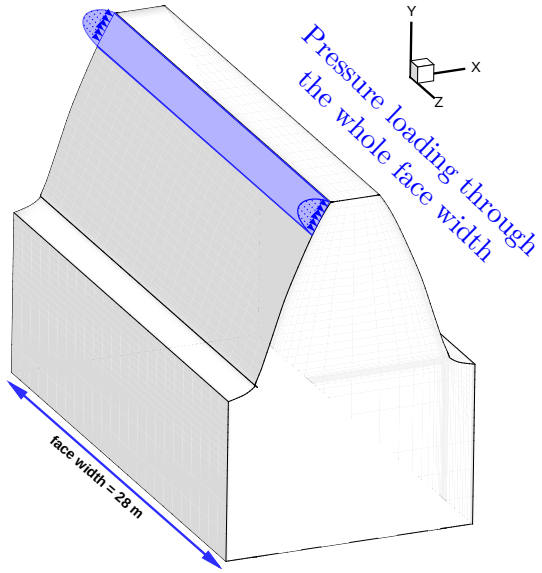

Fig. 4.9: Applied Contact load through the face width of the gear tooth.

Fig. 4.10 shows the variations of stress intensity factors (K_I, K_{II} and K_{III}) along the initial crack front before the occurrence of crack growth. It can be seen that the values of K_{II} and K_{III} (Fig. 4.10(b) and 4.10(c) respectively) stress intensity factors along the crack front are very small and therefore mode-I as shown in Fig. 4.10(a) is the dominant fracture mode. Fig. 4.10(a) also shows that the mode-I stress intensity factors at the crack front of the cracked gear tooth are considerably reduced from the midpoint to the edge of the gear tooth. On the other hand, the

variation of K_{II} in Fig. 4.10(b) indicates that the crack tilted more at the center of the gear tooth than at the edges.

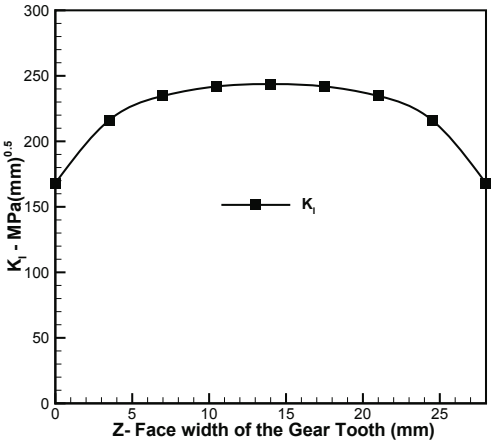

(a)

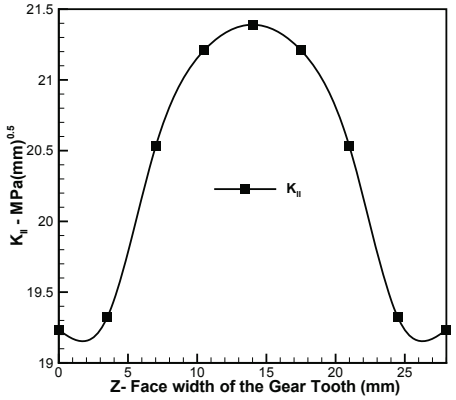

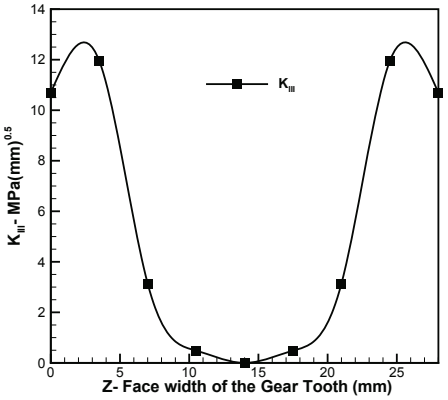

(b) (c)

Fig. 4.10: Variation of stress intensity factors along the face width of the gear tooth; (a) K_I , (b) K_{II} , (c) K_{III}.

Fig. 4.11 illustrates the growth of crack length in the X-direction versus the number of load cycles as the crack propagated in the gear tooth. It was noted that the major component of crack growth both inside and at the edge of the gear tooth were in the X-direction. Therefore, variations of fatigue crack growth lives were presented with respect to the X-coordinate of the crack increments in all cases.

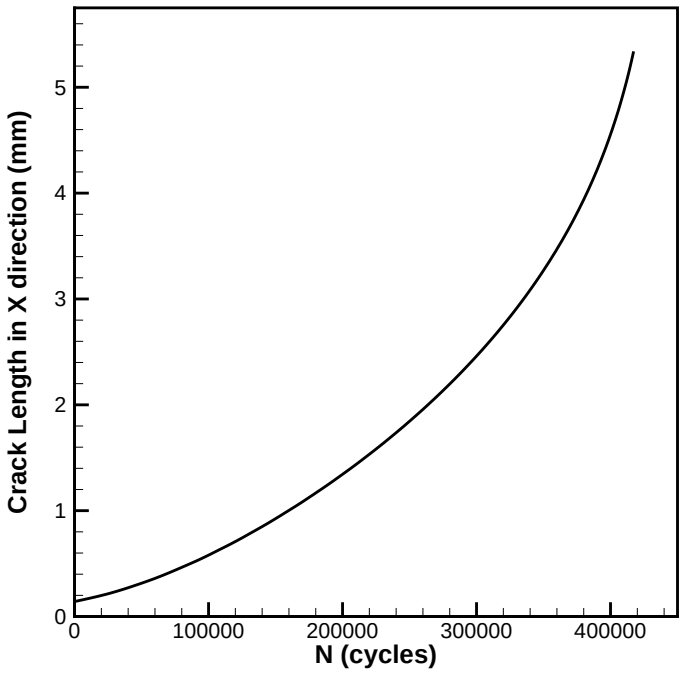

Fig. 4.11: Predicted fatigue crack growth versus the number of load cycles.

Fig. 4.12 shows how the crack propagated in the gear tooth subject to the moving contact load. The crack trajectories in two different planes are shown here.

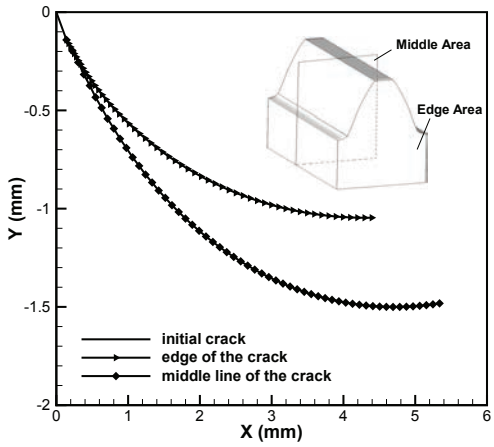

(a)

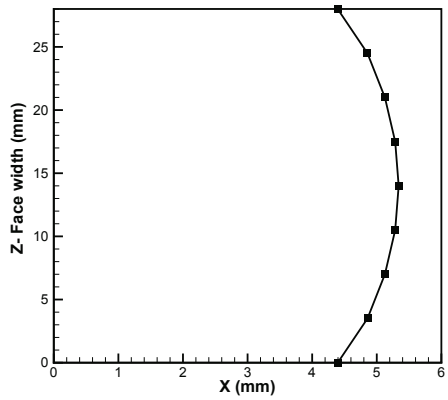

(b)

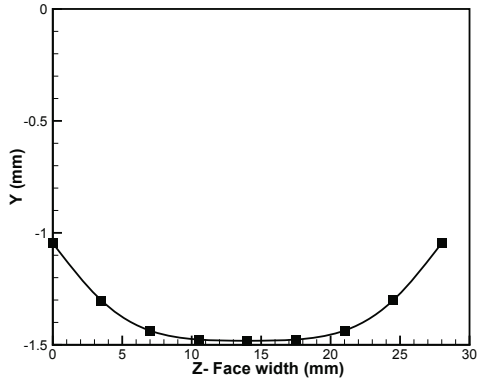

(c)

Fig. 4.12: (a) Prediction of crack trajectories in X-Y plane, (b) Predicted crack front shapes in Z-X plane, (c) Predicted crack front shapes in Z-Y planel.

One was located on the edge of the gear tooth and the other was at the middle section of the gear tooth. As it was discussed above, it was predicted that at the middle area of the gear tooth the crack would be tilted in Y direction rather than the

edges. Since the largest K_I was at the middle, the crack had its longest length at the middle of the gear tooth. This claim is shown in Fig. 4.12(b) and Fig. 4.12(c).

Fig. 4.13 illustrates a three-dimensional view of the crack surface after propagation.

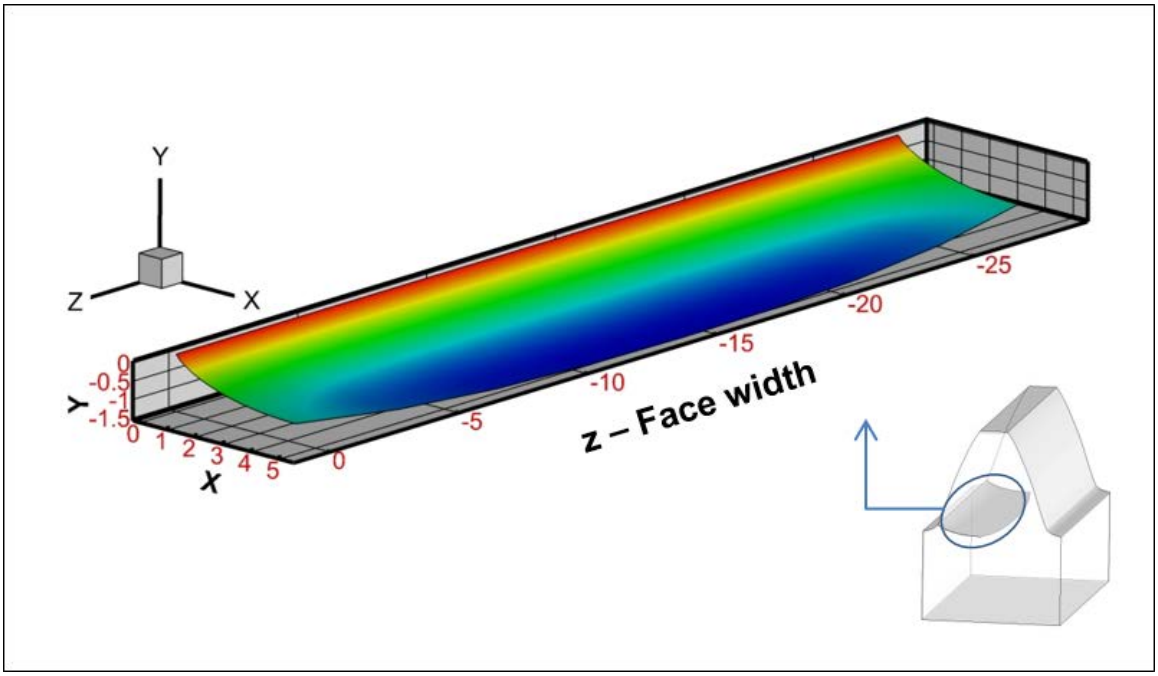

Fig. 4.13: Predicted crack surface after propagation.

4.4.2 Loading through the partial face width

Some imperfections in contact loading due to misalignment of the gear were considered to study their effect on stress intensity factors and crack trajectory. In this case, the moving contact load was applied on the partial face width of the gear tooth as shown in Fig. 4.14. The following various widths were considered: $7\,mm$, $14\,mm$ and $21\,mm$. The results were then compared with the ones from the previous

case in which the contact load was applied on the whole face width of the gear tooth.

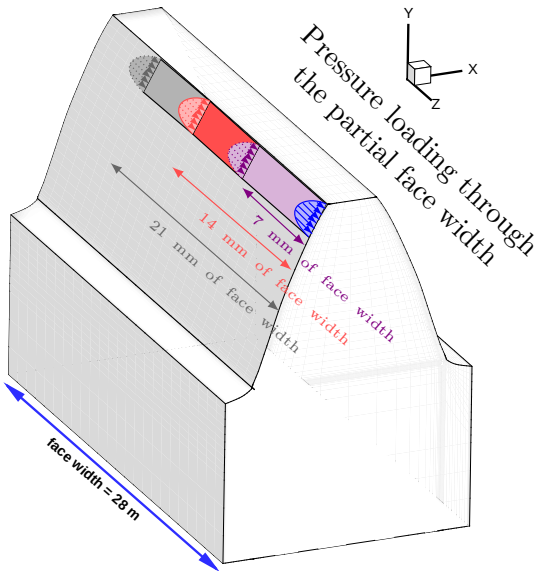

Fig. 4.14: Applied Contact load through the partial face width.

At first, variations of the stress intensity factors through the face width for the cases with load imperfection and the case without load imperfection were compared and shown in Fig. 4.15. In the cases with load imperfection there was a pressure at one side of the gear tooth and the crack length was predicted to be longer at that side than the other side which was not loaded. The reason for this claim was that the dominant stress intensity factor was K_I and two other stress intensity factors were much smaller. Therefore, K_I will have most influence on crack length in such a way that a larger value predicts bigger crack growth. Fig. 4.16 shows the comparison of

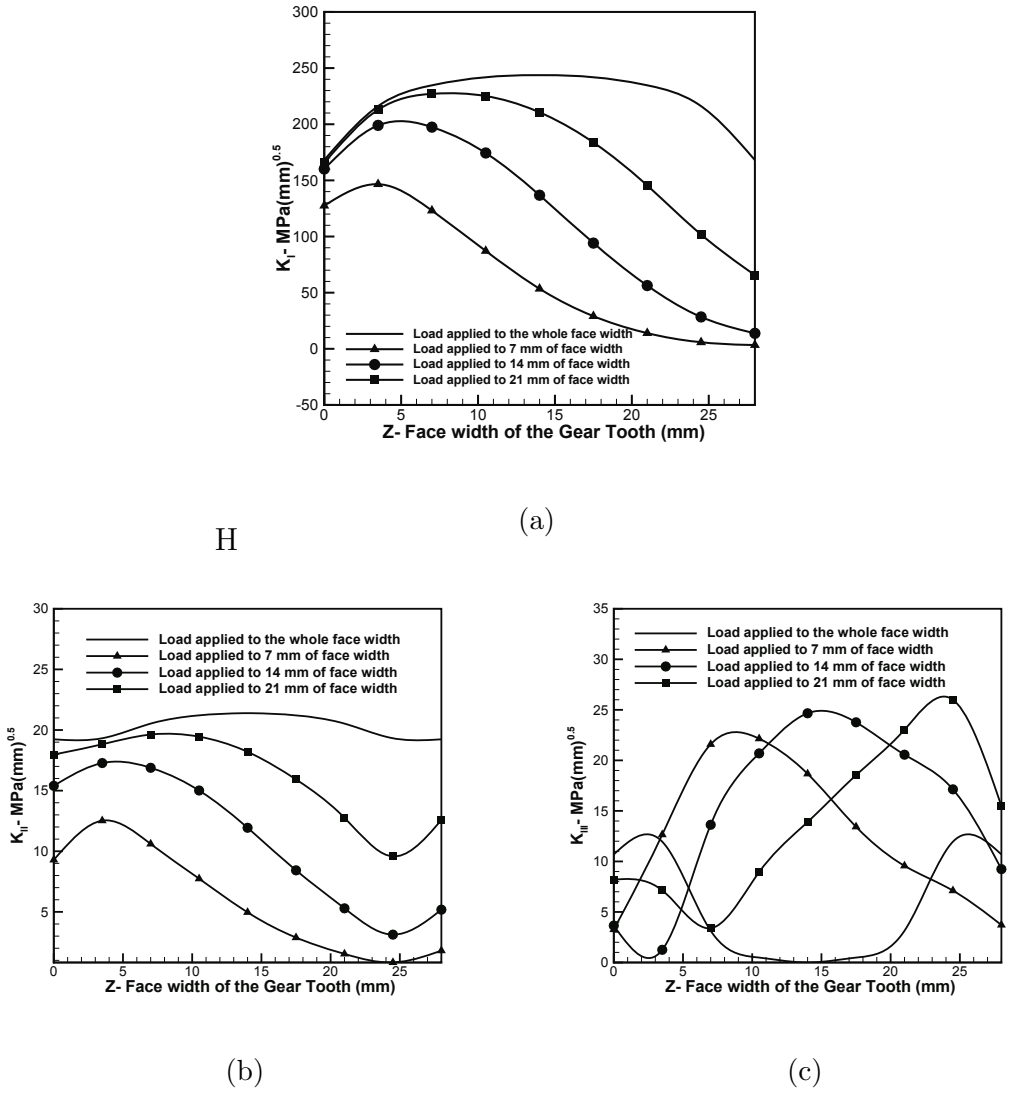

Fig. 4.15: Variation of stress intensity factors along the face width for both cases (first case: Contact load through the whole face width; second case: Contact load through the partial face width); (a) K_I , (b) K_{II} , (c) K_{III}.

the fatigue crack propagation life between different cases of load contact area and constant load amplitude. The fatigue crack propagation life increased as the load contact area was reduced. For instance, the fatigue crack propagation life for crack propagating $5\,mm$ in X-direction was $900,000$ cycles for the case in which the load was applied to $14\,mm$ of the face width while such a fatigue life was $400,000$ cycles for the case in which the load was applied through the face width of the gear tooth.

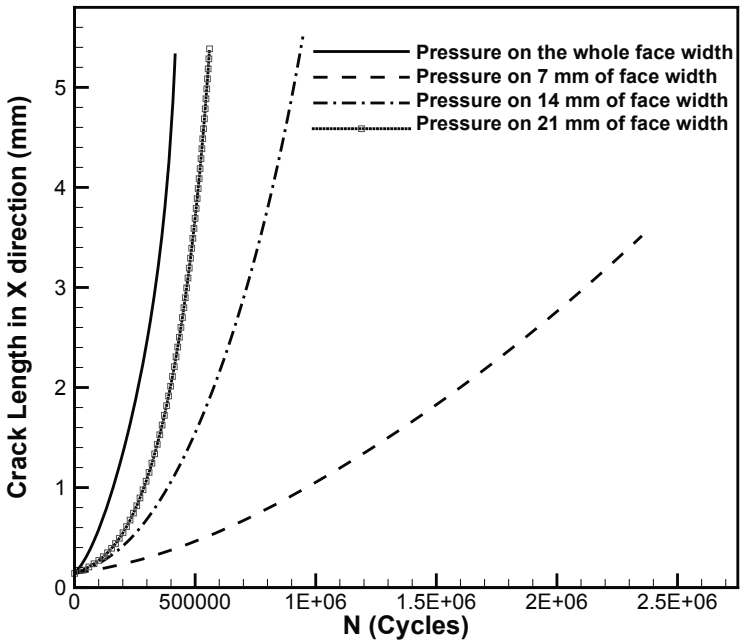

Fig. 4.16: Predicted fatigue crack growth versus the number of load cycles.

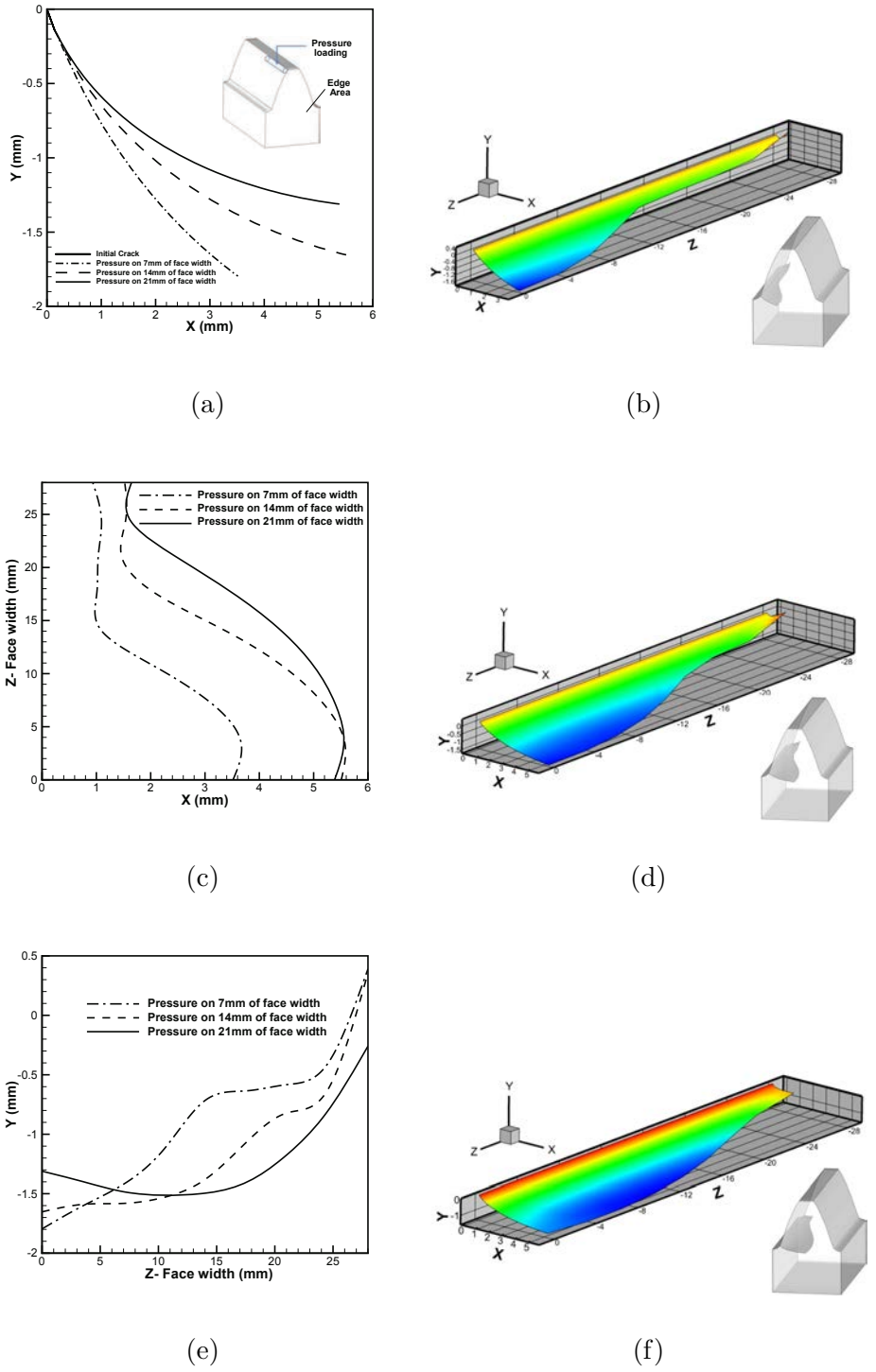

Fig. 4.17: (a) Prediction of crack trajectories in X-Y plane, (b) Predicted crack surface after propagation(Load applied to 7 mm of the face width), (c) Predicted crack front shapes in Z-X plane, (d) Predicted crack surface after propagation(Load applied to 14 mm of the face width), (e) Predicted crack front shapes in Z-Y plane, (f) Predicted crack surface after propagation(Load applied to 21 mm of the face width).

Fig. 4.17 shows the crack trajectory in $X-Y$ plane as well as the crack fronts in $X-Z$ and $Y-Z$ planes. As shown in Fig. 4.17(a), the crack trajectories at the edge were different for different loadings. Since the load was applied on the partial face width of the gear tooth, the crack grew unevenly through the face width. This claim is shown clearly in Fig. 4.17(c) and 4.17(e). In addition, Fig. 4.17(a) and 4.17(e) indicate that the crack was tilted in positive direction of the Y axis at the edge where no moving contact load was applied.

It was also shown that as the load contact area was increased the crack was prone to increased tilting in Y direction. Fig. 4.17(b), 4.17(d), 4.17(f) shows three-dimensional views of the crack surfaces for different cases after the crack propagated. The crack front with imperfect loading was totally different than the case without load imperfection.

4.5 Extension of fatigue crack propagation life

In this section the cracked gear tooth was repaired with Boron/Epoxy patches. The effect of the composite layers on enhancing fatigue crack propagation life of the gear tooth was analyzed. Both single side repair and double side repair were studied. Similar to the methods in previous literatures [7, 91] for repairing Aluminum panels with composite patches, a small de-bonding between the gear tooth and adhesively bonded composite patch was considered. According to Aggelopoulos et al [93], patch end de-bonding does not affect the stress magnification factor up to relatively large

de-bonded lengths (60% of patch length overall). Fig. 4.18 shows the model of the gear tooth being repaired by the composite patches that were used on both sides of the cracked gear tooth.

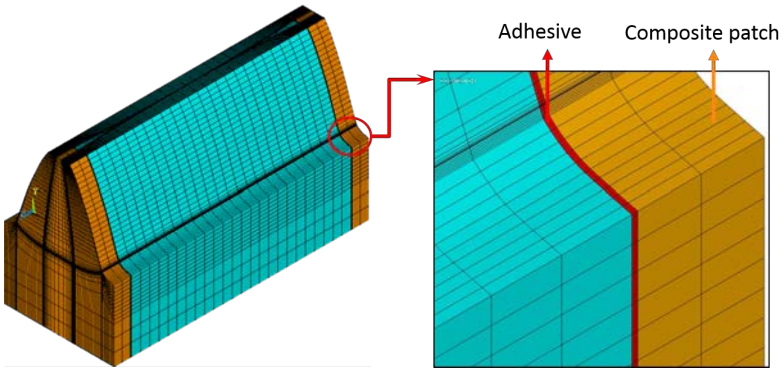

Fig. 4.18: Typical meshing of the repaired gear tooth with composite material.

In the three dimensional analysis, an isotropic 8-node-solid element (SOLID45) was used to model the adhesive layer and a layered 8-node-solid element (SOLID46) was used to model the composite patch. As shown in Fig. 4.18, the model includes 2 elements along the adhesive thickness and 2 elements along the patch thickness. A small de-bonded area equal to the element size at the crack edges was considered in the FEM modeling. Adhesive layer and Boron/Epoxy material properties can be found in [4]. To validate the developed FEM procedure, the predicted crack growth behavior of repaired plain panel with Glass/Epoxy composite patch lay-up of $[105]_4$,which indicates 4 layers of composite with angles of 105^o for each layer, was compared with the available experimental results [7] as shown in Fig. 4.19. The agreement between

experimented and the predicted finite element results was demonstrated.

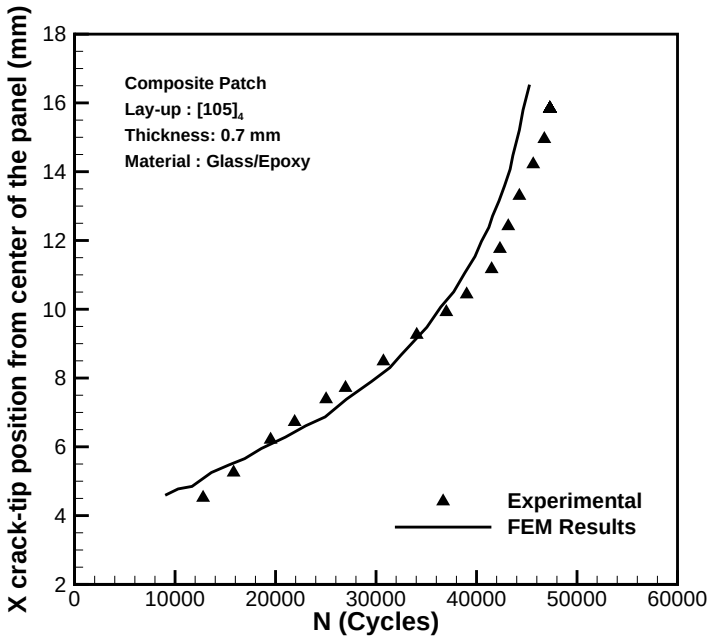

Fig. 4.19: Comparison between the predicted Fatigue crack propagation life behaviors with experimental results of ref. [7].

4.5.1 Loading through the whole face width of gear tooth

The same load described in section 4.4.1 was applied to the gear tooth, and the effects of different composite patches on enhancing the fatigue crack propagation life were studied. Four different patch lay-ups of $[90]_4$, $[90]_{12}$, $[90]_{20}$ and $[90]_{30}$ at both sides of the gear tooth were considered. The fatigue crack propagation lives are shown in Fig. 4.20.

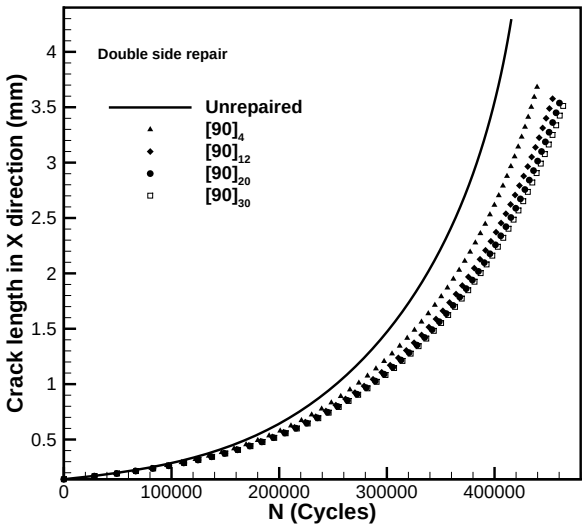

(a)

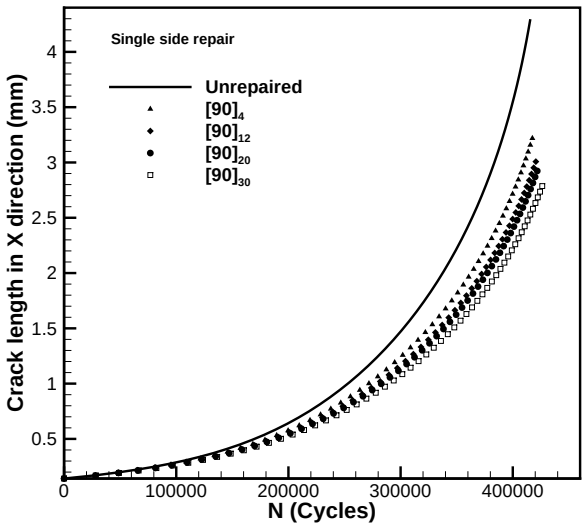

(b)

Fig. 4.20: Predicted fatigue crack propagation life for different composite patch lay-ups, (a) Double side repair, (b) Single-side side repair.

According to Fig. 4.20(a), the fatigue crack propagation life was extended by 16% when the patch lay-up of $[90]_{30}$ was used. This enhancement percentages for patch lay-ups of $[90]_4$, $[90]_{12}$, and $[90]_{20}$ are 9%, 13%, and 15% respectively.

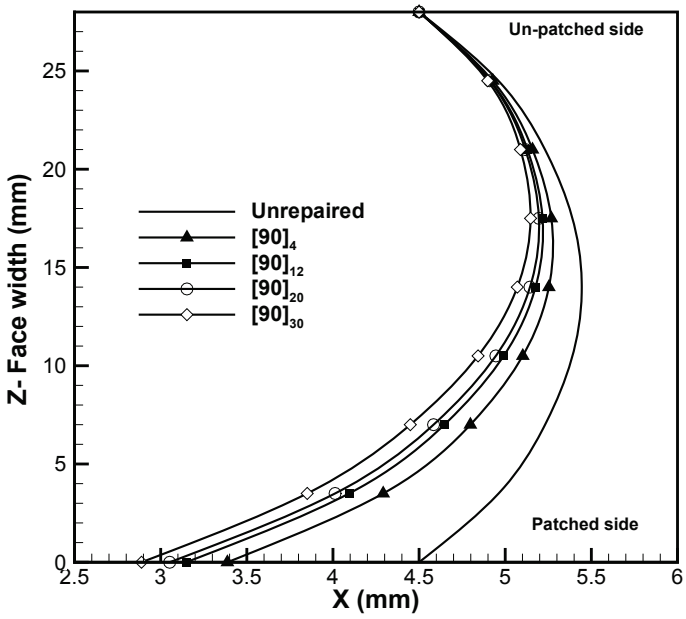

Fig. 4.21: Prediction of crack front in X-Z plane for different repair patch thicknesses.

It was observed that patches with more layers result in higher out of plane bending which could cause misalignment in gear tooth rotating. In another study, we used one side repair on gear tooth instead of double side to demonstrate the effect of different repairs on enhancing the fatigue crack propagation life of the gear tooth. Fig. 4.20(b) shows fatigue crack propagation life when different patches were used for

single side repair. A 13% extension of fatigue crack propagation life of gear tooth repaired by single side patch lay-up of $[90]_{30}$ was observed. The single side patch lay-ups of $[90]_4$, $[90]_{12}$, and $[90]_{20}$ increase the fatigue crack propagation life of the gear tooth for 9%, 10%, and 11% respectively.

Fig. 4.21 shows the crack length would be different at both edges if single side repair is used. These results indicate that the crack in patched side grows slower than unpatched side and the biggest difference is 36% when the patch lay-up of $[90]_{30}$ is used. The percentages are 24%, 30%, and 32% when the patch lay-ups of $[90]_4$, $[90]_{12}$, and $[90]_{20}$were used respectively. Therefore, results show that the composite patch would make the crack propagation slower and increase the fatigue crack propagation life of the gear tooth.

4.5.2 Loading through the partial face width of gear tooth

In the last section of the study, we investigated the effectiveness of the composite repair under partial loading which could be occurred due to misalignment of the gear tooth. We also considered different composite patch lay-ups for repairing the gear tooth under partial loads as discussed before. Composite patches were applied on the side closer to where the load was applied. Fig. 4.22 shows that patch lay-ups of $[0]_{30}$, $[90]_{30}$, and $[45]_{30}$ increased the fatigue crack propagation life of the gear tooth by 15%, 24%, and 29% respectively. Patch lay-up of $[45]_{30}$ increased the fatigue crack propagation life more than the two other patches. This was because the angle of

layers were nearly perpendicular to the crack trajectory meaning the patch lay-up of $[45]_{30}$ were more durable to prevent crack opening compared to other patch lay-ups whose layers were not perpendicular to the crack trajectory. Fig. 4.22 shows crack propagation along the patched side of the gear tooth.

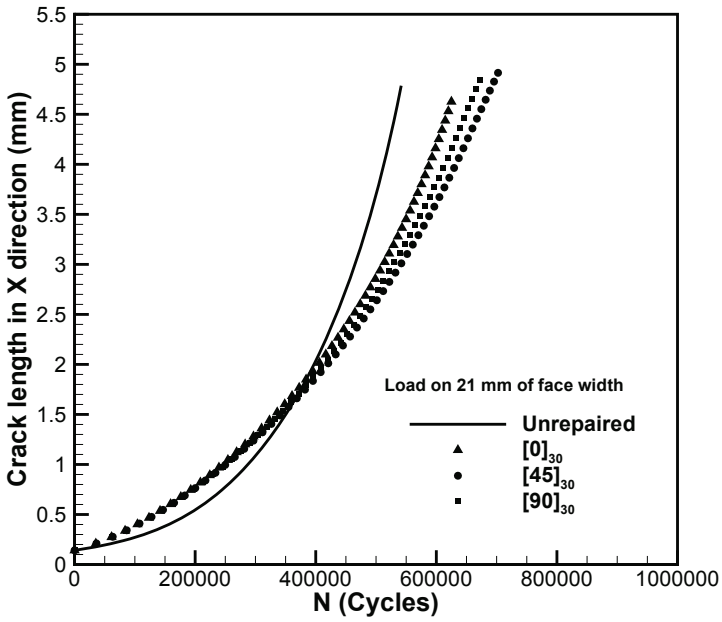

Fig. 4.22: Predicted fatigue crack propagation life for different composite patch lay-ups (Load applied to 21 mm of the face width).

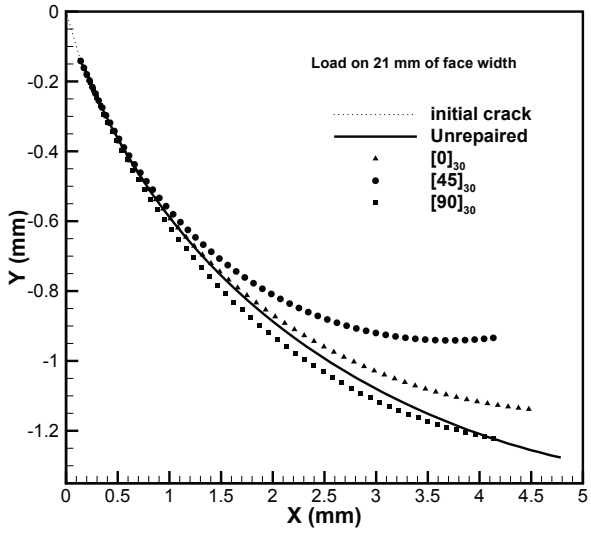

(a)

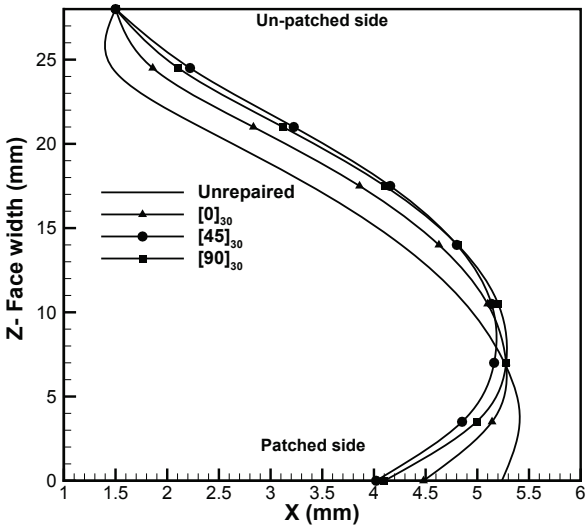

(b)

Fig. 4.23: (a) Prediction of crack trajectories in X-Y plane, (b) Prediction of crack front in X-Z plane.

After comparing the effect of different patch lay-ups on fatigue crack propagation life of the gear tooth, we studied the effect of the composite patches on the crack trajectory. Fig. 4.23(a) shows the composite patch lay-up of $[45]_{30}$ changed the crack trajectory more than the two other lay-ups when the load was applied on 21 mm face width of the gear tooth.

As shown Fig. 4.23(b) the crack propagation length along the patched side was bigger than the un-patched side since the pressure was applied to the patched side of the gear tooth. Therefore we applied the patch repair closer to the load when a partial load was applied. Fig. 4.23 also shows that the major difference of crack front between un-repaired gear tooth and the repaired ones are near the patched side.

4.6 Conclusion

Three-dimensional finite element analyses were conducted to study both fatigue crack initiation and fatigue crack propagation in a gear tooth. Linear elastic fracture mechanics approach was employed here to model mixed-mode fatigue crack propagation in a gear tooth after a fatigue crack was initiated. Two various load conditions were considered: the contact load acting along the whole face width or the partial face width of gear tooth. Those two load conditions resulted in different crack trajectories, stress intensity factors and fatigue crack propagation lives for the gear tooth. In addition, it was shown that Boron/Epoxy patches would enhance the fatigue crack propagation life of the gear tooth. Future studies include investigating

the enhancement on gear tooth fatigue life due to composite patches with various materials and layers.

CHAPTER 5
STUDYING BEARING FAILURE USING PERIDYNAMICS (MACRO SCALE)

5.1 Introduction

Fracture is one of major concerns in engineering field for a long time, and many scientists have made substantial efforts in order to understand material failures and prevent potential dangers. Inglis, Griffith, were the pioneers who made contributions to the early development of fracture analyses [94]. By developing the energy release rate, Irwin extended the Griffith approaches [94, 95] in early 1950s. Although the classical fracture mechanics provides a more reliable methodology for engineering design than the traditional strength based approach, it has its limitations. For instance, a pre-existing (initial) crack has to be defined, and the fracture process zone is required to be small compared to geometrical dimensions [96, 97].

As mentioned in Chapters 3 and 4, numerical predictions of crack initiation and growth are considered as a class of challenging problems in mechanical engineering. Approaches based on classical continuum mechanics fail to describe discontinuities on crack surfaces since the theory is formulated in partial differential equations and a specific spatial derivative which does not exist on the singularities. In order to model crack growth and material damage, significant amount of researches have been done. Dugdale [98] and Barenblatt [99] in early 60s introduced the cohesive crack models to address relationships between the cohesive tractions resisting the separation of cracks and the crack opening displacement [100]. The cohesive zone models have

been implemented into finite element models with introducing interface elements and contact surfaces. In addition, many researchers have adopted cohesive zone models in numerical simulations. Some examples include implementing a cohesive zone model in nonlinear finite element formulations by Foulk et al. [101] and studying dynamic mixed-mode fracture using three-dimensional cohesive models by Ruiz et al. [100]. Overviews of cohesive crack models were presented by Elices et al. [102] and Planas et al. [103].

Melenk and Babuska [104] presented the partition of unity finite element method and then Belytschko and his colleagues [105–107] investigated the partition of unity principle for numerical simulations of fracture problems. They introduced the extended finite element method (XFEM) to alleviate shortcomings of the conventional finite element method so that the discontinuities are not constrained to element boundaries and can be modeled without remeshing [108]. Moes and Belytschko [106] used the XFEM to simulate the growth of arbitrary cohesive cracks, and Sukumar et al. [107, 109] implemented extended finite element method with Dynaflow and conducted crack growth simulations of channel-cracking in thin films. More XFEM simulations can be found in Mariani and Perego [110], Cox [108], Meschke and Dumstorff [111], and many others.

Unlike FEA in which elements are connected by a topological mesh, meshfree particle methods were developed based on using a finite number of discrete particles to describe the state of a system [112–116]. Meshfree particle methods eliminate mesh constraints and demonstrate advantages in many applications including crack prop-

agation simulations, large deformation analyses and fluid-structure interactions (FSI).

5.2 Peridynamics

Peridynamics is a relatively new method comparing to the classical continuum mechanics. This method is converged to the classical theory, and its numerical applications have been studied since early 2000s. Silling [117] first introduced this theory as an alternative theory of continuum mechanics to solve problems involving spontaneous formations of discontinuities without any special treatment on discontinuities. Spatial derivatives are eliminated in the peridynamics theory, and this is the main difference between peridynamics and most other classical theories. The theory in Silling's paper [117] is specified as the bond-based peridynamics since a pairwise force function is used to describe the interaction between two material points. Silling and other researchers then developed state-based peridynamics.

Silling et al. [118] used the peridynamic formulation to study the deformation of an infinite elastic solid and found out that the peridynamics solution converges to the classical solution as the horizon goes to zero. In addition, the conclusion shows that some features of peridynamics, including the oscillation of the displacement field decaying from the loading region and spreading out to infinity, are not presented in the classical theory. In the classical theory, the displacement field is two-order smoother in derivatives than the body force field. However, in Peridynamics, it is found that the same smoothness between the displacement field and the body force field.

Although the peridynamics employees a set of particles to model the continuum, the main theoretical difference between the peridynamics and the meshfree methods is that the peridynamic approach solves a different set of continuum equations. The integral equations of the peridynamic model remain directly applicable even for the models having discontinuity, while the PDEs of the other classical theories do not. One practical application is that cracks appear automatically in a peridynamic model as a natural consequence of the equation of motion and constitutive models. In addition, the peridynamic model is based on interacting forces between pairs of particles, and therefore does not require a large number of neighboring particles to determine spatial derivatives. A consequence of this pairwise interaction approach is that the peridynamic method does not suffer from the "tensile instability"in meshfree methods such as SPH.

Many applications of peridynamics have been studied based on the general applicability of the theory. First study on the numerical simulation using the peridynamic model was introduced by Silling and Askari [119]. In their study, the bond-based peridynamics was used to study the numerical convergence in an opening-mode fracture case and the impact of a sphere on a brittle target. Kilic and Madenci [120, 121] studied structural stability and failure analysis, and in that work peridynamics was used to predict crack paths in a quenched glass plate. Some other studies have been conducted in fracture mechanics using peridynamics [122–125], and peridynamics has also been applied to study composites [126–129].

A generalized formulation of bond-based peridynamics was extended by Silling et al.

[130], which is referred to as the state-based peridynamics. The interaction between two material points might not be along the direction of the deformed bond in the state-based peridynamics. In addition, a force state similar to the stress tensor in the classical continuum mechanics is introduced. Based on the study of convergence by Silling and Lehoucq [131], it is shown that the peridynamics stress tensor convergences to a Piola-Kirchhoff stress tensor as the length scale goes to zero. Using the state-based peridynamic method, Warren et al. [132] presented elastic deformation and fracture of a bar, and Foster et al. [133, 134] studied viscoplasticity. Silling and Lehoucq [135] conducted the development of peridynamic theory of solid mechanics.

5.3 Methodology

5.3.1 Peridynamic formulation

In this chapter, only the bond-based peridynamics is discussed. The equation of motion in the classical continuum mechanics is derived from the principle of linear momentum that the rate of change of linear momentum equals the force applied on the body as [136]

$$\rho\ddot{\mathbf{u}} = \nabla.\boldsymbol{\sigma} + \mathbf{b} \tag{5.1}$$

where ρ is the density, $\ddot{\mathbf{u}}$ is the acceleration vector, $\boldsymbol{\sigma}$ is the stress tensor, and $\mathbf{b}$ is the body force vector.

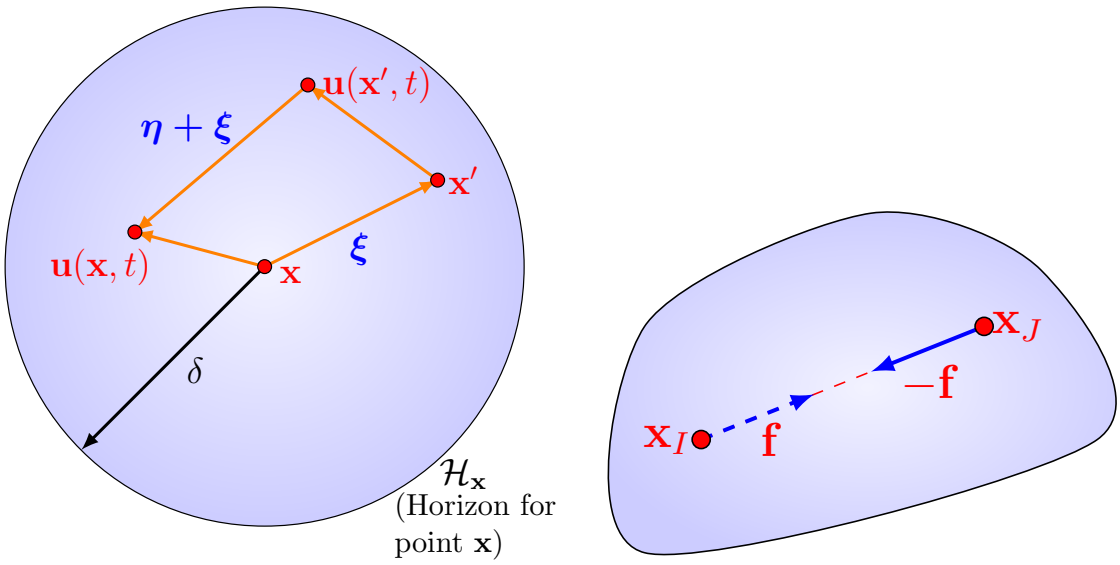

(a) (b)

Fig. 5.1: (a) Relationships among relative position vector and the relative displacement vector within a peridynamic horizon. (b) Pairwise force vector.

This formulation requires a unique spatial derivative which does not exist along discontinuities. However, peridynamics employs integration to calculate the force on a material point, and the equation of motion of the material point at $\mathbf{x}$ in the reference configuration at time t, as depicted in Fig. 5.1, is written as [137]

$$\rho\ddot{\mathbf{u}}(\mathbf{x},t) = \int_{\mathcal{H}_{\mathbf{x}}} \mathbf{f}(\boldsymbol{\eta},\boldsymbol{\xi})dV_{\mathbf{x}'} + \mathbf{b}(\mathbf{x},t) \tag{5.2}$$

where $\mathbf{f}$ is a pairwise force vector that the material point at $\mathbf{x}'$ exerts on the material point at $\mathbf{x}$, and $\mathcal{H}_{\mathbf{x}}$ is a domain (neighborhood) of the material point at $\mathbf{x}$ with a horizon radius of δ. The relative position vector in the reference configuration shown

in Fig. 5.1 is written as [119]

$$\boldsymbol{\xi} = \mathbf{x}' - \mathbf{x}, \qquad \mathbf{x}' \in \mathcal{H}_{\mathbf{x}} \tag{5.3}$$

and the relative displacement vector at time t is expressed as

$$\boldsymbol{\eta} = \mathbf{u}(\mathbf{x}', t) - \mathbf{u}(\mathbf{x}, t) \tag{5.4}$$

For each material point, there is a positive number δ, called the horizon, that is assumed to determine the interacting spatial range between the material point at $\mathbf{x}$ and the material point at $\mathbf{x}'$ such that

$$\mathbf{f}(\boldsymbol{\eta}, \boldsymbol{\xi}) = 0 \quad \forall \boldsymbol{\eta}, \quad \text{if } \|\boldsymbol{\xi}\| > \delta \tag{5.5}$$

Note that $\boldsymbol{\eta} + \boldsymbol{\xi}$ shows the current relative position vector connecting the particles. The direct physical interaction through the particles at $\mathbf{x}$ and $\mathbf{x}'$ is called a *bond*. The bonds for any given particle do not extend over the horizon, δ. This means, particles only interact inside the horizon. The pairwise force vector $\mathbf{f}$ has the direction of $\boldsymbol{\eta} + \boldsymbol{\xi}$, which connects the material point at $\mathbf{x}$ to the material point at $\mathbf{x}'$ in the deformed body, as

$$\mathbf{f}(\boldsymbol{\eta}, \boldsymbol{\xi}) = f(\boldsymbol{\eta}, \boldsymbol{\xi}) \frac{\boldsymbol{\eta} + \boldsymbol{\xi}}{\|\boldsymbol{\eta} + \boldsymbol{\xi}\|} \tag{5.6}$$

where f is a scalar-valued pairwise force function, and $\|.\|$ is the Euclidean norm. The force vector $\mathbf{f}$ has following properties [117]:

$$\mathbf{f}(-\boldsymbol{\eta}, -\boldsymbol{\xi}) = -\mathbf{f}(\boldsymbol{\eta}, \boldsymbol{\xi}) \quad \forall \boldsymbol{\eta}, \boldsymbol{\xi} \tag{5.7}$$

The first property describes the balance of linear momentum, and the other property

arises from the balance of angular momentum:

$$(\boldsymbol{\eta} + \boldsymbol{\xi}) \times \mathbf{f}(\boldsymbol{\eta}, \boldsymbol{\xi}) = \mathbf{0} \tag{5.8}$$

The balance of angular momentum is satisfied by the sum of force couples which produces zero moment [130]. For the material point at $\mathbf{x}'$ within the horizon of the material point at $\mathbf{x}$, the scalar-valued pairwise force function is derived as

$$f(\boldsymbol{\eta} + \boldsymbol{\xi}) = c \times s(t, \boldsymbol{\eta}, \boldsymbol{\xi}) \tag{5.9}$$

where c is the micromodulus, and s is the bond stretch which possesses a similar concept of the strain in elasticity. The bond stretch s is defined as

$$s(t, \boldsymbol{\eta}, \boldsymbol{\xi}) = \frac{\|\boldsymbol{\eta} + \boldsymbol{\xi}\| - \|\boldsymbol{\xi}\|}{\|\boldsymbol{\xi}\|} \tag{5.10}$$

here $\|\boldsymbol{\xi}\|$ is the original bond length in the reference configuration, and $\|\boldsymbol{\eta} + \boldsymbol{\xi}\|$ is the bond length at current configuration. If the bond stretch $s = 0$, it means there is no pairwise force f between material points. In order to evaluate the interactive forces between material points and to solve peridynamic equation of motion, the material domain is discretized with a number of equally spaced nodes as shown in Fig. 5.2. The distance between two adjacent nodes is Δx in $x-$, $y-$, and $z-$directions. All nodes have the same volume $(\Delta x)^3$.

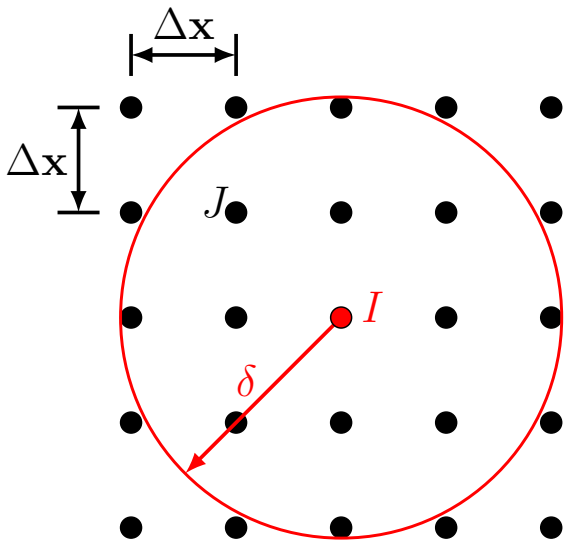

Fig. 5.2: Discretized domain for computation.

For a node which has an intersection with the horizon boundary as illustrated in Fig. 5.3, a volume reduction scheme is introduced as [137]

$$V_J(\|\boldsymbol{\xi}\|) = \begin{cases} \left(\frac{\delta - \|\boldsymbol{\xi}\|}{2r_j} + \frac{1}{2}\right) V_J & \text{if } (\delta - r_j) \leq \|\boldsymbol{\xi}\| \leq \delta \\ V_J & \text{if } \|\boldsymbol{\xi}\| \leq (\delta - r_j) \\ 0 & \text{otherwise} \end{cases} \tag{5.11}$$

where $(\delta - r_j)$ is the distance from which the volume is reduced, and r_j is chosen to be half of the grid spacing Δx in numerical implementations.

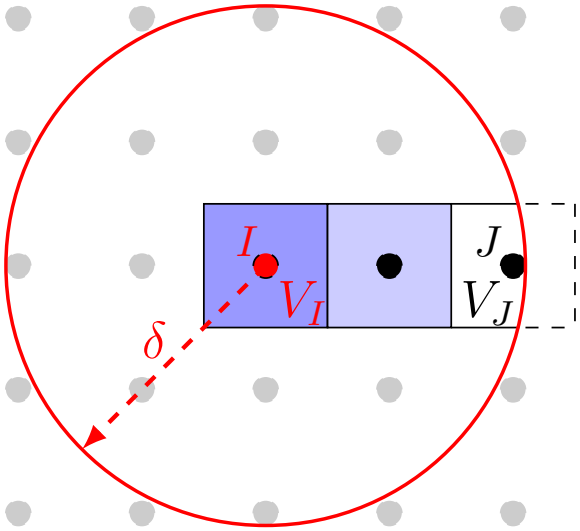

Fig. 5.3: Volume calculation scheme for discretized peridynamics. The volume is reduced on the boundary of a horizon.

To find the volume lumped for other particles inside a domain, in which the particles are arbitrarily placed, Voronoi tessellation can be used in this study. Detailed discussion on Voronoi tessellation and topology optimization is presented in the next chapter.

5.3.2 Micromodulus of elastic materials

A peridynamic material is considered to be microelastic if the bond force is defined as [117, 138, 139]

$$\mathbf{f}(\boldsymbol{\eta}, \boldsymbol{\xi}) = \frac{\partial w}{\partial \boldsymbol{\eta}}(\boldsymbol{\eta}, \boldsymbol{\xi}) \qquad \forall \boldsymbol{\eta}, \boldsymbol{\xi} \tag{5.12}$$

where w is the micropotential which is the energy in a single bond and has dimensions of energy per unit volume squared. Setting the strain energies of peridynamics and classical linear elasticity identical, the constant micromodulus $\tilde{c}_1$ for one-dimensional peridynamics is obtained as [140]

$$\tilde{c}_1 = \frac{2E}{A\delta^2} \tag{5.13}$$

where A is the cross-sectional area, and $\tilde{c}_3$ for three-dimensional models is [141]

$$\tilde{c}_3 = \frac{18k}{\pi\delta^4} \tag{5.14}$$

where k is the material bulk modulus. In the derivation, the Poisson's ratio ν is a fixed value of 1/4. It should be noted that Numerous researches have been conducted in peridynamics so that various Poisson's ratios can be applied.

5.3.3 Numerical implementation of peridynamics

In this section, a summary of the numerical approximation to the peridynamic equations is presented. It should be noted that the linearized version of the peridynamic theory is applied to a homogeneous body here. At first, the discretized form of the Eq. 5.2 replaces the integral by a finite sum

$$\rho\ddot{\mathbf{u}}_i^n = \sum_p \mathbf{f}(\boldsymbol{\eta}, \boldsymbol{\xi})V_p + \mathbf{b}_i^n \tag{5.15}$$

By applying Eqs. 5.3 and 5.4 into Eq. 5.15, the equation becomes as

$$\rho\ddot{\mathbf{u}}_i^n = \sum_p \mathbf{f}(\mathbf{u}_p^n - \mathbf{u}_i^n, \mathbf{x}_p - \mathbf{x}_i)V_p + \mathbf{b}_i^n \tag{5.16}$$

where V_p is the volume of node p, which can be obtained from Voronoi tessellation method. For a uniform rectangle grid, which is mostly discussed here, it is simply Δx^3. The sum is taken over all nodes inside the horizon such that $\mathbf{x}_p - \mathbf{x}_i < \delta$. n is the number of time step, and the subscription denotes the node number as

$$\mathbf{u}_i^n = \mathbf{u}(\mathbf{x}_i, t^n) \tag{5.17}$$

The discretized form of the linearized peridynamic model can be written as

$$\rho\ddot{\mathbf{u}}_i^n = \sum_p \mathbf{C}(\mathbf{x}_p - \mathbf{x}_i)(\mathbf{u}_p^n - \mathbf{u}_i^n)V_p + \mathbf{b}_i^n \tag{5.18}$$

where $\mathbf{C}$ is called micromodulus. The micromodulus was described in previous section, and it is a tensor function defined as

$$\mathbf{C}(\boldsymbol{\xi}) = \frac{\partial \mathbf{f}}{\partial \boldsymbol{\eta}}(0, \boldsymbol{\xi}) \qquad \forall \boldsymbol{\xi} \tag{5.19}$$

Consequently, the pairwise force in the linearized theory is driven by $\mathbf{f} = \mathbf{C}(\boldsymbol{\xi})\boldsymbol{\eta}$. An explicit central difference formula is employed for acceleration in Eq. 5.18

$$\rho\ddot{\mathbf{u}}_i^n = \frac{\mathbf{u}_i^{n+1} - 2\mathbf{u}_i^n + \mathbf{u}_i^{n-1}}{\Delta t^2} \tag{5.20}$$

An stable time step for Eq. 5.18 based on von Neumann stability analysis [142] can be obtained as

$$\Delta t < \sqrt{\frac{2\rho}{\sum_p V_p \mid \mathbf{C}(\mathbf{x}_p - \mathbf{x}_i) \mid}} \tag{5.21}$$

In practice, for macroscale modeling, the value $\delta = 3\Delta x$ most of the time works well [139]. Values much smaller than $3\Delta x$ typically result in undesirable grid effects such as cracks grow along the rows or columns of the grid and values much larger than

this may result in excessive wave dispersion and require very large CPU times.
Boundary conditions applied in the peridynamic method are different than in the FE method. As described in [117], the variational formulation in this approach does not lead to natural boundary conditions. To resolve this problem, forces at the surface of a body are applied as body forces **b** within some layers under the surface.

5.4 Fatigue model

A peridynamic fatigue model has been proposed by Oterkus et. al [143] to predict the growth phase of a crack but not the nucleation phase. Their model was developed within the bond-based peridynamic theory, in which the force density in each bond is independent of the other bonds. In this method, the critical bond strain for breakage in each bond over time was degraded, according to the prevailing cyclic loading in the bond, and it accounts for permanent strain in the bonds.
In addition, Silling and Askari [8] presented a peridynamic damage model that did not explicitly involve a critical bond strain for damage. Instead, they introduced a damage variable called the "remaining life" in each bond that evolves over time, as described below. Their model is not limited to bond-based material models, and it applies to both the crack initiation and propagation phases (by using different choices of the parameters).
To introduce the peridynamic damage model, a peridynamic solid is considered to be subject to cyclic loading between two extremes, denoted max and min. $\mathbf{x}$ is a

point in the body. For a given bond $\boldsymbol{\xi}$ in the family of $\mathbf{x}$, the bond strains at the two extremes then can be defined as

$$s^{max} = \frac{|\underline{\mathbf{Y}}^{max}\langle\boldsymbol{\xi}\rangle| - |\boldsymbol{\xi}|}{|\boldsymbol{\xi}|}, \qquad s^{min} = \frac{|\underline{\mathbf{Y}}^{min}\langle\boldsymbol{\xi}\rangle| - |\boldsymbol{\xi}|}{|\boldsymbol{\xi}|}, \tag{5.22}$$

which means the change in bond length divided by the initial bond length. In this equation, the deformation state $\underline{\mathbf{Y}}$, whose value for any bond is the deformed image of the bond is defined as

$$\underline{\mathbf{Y}}\langle\mathbf{x}' - \mathbf{x}\rangle = \mathbf{y}(\mathbf{x}', t) - \mathbf{y}(\mathbf{x}, t) \tag{5.23}$$

The cyclic bond strain at $\boldsymbol{\xi}$ is defined by

$$\varepsilon = |s^{max} - s^{min}| \tag{5.24}$$

For a given $\mathbf{x}$ and $\boldsymbol{\xi}$, the quantities s^{max}, s^{min}, and ε can all depend on the number of cycles N. This is due to the evolution of fatigue damage and other material properties. When a fatigue crack grows closer to the bond, ε is expected to increase.

The peridynamic fatigue model presented by Silling et. al [8] identifies a remaining life $\lambda(\mathbf{x}, \boldsymbol{\xi}, N)$ for each bond $\boldsymbol{\xi}$ connected to any point $\mathbf{x}$. . The remaining life develops gradually as the loading cycle N increases based on the following relation:

$$\lambda(0) = 1, \qquad \frac{d\lambda}{dN}(N) = -A\varepsilon^m \tag{5.25}$$

where ε is the current cyclic strain in the bond, A is a positive parameter and m is a positive constant exponent. The bond breaks irreversibly at the earliest loading cycle N if the following criteria satisfies:

$$\lambda(N) \leq 0 \tag{5.26}$$

According to whether a bond is in the initiation or propagation phase, the values of A and m are chosen differently as described in the following sections.

5.4.1 Crack initiation and propagation

Before a fatigue crack occurs, each bond $\boldsymbol{\xi}$ is in the crack initiation phase of the fatigue process. In this case, the parameters A and m in Eq. 5.25 are set to [8]

$$A = A_1, \qquad m = m_1 \tag{5.27}$$

where A_1 and m_1 are positive constants that are calibrated for the crack initiation phase in a material as described below.

Each bond in the body experiences a cyclic strain $\varepsilon(\mathbf{x}, \boldsymbol{\xi})$. In order to calibrate A_1 and m_1 with experimental data, it is assumed that the cyclic strain in each bond is independent of number of cycles N. Considering the bond $\boldsymbol{\xi}_1$ connected to a point $\mathbf{x}_1$ such that this bond has the largest cyclic bond strain in the model, its cyclic bond strain is named as ε_1. Since A_1 and m_1 are independent of position and $m_1 > 0$, the bond $\boldsymbol{\xi}_1$ is the bond at which damage will first initiate. $\lambda_1(N)$ denotes the remaining life of the corresponding bond, and $\lambda_1(0) = 1$ based on Eq. 5.25. By computing the cycle N_1 at which the bond breaks and integrating the second of Eq. 5.25 over number of cycles N, it can be obtained that

$$A_1 \varepsilon_1^{m_1} N_1 = 1 \tag{5.28}$$

Consequently, the crack initiation will occur if

$$N_1 = \frac{1}{A_1 \varepsilon_1^{m_1}} \tag{5.29}$$

The parameters A_1 and m_1 can be obtained from S-N test data for a material as depicted in Fig. 5.4 [8].

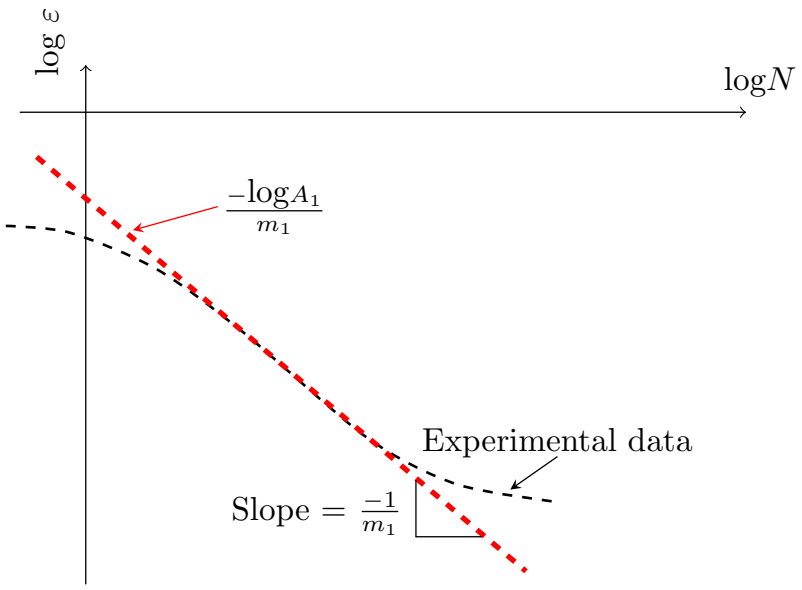

Fig. 5.4: Determination of A_1 and m_1 from E-N curve [8].

Once the initial crack location and the corresponding fatigue life are calculated, the bond with the minimum fatigue cycles is broken. In the model of a broken bond, its elastic modulus is decreased to a very small number. Then, the simulation keeps continuing to the next step until the crack growth path is identified. In this approach, which leads to progressive failure, the breakage of one bond in the model tends to increase the elongation of neighboring bonds. Therefore, it is more likely

that the neighboring bonds will be broken in next steps. This failure tends to organize itself into two-dimensional surfaces that represent cracks and bonds in many different directions contribute to crack propagation, as well as bonds that are normal to the crack surface (Fig. 5.5). Crack initiation and propagation occur spontaneously and autonomously, that is, without reference to any supplemental equations dictating these phenomena.

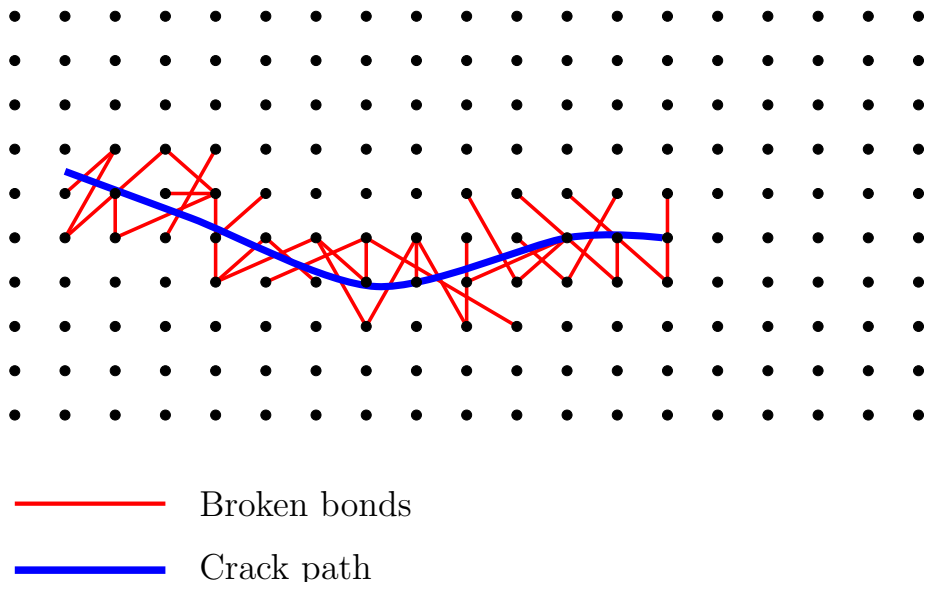

Fig. 5.5: Crack propagation trajectory in a peridynamic model predicted by damage in bonds

5.5 Tension test for a two dimensional case

In this case, a two-dimensional plate with a central crack subjected to a uniaxial tension is studied. The length of the plate is 40 *cm* and the width is 20 *cm*.

Young's modulus, E, is 70 GPa and the density is $\rho = 2700\ kg/m^3$. The model is shown in Fig. 5.6 and based on Macek and Silling comment [139], δ is chosen to be equal to $3\Delta x$. It should be noted that undesirable grid effects such as cracks growing along the rows or columns of the grid may occur if δ is much smaller than this value, and larger vaules may may result in excessive wave dispersion and require very large CPU run times.

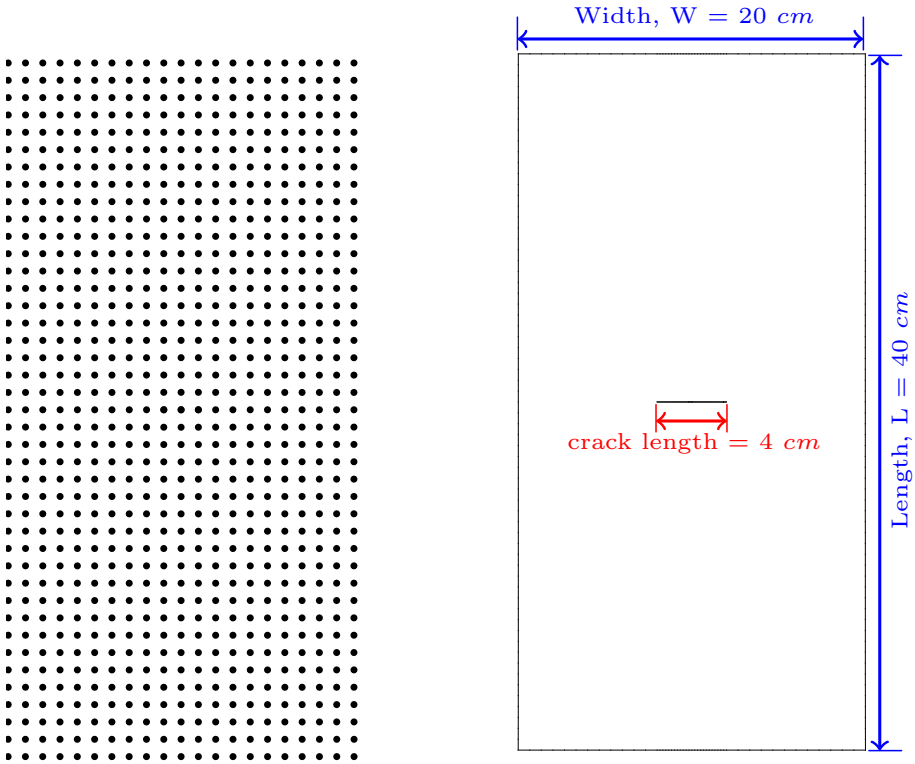

Fig. 5.6: Schematic view of two dimensional model with a crack, and particle distributions

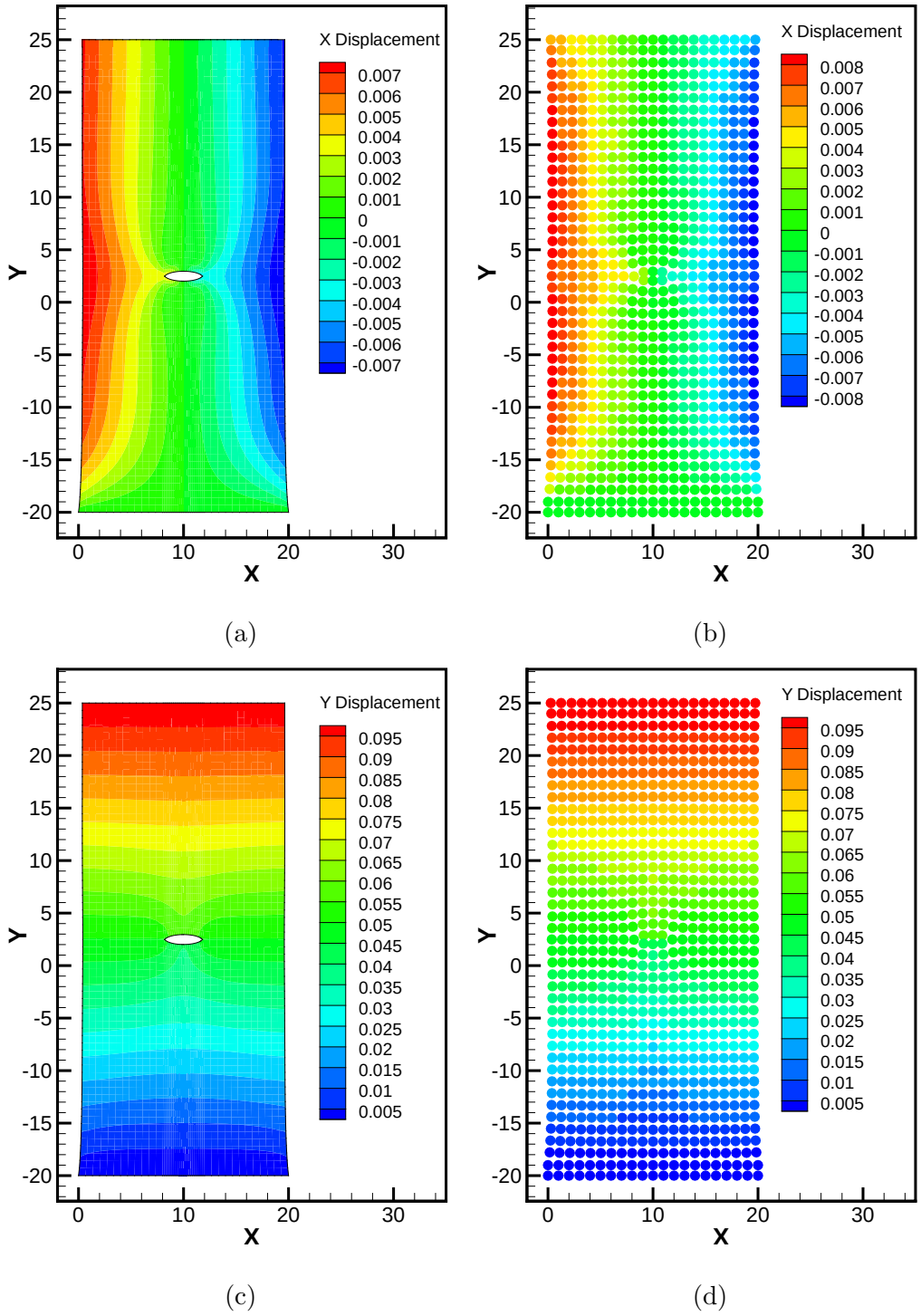

Fig. 5.7: (a) U_x using finite elment method; (b) U_x using peridynamics method; (c) U_y using finite elment method; (d) U_y using peridynamics method.

The displacement fields obtained by peridynamics are compared with the finite element analysis results in Fig. 5.7 and as the figure indicates they are in good agreement.

5.6 Rolling contact fatigue

Subsurface originated spalling has been known as one of the main modes of failure for rolling contact fatigue (RCF) of bearings. A significant number of investigators have attempted to determine the physical mechanisms involved in rolling contact fatigue of bearings and proposed models to predict their fatigue lives [18, 19, 21, 144–146].

Very few models from previous studies relate the micro-mechanical material behavior to the phenomenon of rolling contact fatigue. At first, fatigue cracks appear as micro-cracks at weak material points, and the crack initiation mechanism is influenced by the microscopic characteristics of the material. Hence, the models developed based on a macro-scale description of the material lead to overlook the microscopic details. RCF lives of bearings are known to show scatter because of the spatial dispersion in material strengths and inclusion distributions. The occurrence of crack initiation is finding at the weakest point in the material where the local strength is a minimum. Nevertheless, the analytical models are deterministic in nature and hence do not take this into account.

In view of the limitations of the current state of bearing life modeling, a new ap-

proach, for predicting the fatigue lives of the rolling element bearings, is developed in this study, based on the fatigue model of peridynamics. The proposed approach offers several advantages over existing research models for RCF life. First, it can easily predict fatigue crack initiation and propagation without mesh treatment. Unlike the previous crack propagation approaches where some initial crack geometry and location are assumed, the present approach does not require the presence of initial cracks or flaws in the material domain. In fact, cracks can be naturally initiated under the contact loading and can continue to grow if the stress conditions permit. Secondly, non-homogeneous description of the material can be modeled using this approach. In this regard, it can easily incorporate the effects of material inclusions in the studies of bearing contacts. Finally, the model has the potential to offer more insight into the physical mechanism of the failure process occurring during RCF.

In this study one example is carried over using Peridynamics in order to predict the fatigue crack initiation life and the crack initiation location. The results will be compared with the ones from finite element analysis. Then by using the progressive damage model that presented in previous section, the crack propagation path will be determined.

Fig. 5.8 shows a rolling contact model and the area of interest in which the fatigue lives are calculated. The structure is under Hertzian pressure and the load is moving from one side to another in one cycle.

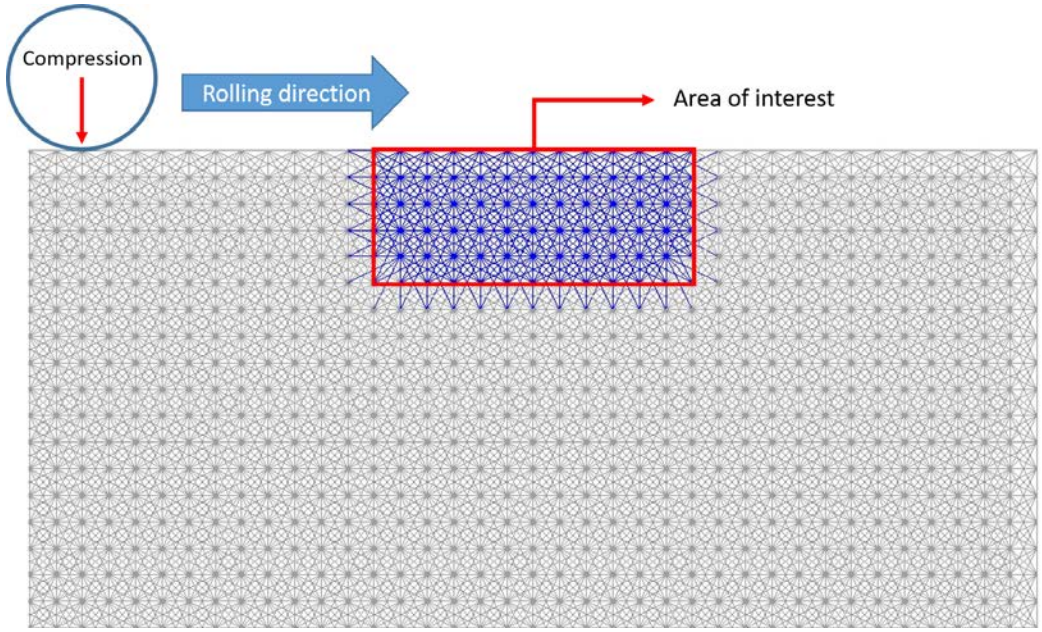

Fig. 5.8: Shematic peridynamic model (bonds) and cyclic Hertzian contact load through analytical rigid body on the surface.

Before computing fatigue life, the total displacement fields using Peridynamics and finite element approaches are compared. Fig. 5.9 indicates good agreement between Peridynamic's results and finite element approach at three different time steps.

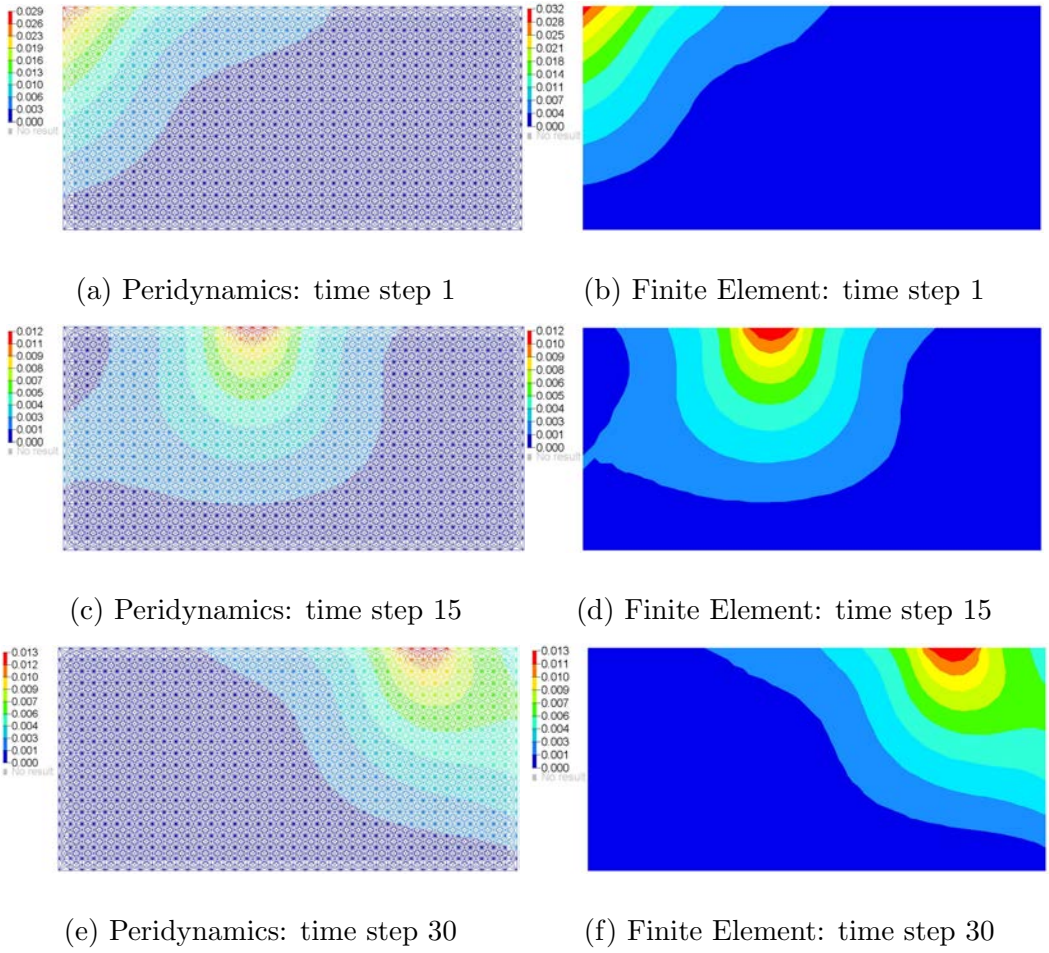

(a) Peridynamics: time step 1 (b) Finite Element: time step 1

(c) Peridynamics: time step 15 (d) Finite Element: time step 15

(e) Peridynamics: time step 30 (f) Finite Element: time step 30

Fig. 5.9: Total displacement; (a,c,e) Perdidynamics; (b,d,f) Finite Element Anlysis.

For the purpose of verification, the same geometry with the same number of nodes were used in FE model. Based on the Peridynamics results and FE simulation the crack initiation will occur at 5500 and 6000 cycles respectively. This is shown in Fig. 5.10(a) and Fig. 5.10(b) and it also demonstrates that the fatigue crack will initiate near the surface in both approaches. Once the first bond with the lowest fatigue life is identified, its mechanical properties are decreased to model a broken bond in

order to simulate the fatigue crack propagation which is depicted in Fig. 5.10(c) - 5.10(e). It shows that the crack starts propagation from a location with which has more broken bonds around and it propagates to the other side of the bearing.

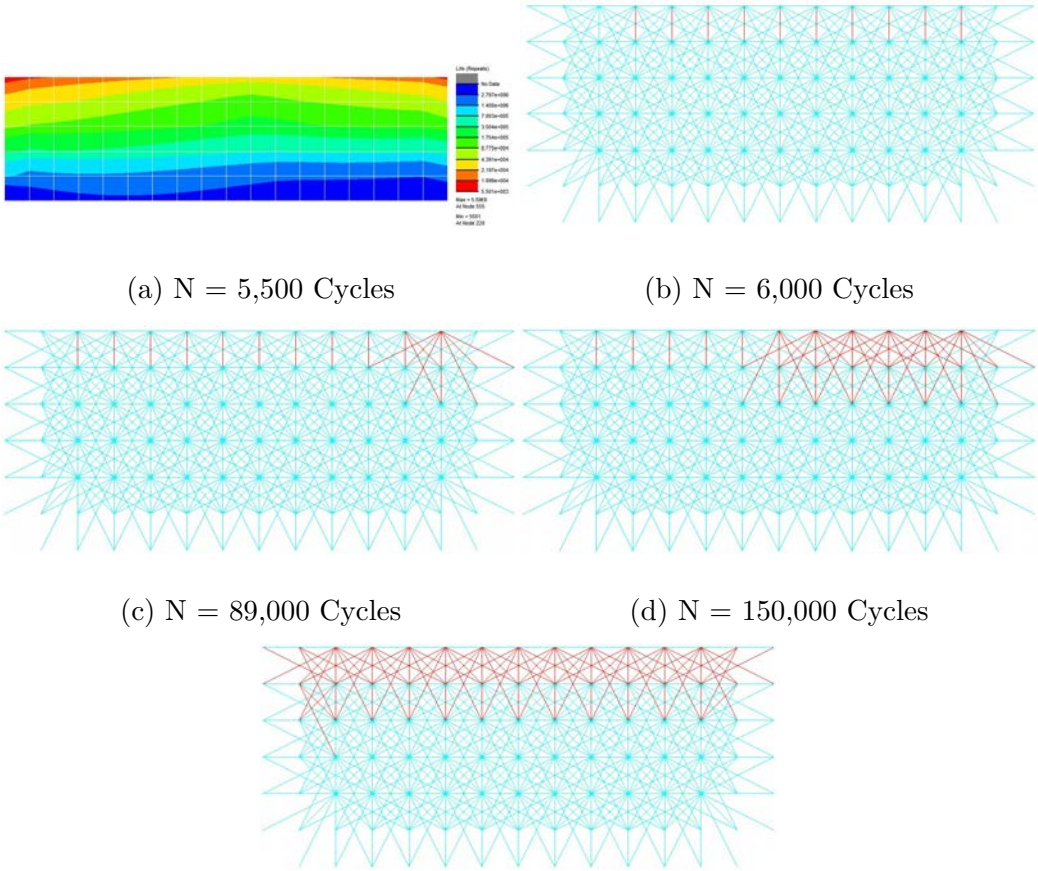

(a) N = 5,500 Cycles

(b) N = 6,000 Cycles

(c) N = 89,000 Cycles

(d) N = 150,000 Cycles

(e) N = 350,000 Cycles

Fig. 5.10: Fatigue crack initiation and propagation lives and locations; (a) FE analysis for fatigue crack initiation; (b) Peridynamics result for crack initiation; (c)-(e) crack propagation using Peridynamics approach.

5.6.1 Another approach for crack propagation using initial cracks

There is another approach to simulate fatigue crack propagation using peridynamics [8], and it was not used but only describeded in this section. In this approach, there should be an initial crack in order to perform crack propagation analysis.

To apply the peridynamic model to predict fatigue crack propagation, Eq. 5.25 with a proper choice of parameters A_2 and m_2 needs to be applied to bonds within the horizon, δ, of the material point on a pre-existing crack tip. A bond $\boldsymbol{\xi}$ normal to the axis of a growing mode-I fatigue crack is considered to calibrate A_2 and m_2 for the material,(Fig. 5.11).

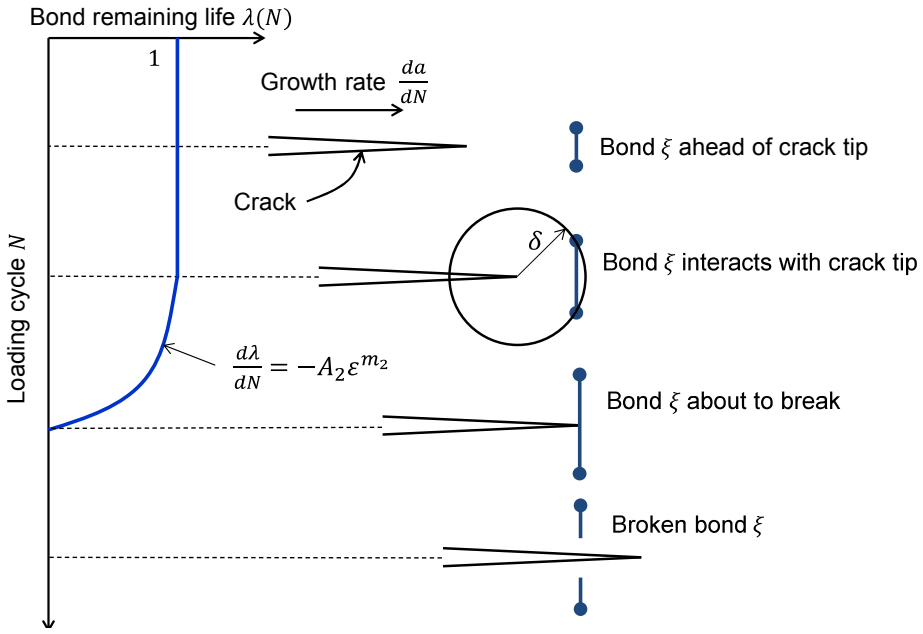

Fig. 5.11: A bond $\boldsymbol{\xi}$ near an approaching fatigue crack under the cyclic strain ε, which changes over time, eventually causing the bond to break. [8]

Two assumptions are made in this step. The first assumption is that the deformation near the crack tip is constant in the frame of reference of the crack tip, and the second one is that the crack propagates through a constant distance da/dN in every loading cycle. It follows that the cyclic strain and the remaining life of this bond $\boldsymbol{\xi}$ as

$$\varepsilon(N) = \bar{\varepsilon}(z), \qquad \lambda(N) = \bar{\lambda}(z) \tag{5.30}$$

At the core bond, the remaining life disappears since this bond is on the verge of breakage:

$$\bar{\lambda}(0) = 0 \tag{5.31}$$

Hence, a relation between the crack growth rate and the core cyclic bond strain can be obtained as

$$\frac{da}{dN} = C\varepsilon_{core}^{m_2} \tag{5.32}$$

By recalling the well-known Paris law from Chapter 2 for fatigue crack growth:

$$\frac{da}{dN} = c\Delta K^M \tag{5.33}$$

where c and M are Paris constants. Comparing Eq. 5.32 with Eq. 5.33 leads to the conclusion that the exponents are the same in both expressions as

$$m_2 = M \tag{5.34}$$

In other words, the parameter m_2 can be obtained directly from Paris law data for a material based on a plot of $\log(da/dN)$ versus $\log(\Delta K)$.

In addition, the calibrated value for A_2 in the peridynamic model is given by [8]

$$A_2 = A' \frac{da/dN}{(da/dN)'} \tag{5.35}$$

If the loading is less than the fatigue limit on the S-N curve, there will be no fatigue damage occurring and accumulating. To incorporate such a fatigue limit into the peridynamic fatigue model, the fatigue crack initiation phase in Eq. 5.25 is modified as follows [8]:

$$\lambda(0) = 1, \qquad \frac{d\lambda}{dN}(N) = \begin{cases} -A_1(\varepsilon - \varepsilon_\infty)^{m_1}, & \text{if } \varepsilon > \varepsilon_\infty \\ 0 & \text{otherwise} \end{cases} \tag{5.36}$$

where ε_∞ is the lowest cyclic bond strain results in damage over a very large number of load cycles. Fig. 5.12 indicates a comparison of an S-N curve predicted by the peridynamic model with a fatigue limit and without the limit versus test data.

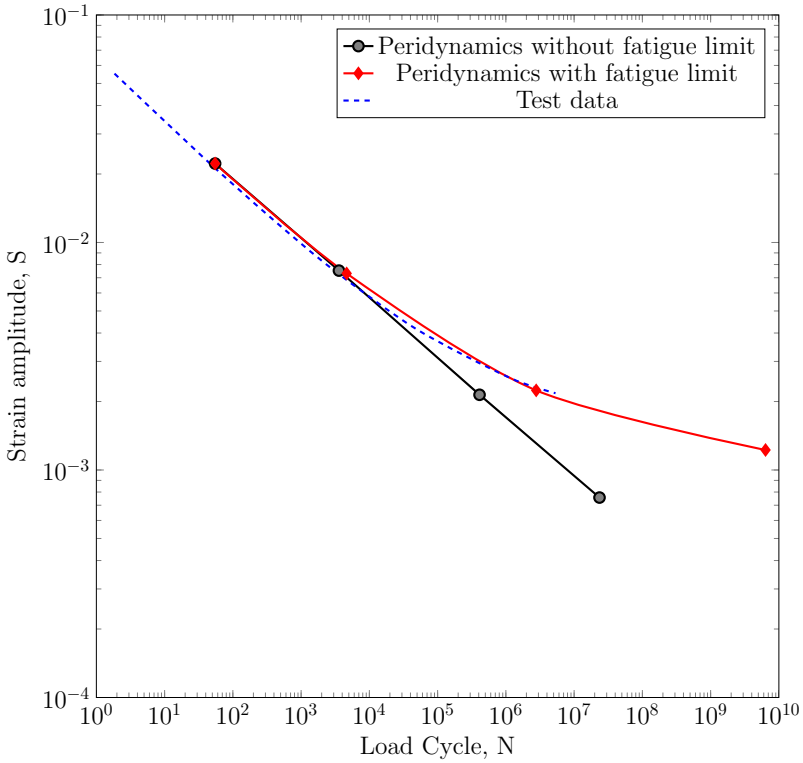

Fig. 5.12: Strain amplitude as a function of loading cycle at which crack initiation occurs in the hourglass test specimen. Model results are shown with and without a fatigue limit [8]

5.7 Conclusion and scope

In this chapter the peridynamics method was presented to simulate fatigue crack initiation and propagation of mechanical structures. The theory was explained and adapted to simulate rolling contact fatigue.

The current work is carrying out the peridynamics to predict rolling contact fatigue (RCF). Research in this study was made in following areas:

- Conducting a damage based rolling contact fatigue calculation using peridy-

namics to study the process of subsurface initiated spalling in bearing contacts

- Developing a model which takes into account the gradual material degradation occurring under contact cycling through an empirical damage evolution equation
- Incorporating three phases of spall formation (microcrack initiation, crack coalescence, and propagation) in a unified framework that explicitly takes the effect of material microstructure into account
- Eventually, studying the Multi-scale results and making conclusions for the procedure.

CHAPTER 6
CONCLUSIONS AND FUTURE WORKS

In this chapter, the conclusions of the thesis and the future recommendations are presented. Section 7.1 presents conclusions about the proposed multiscale method for fatigue analysis of rolling contact systems as well as alternate continuum methods for fatigue analysis. Future recommendations are provided in Section 7.2.

6.1 Conclusions

In this thesis, a hierarchical multiscale method was proposed to study rolling contact fatigue phenomena and to predict fatigue lives. This multiscale framework contains the molecular model of lubricant and the continuum model of rolling contact components. The calculated friction coefficient was passed from the molecular model to the continuum model. Therefore, this one-way message passing categorizes the developed multiscale method in the hierarchical or sequential multiscale family.

In the molecular model, MD simulations of thin film lubrication and lubricated contact surfaces were carried out to investigate hydrodynamic lubrication at nano-scale. In this molecular model, solid walls were modeled by the Finnis-Sinclair (FS) EAM potentials, and the united atoms including CH_3 and CH_2 were considered for the lubricant alkane chains. Various chain lengths were considered to study the effect of molecular chain length on the mechanisms of lubrication as well as the friction between contact surfaces. It was observed that when two contact surfaces approached each other, the thin film thickness presented a step-like behavior because the num-

ber of layers varied with the amount of lubricant chains although the total number of molecules kept same. It was also shown that as the chain length increased, the thin film thickness reduced. However, the velocity profile didn't change significantly. In addition, a longer chain length also resulted in higher shear stresses in thin film lubrication. Only the chain length of eight was considered in the molecular model of lubricant to calculate the coefficient of friction, which will be passed to the macro-scale in order to calculate rolling contact fatigue.

In addition, the effects of one nano-particle (debris) and temperature on mechanical behaviors of thin film lubrication in were studied. The material of the nano-particle was chosen as the same as the wall material (Fe) and it was big enough to have contact with two solid wall surfaces. Based on the results in this thesis, due to the presence of a nano-particle the coefficient of friction would be increased by %40. When various temperatures were considered, it was found that the friction coefficient was smaller at a higher temperature.

Then by passing the coefficient of friction to the continuum model at the macro scale, rolling contact fatigue analysis was carried out using the finite element analysis. A finite element model was developed and employed to study rolling contact fatigue and predict fatigue life of bearing. The fluctuating load was also considered, and the fatigue life was significantly reduced. The intention to study the fatigue of mechanical systems under random loads was raised from considering the effects of wind speed and direction on bearings and gear-teeth in wind turbine gearboxes.

In addition, three-dimensional finite element analyses were presented to study both

fatigue crack initiation and fatigue crack propagation in a gear tooth. Linear elastic fracture mechanics approach was employed here to model mixed-mode fatigue crack propagation in a gear tooth after a fatigue crack was initiated. Two various load conditions were considered: the contact load acting along the whole face width and the one acting along the partial face width of gear tooth. Those two load conditions resulted in different crack trajectories, stress intensity factors and fatigue crack propagation lives. In addition, it was shown that Boron/Epoxy patches would enhance the fatigue crack propagation life of the gear tooth.

In this thesis, Peridynamics was studied as alternate approache in the continuum model of the proposed multiscale method. It has the advantages to model and simulate discontinuities over the conventional finite element methods. The Peridynamics method was presented first to simulate fatigue crack initiation and propagation of mechanical structures. The theory was explained and adapted to simulate rolling contact fatigue phenomena and to predict fatigue lives. It was shown that using Peridynamics, the results were in good agreement with finite element method and it has the ability to predict crack propagation by reducing the bonds mechanical properties (progressive damage).

6.2 Future work

The current work is developing a multiscale framework to study rolling contact fatigue. The multiscale model include a molecular model of lubricant and a continuum

model of rolling contact components. Future works can be done in each model.

The molecular model in this thesis provides an enlightened view on the mechanism of hydrodynamics lubrication at nano-scale. There are many future studies that could be explored with the current models to gain a better understanding of friction and lubrication, including:

- Metal oxide surfaces can be considered to replace the current iron surfaces (i.e., Fe2O3), and the liquid-solid interaction should be described by a more advanced potential which enables the simulation to explore the physical and chemical interactions (i.e., ReaxFF [147, 148]).
- A limited range of operating conditions in this work were considered and a wider range of conditions (sliding speed, normal load, and different types and sizes of nano particles with different materials) could be investigated in the future.
- Rough surfaces with multiple and random asperities can also be considered with further studies and statistical analyses.
- nanoparticles with various materials and sizes can be considered to study their effects on the friction force between contact surfaces.

There are more further researches can be done in the future with the continuum model of rolling contact components:

- Conducting a damage based rolling contact fatigue calculation using peridynamics to study the process of subsurface initiated spalling in bearing contacts
- Developing a model which takes into account the gradual material degradation occurring under cycling contact through an empirical damage evolution equation

- Incorporating three phases of spall formation (microcrack initiation, crack coalescence, and propagation) in a unified framework that explicitly takes the effect of material microstructure into account
- Studying the effect of nonhomogeneous materials and defects on rolling contact fatigue
- Conducting a statistical analysis on rolling contact fatigue

Finally, to study roller contact bearings using peridynamics, Weibull distribution can be considered. Rolling contact fatigue lives of bearings are known to show scatter because of the spatial dispersion in material strengths and inclusion distributions. In fact, it has been observed in experiments that bearing lives followed the Weibull distribution closely.

REFERENCES

[1] B. Boardman. Crack Initiation Fatigue - Data, Analysis, Trends and Estimation. *SAE Technical Paper 820682*, 1982.

[2] B. Lou, L. Han, Z. Lu, S. Liu, and F. Shen. The rolling contact fatigue behaviors in carburized and hardened steel. *In Fatigue 90, (Ed. H. Kitagawa and T. Tanaka) Proceedings of the Fourth International Conference on Fatigue and Fatigue Thresholds, Honolulu, Hawaii*, pages 627–632, 1990.

[3] D. Nelias, M.L. Dumont, F. Champiot, A. Vincent, D. Girodin, R. Fougeres, and L. Flamand. Role of inclusions, surface roughness and operating conditions on rolling contact fatigue. *Journal of Tribology*, 121:240–251, 1999.

[4] H. Hosseini-Toudeshky, B. Mohammadi, and S. Bakhshandeh. Crack trajectory analysis of single-side repaired thin panels in mixed-mode conditions using glass/epoxy patches. *Computers and Structures*, 86:997–1005, 2008.

[5] H. Hosseini-Toudeshky and B. Mohammadi. Thermal residual stresses effects on fatigue crack growth of repaired panels bounded with various composite materials. *Computers and Structures*, 89:216–223, 2009.

[6] S. Pehan, J. Kramberger, J. Flas, and B. Zafosnik. Investigation of crack propagation scatter in a gear tooths root. *Engng Fract Mech.*, 75:1266–1283, 2008.

[7] H. Hosseini-Toudeshky, M.A. Ghaffari, and B. Mohammadi. Finite element fatigue propagation of induced cracks by stiffeners in repaired panels with composite patches. *Comp. Struct.*, 94:1771–1780, 2012.

[8] S. A. Silling and A. Askari. *Peridynamic Model for Fatigue Cracking.* A user guide. Technical report, SAND2014-18590, Sandia National Laboratories, 2014.

[9] W.E. Littmann. The mechanism of contact fatigue. *In Interdisciplinary Approach to the Lubrication of Concentrated Contacts, (Ed. P.M. Ku) Proceedings of a Symposium, Troy, NY, NASA Special Report, SP-237*, pages 309–378, 1969.

[10] A.F. Bower. The influence of crack face friction and trapped fluid on surface initiated rolling contact fatigue cracks. *Journal of Tribology*, 110:704–711, 1988.

[11] D. Dowson. *History of tribology.* London, Longman, 1979.

[12] F.P. Bowden and D. Tabor. *The friction and lubrication of solids.* Oxford, Oxford University Press, 1954.

[13] J.N. Israelachvili. Strength of van der waals attraction between liqid bilayers. *Journal of Tribology*, 10:3369–3370, 1994.

[14] H. Yoshizawa, Y.L. Chen, and J. Israelachvili. Recent advances in molecular level understanding of adhesion, friction and lubrication. *Wear*, 168:161–166, 1993.

[15] J. Krim, D.H. Solina, and R. Chiarello. Nanotribology of a krypton monolayer: a quartz-crystal microbalance study of atomic-scale friction. *Phys. Rev. Lett.*, 66:181–184, 1991.

[16] O. Raynolds. On the theory of lubrication and its application to mr beauchamp towers experiments, including an experimental determination of the viscosity of olive oil. *Phil. Trans. R. Soc.*, 117:157–234, 1886.

[17] D. Dowson and G.R. Higginson. A numerical solution to the elastohydrodynamic problem. *J. Mech. Eng. Sci.*, 1:6–15, 1959.

[18] F. Sadeghi, B. Jalalahmadi, T. S. Slack, N. Raje, and N. K. Arakere. A review of rolling contact fatigue. *Journal of tribology*, 131:041403, 2009.

[19] G. Lundberg and A. Palmgren. Dynamic Capacity of Rolling Bearings. *Acta Polytech. Scand., Mech. Eng. Ser.*, 1:1–52, 1947.

[20] G. Lundberg and A. Palmgren. Dynamic capacity of roller bearings. *Acta Polytech. Scand., Mech. Eng. Ser.*, 2:96–127, 1952.

[21] E. Ioannides and T. A. Harris. New Fatigue Life Model for Rolling Bearings. *ASME J. Tribol.*, 107:367–378, 1985.

[22] T.E. Tallian. Simplified Contact Fatigue life prediction model - part II: new model. *ASME J. Tribology*, 114:214–222, 1992.

[23] I. I. Kudish and K. W. Burris. Modern state of experimentation and modeling in contact fatigue phenomenon: Part II - analysis of the existing statistical mathematical models of bearing and gear fatigue life. New statistical model of contact fatigue. *Tribology Transactions*, 43:293–201, 2000.

[24] L. M. Keer and M. D. Bryant. A pitting model for rolling contact fatigue. *ASME J. Lubr. Tech.*, 105:198–205, 1983.

[25] R. S. Zhou, H. S. Cheng, and T. Mura. Micropitting in rolling and sliding contact under mixed lubrication. *ASME J. Tribology*, 111:605–613, 1989.

[26] R. S. Zhou. Surface topography and failure life of rolling contact bearings. *Tribology Transactions*, 36:329–340, 1993.

[27] V. Bhargava, G. T. Hahn, and C. A. Rubin. Rolling contact deformation, etching effects and failure of high strength steels. *Metall. Trans. A*, 21:1921–1931, 1990.

[28] A. Vincent, G. Lormand, P. Lamagnere, L. Gosset, D. Girodin, G. Dudragne, and R. Fougeres. From white etching areas formed around inclusions to crack nucleation in bearing steels under rolling contact. *Bearing Steels: Into the 21st Century, ASTM STP No. 1327, J. Hoo and W. Green, eds., ASTM Special Technical Publication, West Conshohocken,*, pages 109–123, 1998.

[29] G. Xu and F. Sadeghi. Spall initiation and propagation due to debris denting. *Wear*, 201:106–116, 1996.

[30] G. Lormand, G. Meynaud, A. Vincent, G. Baudry, D. Girodin, and G. Dudragne. From cleanliness to rolling fatigue life of bearings - a new approach. *Bearing Steels: Into the 21st Century, ASTM STP No. 1327, J. Hoo and W. Green, eds., ASTM Special Technical Publication, West Conshohocken, PA.*, pages 55–69, 1998.

[31] B. Jalalahmadi and F. Sadeghi. A voronoi finite element study of fatigue life scatter in rolling contacts. *ASME J. Tribology*, 131:022203, 2009.

[32] N. N. Raje, F. Sadeghi, R. G. Jr. Rateick, and M. R. Hoeprich. A numerical model for life scatter in rolling element bearings. *ASME J. Tribology*, 130: 011011, 2008.

[33] B. Bhushan, J. N. Israelachvili, and U. Landman. Nanotribology: Friction, Wear and Lubrication at the Atomic Scale. *Nature*, 374:607–616, 1995.

[34] L. Zhang and H. Tanaka. Atomic Scale Deformation in Silicon Monocrystals Induced by Two-Body and Three-Body Contact Sliding. *Tribology International*, 31:425–433, 1998.

[35] P. Chantrenne, M. Raynaud, P. C. Clapp, J. Rifkin, and C. S. Becquart. Molecular Dynamics Simulations of Friction. *Heat and Technology*, 18:49–56, 2000.

[36] J. A. Harrison, R. J. Colton, C. T. Whit, and D. W. Brenner. Effect of Atomic-Scale Surface Roughness on Friction: A Molecular Dynamics Study of Diamond Surfaces. *Wear*, 168:127–133, 1993.

[37] X. Zheng, H. Zhun, A. K. Tieu, and B. Kosasih. A molecular dynamics simulation of 3D rough lubricated contact. *Tribology International*, 67:217–221, 2013.

[38] X. Zheng, H. Zhu, B. Kosash, and A.K. Tieu. A molecular dynamics simulation of boundary lubrication: The effect of n-alkanes chain length and normal load. *Wear*, 301:62–69, 2013.

[39] X. Zheng, H. Zhun, A. K. Tieu, and B. Kosasih. Roughness and Lubricant Effect on 3D Atomic Asperity Contact. *Tribol. Lett.*, 53:215–223, 2014.

[40] X. Zheng. Molecular dynamics simulation of boundary lubricant contacts. *PhD thesis*, 2014.

[41] X. Tao, Z. Jiazheng, and X. Kang. The ball-bearing effect of diamond nanoparticles as an oil additive. *Journal of Physics D: Applied Physics*, 29:2932, 1996.

[42] S. Tarasova, A. Kolubaeva, S. Belyaeva, M. Lernerb, and F. Tepperc. Study of friction reduction by nanocopper additives to motor oil. *Wear*, 252:63–69, 2002.

[43] H. Ghaedniaa, R. L. Jacksona, and Khodadadia J. M. Experimental analysis of stable CuO nanoparticle enhanced lubricants. *Journal of Experimental Nanoscience*, 10:1–18, 2015.

[44] M. Chhowalla and Amaratunga G. Thin films of fullerene-like MoS2 nanoparticles with ultra low friction and wear. *Nature*, 407:164–167, 2000.

[45] L. Rapoport, N. Fleisher, and R. Tenne. Applications of WS_2 (MoS_2) inorganic nanotubes and fullerene-like nanoparticles for solid lubrication and for structural nanocomposites. *Journal of Materials Chemistry*, 15:1782–1788, 2005.

[46] H. Ghaednia, H. Babaei, R.L. Jackson, M.J. Bozack, and J. M. Khodadadi. The effect of nanoparticles on thin film elasto-hydrodynamic lubrication. *Applied physics letters*, 103:263111, 2013.

[47] R. Rosentsveig, A. Gorodnev, N. Feuerstein, H. Friedman, A. Zak, N. Fleischer, J. Tannous, F. Dassenoy, and R. Tenne. Fullerene-like mos_2 nanoparticles and their tribological behavior. *Tribology Letters*, 36:175–182, 2009.

[48] D. Maharaj and B. Bhushan. Effect of mos_2 and ws_2 nanotubes on nanofriction and wear reduction in dry and liquid environments. *Tribology Letters*, 49:323–339, 2013.

[49] I.P. Omelyan, I.M. Mryglod, and Folk R. Optimized verlet-like algorithms for molecular dynamics simulations. *Phys. Rev. E*, 65:056706, 2002.

[50] S. Nose. unified formulation of the constant temperature molecular dynamics methods. *J. Chem. Phys.*, 81:511–519, 1984.

[51] W.G. Hoover. Canonical dynamics: equilibrium phase-space distributions. *Phys. Rev. A*, 31:1695–1697, 1985.

[52] N. Berro, H.and Fillot and P. Vergne. Molecular dynamics simulation of surface energy and zddp effects on friction in nano-scale lubricated contacts. *Tribol. Int.*, 43:1811–1822, 2010.

[53] D. Savio, N. Fillot, P. Vergne, and M. Zaccheddu. A model for wall slip prediction of confined n-alkanes: effect of wall-fluid interaction versus fluid resistance. *Tribol. Lett.*, 46:11–22, 2012.

[54] G. Spijker, P.and Anciaux and Molinari J.F. Dry sliding contact between rough surfaces at the atomistic scale. *Tribol. Lett.*, 44:279–285, 2011.

[55] M.G. Martin and J.I. Siepmann. Transferable potentials for phase equilibria. 1. united-atom description. *J. Phys. Chem.*, 1012:2569–2577, 1998.

[56] C.D. Wick, M.G. Martin, and J.I. Siepmann. Transferable potentials for phase equilibria. 4. united-atom description of linear and branched alkanes and of alkylbenzenes. *J. Phys. Chem.*, 104:8008–8016, 2000.

[57] J.M. Stubbs, J.J. Potoff, and J.I. Siepmann. Transferable potentials for phase equilibria. 6. united-atom description for ethers, glycols, ketones, and aldehydes. *J. Phys. Chem.*, 108:17596–17605, 2004.

[58] M.H. Ketko, J. Rafferty, J.I. Siepmann, and J.J. Potoff. Development of the trappe-ua force field for ethylene oxide. *Fluid Phase Equilibr.*, 274:44–49, 2008.

[59] P.A. Thompson and M.O. Robbins. Origin of stick-slip motion in boundary lubrication. *Science*, 250:792–794, 1990.

[60] P.A. Thompson and M.O. Robbins. Shear flow near solids: epitaxial order and flow boundary conditions. *Phys. Rev. A*, 41:6830–6837, 1990.

[61] Xuan Zheng. *Molecular dynamics simulation of boundary lubricant contacts*. PhD thesis, Ph.D. Thesis, University of Wollongong, 2014.

[62] G. Spijker, P.and Anciaux and Molinari J.F. The effect of loading on surface roughness at the atomistic level. *Comput. Mech.*, 50:273–283, 2012.

[63] M.S. Daw and M.I. Baskes. Embedded-atom method: derivation and application to impurities, surfaces, and other defects in metals. *Phys. Rev. B*, 29: 6443–6453, 1984.

[64] D.P. Wei, H.A. Spikes, and S. Korcek. The lubricity of gasoline. *Tribol. T.*, 42: 813–823, 1999.

[65] Y. Zhu and S. Granick. Rate-dependent slip of newtonian liquid at smooth surfaces. *Phys. Rev. Lett.*, 87:096105, 2001.

[66] C. Neto, D.R. Evans, E. Bonaccurso, H.J. Butt, and V.S.J. Craig. Boundary slip in newtonian liquids a review of experimental studies. *Rep. Prog. Phys.*, 68:2859–2897, 2005.

[67] A. Koike and M. Yoneya. Chain length effects on frictional behavior of confined ultrathin films of linear alkanes under shear. *J. Phys. Chem. B*, 102:3669–3675, 1998.

[68] I.M Sivebaek, V.N. Samoilov, and B.N.J. Persson. Velocity dependence of friction of confined hydrocarbons. *Langmuir*, 26:8721–8728, 2010.

[69] A. Jabbarzadeh, J.D. Atkinson, and R.I. Tanner. The effect of branching on slip and rheological properties of lubricants in molecular dynamics simulation of couette shear flow. *Tribol. Int.*, 35:35–46, 2002.

[70] A. Jabbarzadeh, J.D. Atkinson, and R.I. Tanner. Effect of molecular shape on rheological properties in molecular dynamics simulation of star, h, comb, and linear polymer melts. *Macromolecules*, 36:5020–5031, 2003.

[71] H. Ghaednia and R.L. Jackson. The effect of nanoparticles on the real area of contact,friction, and wear. *J Tribology*, 135:041603, 2013.

[72] M. A. Ghaffari, E. Pahl, and S. Xiao. Three dimensional fatigue crack initiation and propagation analysis of a gear tooth under various load conditions and fatigue life extension with boron/epoxy patches. *Engineering Fracture Mechanics*, 135:126–146, 2015.

[73] S. Podrug, D. Jelaska, and S. Glodez. Influence of different load models on gear crack path shapes and fatigue lives. *Fatigue Fract. Eng.* , 31:327–339, 2008.

[74] M. Hoffmann and T. Seeger. A generalized method for estimating multiaxial elastic-plastic notch stresses and strains, parts 1 and 2. *Trans. ASME*, 107: 250–260, 1985.

[75] Halfpenny A. and Bishop NWM. Vibration fatigue. *nCode International Ltd. 230 Woodbourn Road, Sheffield, S9 3LQ. UK*, 1997.

[76] M. Sraml and Flasker J. Computational approach to contact fatigue damage initiation analysis of gear teeth flanks. *Int. J. Adv. Manuf. Technol.*, 31:1066–1075, 2007.

[77] S. Glodez, H. Winter, and H.P. Stuwe. A fracture mechanics model for the wear of gear flanks by pitting. *Wear*, 208:177–183, 1997.

[78] S. Glodez and Z. Ren. Modeling of crack growth under cyclic contact loading. *Theo. and Appl. Fract. Mech.*, 30:159–173, 1998.

[79] S. Glodez, Z. Ren, and J. Flasker. Simulation of surface pitting due to contact loading. *Int. J. Num. Meth. Engng.*, 43:33–50, 1998.

[80] D.G. Lewicki and R. Ballarini. Effect of rim thickness on gear crack propagation path. *J. Mech. Des.*, 119(1):88–95, 1997.

[81] D.G. Lewicki and R. Ballarini. Rim thickness effects on gear crack propagation life. *Int J Fract*, 87(1):59–86, 1997.

[82] C. Albrecht. Transmission design using finite element method analysis techniques. *J. Am. Helicopter Soc.*, 33(2):3–14, 1988.

[83] A. Blarasin, M. Guagliano, and L. Vergani. Fatigue crack growth predictions in specimens similar to spur gear teeth. *Fatigue Fract Engng Mater Struct.* , 20(8):1171–1182, 1997.

[84] J. Flasker and S. Pehan. Crack propagation in tooth root with variable loading. *Commun Num Meth Engng.*, 9(2):103–110, 1993.

[85] S Pehan, T Hellen, J Flasker, and S. Glodez. Numerical methods for determining stress intensity factors vs. crack depth in gear tooth roots. *Int. J. Fatigue*, 19(10):677–685, 1997.

[86] L.E. Spievak, P.A. Wawrzynek, A.R. Ingraffea, and D.G. Lewicki. Simulating fatigue crack growth in spiral bevel gears. *Engng Fract Mech.*, 68:53–76, 2001.

[87] G. Fajdiga and M. Sraml. Fatigue crack initiation and propagation under cyclic contact loading. *Engng Fract Mech.*, 76:1320–1335, 2009.

[88] S. Glodez, S. Pehan, and J. Flas. Experimental results of the fatigue crack growth in a gear tooth root. *Int. J. Fatigue*, 20:669–675, 1998.

[89] D.G. Lewicki, A.D. Sane, R.J. Drago, and P.A. Wawrzynek. Three-dimensional gear crack propagation studies. *NASA/TM-1998-208827/ARL-TR-1833*, 1998.

[90] H.A. Richard, F.G. Buchholz, G. Kulmer, and M. Schollmann. 2d and 3d mixed mode criteria. *Adv. Frac. Damage Mech.*, 251:251–260, 2003.

[91] R. Krueger. The virtual crack closure technique, history, approach and applications. *NASA/CR-2002-211628, ICASE Report No. 2002-10*, 2002.

[92] T. Burton, N. Jenkins, D. Sharpe, and E. Bossanyi. *Wind Energy Handbook*. Wiley; 2 edition, 2011.

[93] E.S. Aggelopoulos, T.D. Righiniotis, and M.K. Chryssanthopoulos. Debonding of adhesively bonded composite patch repairs of cracked steel members. *Composite B*, 42:1262–1271, 2011.

[94] T.L. Anderson. *Fracture mechanics: Fundamentals and applications*. CRC, 2005.

[95] G.R. Irwin. *Fracture Dynamics*. Fracturing of Metals, American Society for Metals, Cleveland, 1948.

[96] G.R. Irwin. Linear fracture mechanics, fracture transition, and fracture control. *Engng. Frac. Mech.*, 1:241–257, 1968.

[97] G.R. Irwin and D.E. Wit. A summary of fracture mechanics concepts. *Journal of Testing and Evaluation*, 11:56–65, 1983.

[98] D.S. Dugdale. Yielding of steel sheets containing slits. *Journal of the Mechanics and Physics of Solids*, 8:100–104, 1960.

[99] G.I. Barenblatt. The mathematical theory of equilibrium cracks in brittle fracture. *Advances in applied mechanics*, 7:55–129, 1962.

[100] G. Ruiz, A. Pandolfi, and M. Ortiz. Three-dimensional cohesive modeling of dynamic mixed-mode fracture. *International Journal for Numerical Methods in Engineering*, 52:97–120, 2001.

[101] J. W. Foulk, D. H. Allen, and K. L. E. Helms. Formulation of a three-dimensional cohesive zone model for application to a finite element algorithm. *Computer Methods in Applied Mechanics and Engineering*, 183:51–66, 2000.

[102] M. Elices, G. V. Guinea, J. Gomez, and J. Planas. The cohesive zone model: advantages, limitations and challenges. *Engineering fracture mechanics*, 69: 137–163, 2002.

[103] J. Planas, M. Elices, G. V. Guinea, F. J. Gomez, D. A. Cendon, and I. Arbilla. Generalizations and specializations of cohesive crack models. *Engineering fracture mechanics*, 70:1759–1776, 2003.

[104] J. M. Melenk and I. Babuska. The partition of unity finite element method: basic theory and applications. *Computer methods in applied mechanics and engineering*, 139:289–314, 1996.

[105] T. Belytschko and T. Black. Elastic crack growth in finite elements with minimal remeshing. *International Journal for Numerical Methods in Engineering*, 45: 601–620, 1999.

[106] N. Moes, J. Dolbow, and T. Belytschko. A finite element method for crack growth without remeshing. *International Journal for Numerical Methods in Engineering*, 46:131–150, 1999.

[107] N. Sukumar, N. Moes, B. Moran, and T. Belytschko. Extended finite element method for three-dimensional crack modelling. *International Journal for Numerical Methods in Engineering*, 48:1549–1570, 2000.

[108] J. V. Cox. An extended finite element method with analytical enrichment for cohesive crack modeling. *International Journal for Numerical Methods in Engineering*, 78:48–83, 2009.

[109] N. Sukumar and J. H. Prevost. Modeling quasi-static crack growth with the extended finite element method part i: Computer implementation. *International Journal for Numerical Methods in Engineering*, 40:7513–7537, 2003.

[110] S. Mariani and U. Perego. Extended finite element method for quasi-brittle fracture. *International Journal for Numerical Methods in Engineering*, 58:103–126, 2003.

[111] G. Meschke and P. Dumstorff. Energy-based modeling of cohesive and cohesionless cracks via x-fem. *Computer methods in applied mechanics and engineering*, 196:2338–2357, 2007.

[112] S. Li and W. K. Liu. *Meshfree and particle methods and their applications*. Applied Mechanics Reviews, 2002, 55:1.

[113] W. K. Liu, Y. Chen, S. Jun, J. S. Chen, T. Belytschko, C. Pan, R. A. Uras, and C. T. Chang. Overview and applications of the reproducing kernel particle methods. *Archives of Computational Methods in Engineering*, 3:3–80, 1996.

[114] G. R. Liu and M. B. Liu. *Smoothed particle hydrodynamics: a meshfree particle method*. World Scientific Pub Co Inc, 2003.

[115] T. Rabczuk, P. Areias, and T. Belytschko. A meshfree thin shell method for non-linear dynamic fracture. *International Journal for Numerical Methods in Engineering*, 72:525–548, 2007.

[116] T. Rabczuk, JH. Song, and T. Belytschko. Simulations of instability in dynamic fracture by cracking particles methods. *Engineering Fracture Mechanics*, 76: 730–741, 2009.

[117] S.A. Silling. Reformulation of elasticity theory for discontinuities and long-range forces. *Journal of the Mechanics and Physics of Solids*, 48:175–209, 2000.

[118] S.A. Silling. Linearized theory of peridynamic states. *Journal of Elasticity*, 99: 85–111, 2010.

[119] S. A. Silling and E. Askari. A meshfree method based on the peridynamic model of solid mechanics. *Computers & Structures*, 83:1526–1535, 2005.

[120] B. Kilic and E. Madenci. Prediction of crack paths in a quenched glass plate by using peridynamic theory. *International Journal of Fracture*, 156:165–177, 2009.

[121] B. Kilic and E. Madenci. Structural stability and failure analysis using peridynamic theory. *International Journal of Non-Linear Mechanics*, 44:845–854, 2009.

[122] Y. D. Ha and F. Bobaru. Studies of dynamic crack propagation and crack branching with peridynamics. *International Journal of Fracture*, 162:229–244, 2010.

[123] Y. D. Ha and F. Bobaru. Characteristics of dynamic brittle fracture captured with peridynamics. *Engineering Fracture Mechanics*, 78:1156–1168, 2011.

[124] S. A. Silling, O. Weckner, and E. Askari. Crack nucleation in a peridynamic solid. *International Journal of Fracture*, 162:219–227, 2010.

[125] M. L. Parks, R. B. Lehoucq, S. J. Plimpton, and S. A Silling. Implementing peridynamics within a molecular dynamics code. *Computer Physics Communications*, 179:777–783, 2008.

[126] J. Xu, A. Askari, O. Weckner, and S. A. Silling. Peridynamic analysis of impact damage in composite laminates. *Journal of Aerospace Engineering*, 21:187–194, 2008.

[127] B. Kilic, A. Agwai, and E. Madenci. Peridynamic theory for progressive damage prediction in center-cracked composite laminates. *Composite Structures*, 90: 141–151, 2009.

[128] W. Hu, Y. D. Ha, , and F. Bobaru. Modeling dynamic fracture and damage in a fiberreinforced composite lamina with peridynamics. *International Journal for Multiscale Computational Engineering*, 9:707–726, 2011.

[129] W. Hu, Y. D. Ha, , and F. Bobaru. Peridynamic model for dynamic fracture in unidirectional fiber-reinforced composites. *Computer Methods in Applied Mechanics and Engineering*, 217:247–261, 2012.

[130] S. A. Silling, M. Epton, O. Weckner, J. Xu, and E. Askari. Peridynamic states and constitutive modeling. journal of elasticity. *Journal of Elasticity*, 88:151–184, 2007.

[131] S. A. Silling and R. B. Lehoucq. Convergence of peridynamics to classical elasticity theory. *Journal of Elasticity*, 93:13–37, 2008.

[132] T. L. Warren, S. A. Silling, A. Askari, O. Weckner, M. A. Epton, and J. Xu. nonordinary state-based peridynamic method to model solid material deformation and fracture. *International Journal of Solids and Structures*, 46:1186–1195, 2009.

[133] J. T. Foster, S. A. Silling, and W. W. Chen. Viscoplasticity using peridynamics. *International Journal for Numerical Methods in Engineering*, 81:1242–1258, 2009.

[134] J. T. Foster, S. A. Silling, and W. W. Chen. An energy based failure criterion for use with peridynamic states. *International Journal for Multiscale Computational Engineering*, 9:675–688, 2011.

[135] S. A. Silling and R. B. Lehoucq. Peridynamic theory of solid mechanics. *Advances in Applied Mechanics*, 44:73–168, 2010.

[136] G. T. Mase, R. E. Smelser, and G. E. Mase. *Continuum mechanics for engineers*. CRC, 1999.

[137] M. L. Parks, S. J. Plimpton, R. B. Lehoucq, and S. A. Silling. *Peridynamics with LAMMPS: A user guide. Technical report.* A user guide. Technical report, Technical Report SAND 2008-1035, Sandia National Laboratories, 2008.

[138] M. Zimmermann. *A continuum theory with long-range forces for solids*. PhD thesis, Massachusetts Institute of Technology, 2005.

[139] R. W. Macek and S. A. Silling. Peridynamics via finite element analysis. *Finite elements in analysis and design*, 43:1169–1178, 2007.

[140] F. Bobaru, M. M. Yang, L. F. Alves, E. Silling, S. A.and Askari, and J. Xu. Convergence, adaptive refinement, and scaling in 1d peridynamics. *International Journal for Numerical Methods in Engineering*, 77:852–877, 2009.

[141] E. Emmrich and O. Weckner. On the well-posedness of the linear peridynamic model and its convergence towards the navier equation of linear elasticity. *Communications in Mathematical Sciences*, 5:851–864, 2007.

[142] L. Lapidus and G.F. Pinder. *Numerical solution of partial differential equations in science and engineering.* Wiley, New York, 1982.

[143] E. Oterkus, I. Guven, and E. Madenci. Fatigue failure model with peridynamic theory. pages 1–6, Las Vegas, NV, June 2010. IEEE Intersociety Conference on Thermal and Thermomechanical Phenomena in Electronic Systems (ITherm).

[144] H Hertz. On the Contact of Elastic Solids. *Journal of reine angew. math*, 92: 156–171, 1882.

[145] Y. Liu, B. Stratman, and S. Mahadevan. Fatigue Crack Initiation Life Prediction of Railroad Wheels. *Int. J. Fatigue*, 28:747–756, 2006.

[146] Y. Liu and S. Mahadevan. Unified Multiaxial Fatigue Damage Model for Isotropic and Anisotropic Materials. *Int. J. Fatigue*, 29:347–359, 2007.

[147] A.C.T. Van Duin, S. Dasgupta, F. Lorant, and W.A. Goddard. Reaxff: a reactive force field for hydrocarbons. *J. Phys. Chem. A*, 105:9396–9409, 2001.

[148] M. Aryanpour, A.C.T Van Duin, and J.D. Kubicki. Development of a reactive force field for iron-oxyhydroxide systems. *J. Phys. Chem. A*, 114:6298–6307, 2010.